A STUDY OF THERMAL INSTABILITIES IN ELECTROSLAG MELTING

BY

ROBERT O. JACKSON

A THESIS SUBMITTED IN PARTIAL FULFILMENT OF

THE REQUIREMENTS FOR THE DEGREE OF

MASTER OF APPLIED SCIENCE

in the Department

of

METALLURGY

We accept this thesis as conforming to the

required standard

THE UNIVERSITY OF BRITISH COLUMBIA

January, 1972

In presenting this thesis in partial fulfilment of the requirements for an advanced degree at the University of British Columbia, I agree that the Library shall make it freely available for reference and study. I further agree that permission for extensive copying of this thesis for scholarly purposes may be granted by the Head of my Department or by his representatives. It is understood that copying or publication of this thesis for financial gain shall not be allowed without my written permission.

Department of Metallurgy

The University of British Columbia
Vancouver 8, Canada

Date April 28, 1972

ABSTRACT

Structural and compositional changes resulting from interruptions in the steady-state heat balance of an electroslag remelted ingot have been investigated on a laboratory scale electroslag furnace. An attempt was also made to solve some of the fundamental problems introduced by the proposed production of large commercial ingots in a tandem electrode change furnace.

The investigation was carried out on three commercially available alloy steels: 1) EN-25, 2) AISI 4340, and 3) AISI 630 (17-4 P.H.).

Power interruption experiments on EN-25 and AISI 4340 steels revealed only minor structural changes but did show carbon concentration banding. Carbon rich bands were also produced by periodic variations in the slag skin thickness.

Power interruption experiments on AISI 630 produced some structural changes but no change in the concentrations of the major alloying elements was detected.

The mixing action in the liquid metal pool appears to be due to a slow convective motion which causes the liquid to approach a state of complete mixing at the solidification rates found in the ESR process.

A general heat balance was calculated for a 10 cm dia. ESR ingot. The various volume fractions solidified were calculated for different durations of the "power-off" mode. The results of the heat balance were extended to a large (61 cm dia.) commercial ingot and the volume solidified during a 60 second power interruption was estimated.

A heat transfer program was written to determine the unsteady state temperature profiles in an electrode as a function of temperature

of the slag bath and time after immersion. The resulting profiles indicated that in order to avoid any major structural and/or compositional changes during an electrode change operation, electrode preheating is mandatory.

TABLE OF CONTENTS

LIST OF FIGURES

LIST OF TABLES

LIST OF SYMBOLS

Symbol	
A	cross-sectional area, cm^2
B	magnetic induction, gauss
C_i	concentration at the S/L interface, wt. %
C_o	initial concentration, wt. %
C'_x	concentration x cm from the S/L interface, wt. %
C_x	relative fractional concentration x cm from the S/L interface
C_S	concentration of the solid, wt. %
C_L	concentration of the liquid, wt. %
C_p	specific heat, cal g^{-1} $°C^{-1}$
F	Lorentz Force, nt.
H_L	height of liquid metal, cm
h	heat transfer coefficient, cal $cm^{-2}sec^{-1}°C^{-1}$
h_I	heat transfer coefficient at the slag/metal interface, cal $cm^{-2}sec^{-1}°C^{-1}$
i	current, amps
K	thermal conductivity, cal $cm^{-1}sec^{-1}°C^{-1}$
K_A	area correction factor
K_E	effective distribution coefficient
k_o	equilibrium distribution coefficient
L	latent heat, cal g^{-1}
m	mass, g
Q_A	available heat content, kcals
Q_I	heat input into the electrode, kcals
Q_L	total heat loss, kcals
Q_T	total heat content, kcals
$\dot{q}$	rate of heat loss, kcals sec^{-1}

Symbol

q	heat loss at each interface, kcal
r'	number of units from the centerline
Δr	unit length in the r' direction
S	shape correction factor
T_b	slag bath temperature, °C
T_o	initial temperature, °C
ΔT_S	degrees of superheat, °C
V	volume, cm^3
ΔZ	unit length in the z' direction
ρ	density, g cm^{-3}
ε	emmisivity
α	$\frac{K}{\rho C_p}$, thermal diffusivity, $cm^2 sec^{-1}$
σ	Stefan-Boltzmann constant, 5.67×10^{-8} watts, $m^{-2} {}^\circ K^{-4}$

ACKNOWLEDGEMENT

The author is indebted to Dr. A Mitchell for his advice and assistance throughout the duration of this work.

Thanks are also due to Dr. F. Weinberg and fellow graduate students for innumerable helpful discussions.

The assistance of the technical staff during the experimental program is greatly appreciated.

The financial assistance of the Consarc Corporation is gratefully acknowledged.

1. INTRODUCTION

With the increasing demands of modern machine builders for large forgings that can withstand severe service conditions, steel ingots of considerable size and weight will be required.

Thus, for example, in the near future the capacity of turbogenerators in nuclear electric power stations will be close to 1300 mega watts. The rotor shafts for such turbogenerators will have billet weights of around 300 tons, with diameters greater than 3000 mm (118 in.). To produce such rotor shafts, static cast steel ingots for forgings weighing more than 600 tons and having diameters about 5000 mm (197 in.) would be required.

The problems associated with producing steel ingots exceeding even 200 tons by conventional techniques are well known. During the crystallization of such large volumes of liquid metal, macrosegregation and shrinkage processes become significant. The result is certain defects in the steel ingots which are irreparable even with further treatment and are inherently transferred to the forgings and to parts made from them.

The existing methods for improving heavy steel ingots, such as sequentially pouring the liquid metal into the mould, vacuum treatment, heating and hot topping the head of the ingots are not efficient enough and do not guarantee a good macrostructure, homogeneity, uniformity, and isotropy of mechanical properties throughout the billet and forgings.

To meet the demands of the modern machine builders, therefore, it is not unreasonable that considerable attention is being focussed on scaling up the electroslag remelting process (ESR) to produce high quality, large tonnage ingots.

1.1 Problems Introduced by "Scale-up"

As furnace sizes increase to meet the new demands imposed by industry, so too will the problems associated with their construction and operation. The first problem facing the process metallurgist is how to design an ESR machine that can economically produce large ingots (100 to 200 tons). At present the majority of the commercial ESR ingots being produced fall into the 5 to 20 ton range with a maximum size of approximately 50 tons. As the ingot weights increase, however, the single electrode design which is currently enjoying the greatest success becomes increasingly inadequate and expensive. The main problem of scaling up a machine of this design is that in order to produce a 200 ton ingot a 200 ton electrode is required. The difficulty of producing such large electrodes and the sophisticated equipment necessary to suspend them and control their vertical motion precisely makes it a practical exercise to investigate possible alternatives.

The most obvious alternative is a machine that uses several small electrodes to produce one large ingot. At present there are two main types of multiple electrode machines in operation. These are the three phase, multi-electrode design (Figure 1), and the tandem electrode design (Figure 2). The three phase, seven electrode bifilar

furnace has a projected capacity of 100 to 200 tons. There is no information available, however, regarding its current status. Another multiple electrode machine is the three phase, three electrode design. At present, however, this design has not been used as an electrode change machine and is limited to producing ingots in the 10 to 20 ton range. The principle behind this design is that the electrodes are of different lengths so that whenever one requires changing there will still be two electrodes operating. The advantage of this technique is that it provides the operator with a considerable degree of control over the system during the electrode change operation. The main drawbacks of this design, unfortunately, are its complexity and the cost associated with producing a large machine of this type.

The tandem electrode arrangement, on the other hand, is mechanically very simple and could be modified to produce larger ingots. This design is also much more flexible with regard to its power requirements. Its main problem is that during the electrode change operation the power to the system must be shut off which could drastically alter the general heat balance of the process.

In order to obtain a better understanding of the effectiveness of the tandem electrode design it is necessary to ask the following questions:

1. To what extent is the overall heat balance of the system effected by the electrode change operation?

2. To what extent do the resulting changes in the heat balance affect the structural and compositional uniformity of the ingot?

The answers to these questions are of the utmost importance when considering the feasibility of using the tandem electrode design. Because of the considerable investment of time and money required to produce large ESR ingots it is essential that they contain no structural or compositional irregularities that could effect the mechanical properties of the steel.

1.2 Objectives of the Present Work

Although a great deal of literature is available pertaining to normal ESR production, little or no work has been published which concerns itself with disruptions in the heat balance, and how they effect the structure and composition of the steel being produced. It is the object of this study to analyze the effects of a power loss to the system and also other problems related to electrode change machines.

The present investigation was primarily concerned with five major topics:

1. The structural changes that result from a disruption in the power supply to the system.

2. The degree of the segregation during the power loss and the extent of any compositional banding.

3. The volume of liquid metal that solidified during the power loss.

4. The general heat balance for the system and how it changed as a result of any disruptions in the power supply.

5. Changing electrodes and its effect on the overall heat balance.

In addition to the major areas of investigation, work was also done relating variation in the slag skin thickness produced by control oscillations, to compositional banding. Also, whenever possible, the investigation was extended to include ingots produced by vacuum arc refining (VAR) for the purpose of comparison.

Although the experiments were carried out on a lab scale ESR unit and many assumptions had to be made about the system due to its complex nature it is believed that the results can be extrapolated to provide meaningful information about the questions related to the large scale electrode change machines.

1.3 Previous Work

The fundamental principles underlying the solidification of steel castings have been well documented in the many books and papers written on the subject.[1,2] More specific studies[3-8] on micro- and macrosegregation in steel castings, however, have mainly pertained to static ingots, or idealized systems in which the solidification variables have been partially controlled. Although these papers provide a great deal of information concerning solidification and segregation in specific systems, it cannot be applied directly to the ESR process because of the large differences in the solidification mode. In the ESR process the solidification is directional within a water cooled-mould and is maintained at a slow solidification rate (0.005 to 0.03 cm sec^{-1}) against a large temperature gradient (10 to 100°C cm^{-1}) by the system's power input. The method also differs from other casting processes in that fresh metal of a constant composition is

added to the liquid pool at a constant slow (3 to 120 g sec^{-1}) rate.

Solidification studies on continuous casting,[9] which is also a cold-crucible process, contribute little information about the ESR process because of the large differences in the casting speeds, and heat transfer between the two systems.

The ESR process has often been classified as a large zone refiner, which is generally an invalid comparison. The confusion between the two processes probably arose due to their physical similarities. It should be noted, however, that the zone refining process is usually a multi-pass operation, and that the relationship governing the solute redistribution during the initial pass is simply the equation for complete mixing in a directionally solidified casting assuming constant metal addition.[1] Since the extent of the mixing action in the metal pool and the effect of the dendritic interface on the distribution coefficients are unknown this equation, therefore, cannot be meaningfully applied to the ESR system.

As far as any detailed examinations of the solidification process in ESR ingots is concerned there has been very little work done. Fredricksson and Jarleborg[10] analyzed the effects of power interruptions on the structure of an 18/8 stainless steel produced by the ESR process. Using sulphur prints and a quenching technique they determined the liquid metal pool depth and microstructure of the ingots examined. On the basis of these experiments they speculated that a strong convective mixing action exists in the metal pool. They also investigated the effects of power interruptions, "dipping" of the electrode, and electrode changes on the ingots structure. They found that the disruptions in the system resulted in a banded structure in the transverse

direction. It was also noted that for power interruptions shorter than 30 seconds there was no apparent sulphur segregation and for times longer than 60 seconds there was significant detectable sulphur segregation. In an experiment using a preheated electrode, there was no improvement in the sulphur segregation problem. The possible zone refining effect of the ESR process was also investigated by monitoring Cr and Ni concentrations longitudinally in an 18/8 ingot. They found a lower concentration of both Cr and Ni in the final transient which they attributed to inverse segregation. An analysis of the transverse segregation of Cr and Ni was also made, and this type of segregation was found at high melt rates (13.3 g sec^{-1}). This was related to the much deeper metal pool found at these speeds.

Another investigation of the solidification in ESR ingots was conducted by Takada et al.[11] The work was performed on a 5 ton (750 mm dia.) ingot and it was examined using dye penetration, sulphur prints as well as microstructure and segregation tests. The analysis related the temperature gradient/growth velocity ratio (G/V) to the observed microstructure which became progressively coarser towards the ingot center. They also performed a chemical analysis on the ingot and found no significant macrosegregation.

DeVries and Mumau[12] examined the dendritic formation and solidification in highly alloyed materials produced by the ESR process. They found that the microsegregation increased towards the center of the consumably melted ingots and that chromium showed inverse micro-segregation. They also demonstrated that the secondary dendrite arm spacing increased with an increase in either the melt rate or the ingots cross-sectional area.

Firganek et al.[13] used radioactive isotopes to investigate the solidification front and depth of the liquid metal pool in an ESR furnace. Using W^{185} they successfully outlined the pool profile and ingot structure, and showed how this technique could be used to determine the optimum operating conditions.

Although these papers provide some general background information concerning the solidification in the ESR process, they all, with the exception of the Fredriksson et al. paper, deal with the steady state condition. Despite the fact that the Fredriksson et al. paper deals with the effects of power interruptions on the system, it does not consider the problem in enough detail to answer the fundamental questions asked in this presentation.

2. EXPERIMENTAL

2.1 Introduction

The ESR ingots used in this study were produced on the ESR unit at the University of British Columbia. The VAR ingots used were produced outside the university at the Armco Steel Corporation in Baltimore,Maryland, and the U.S. Bureau of Mines in Albany, Oregon.

The ESR process is shown schematically in Figure 3 and has been described in detail by Etienne.[14] On the University unit it was possible to produce various sized ingots and to change and control many of the operating parameters.

All the VAR ingots examined in this study were manufactured externally, and the companies involved provided a complete production history for each ingot. A schematic diagram of a VAR furnace is shown in Figure 4.

2.2 Materials

2.2.1 Electrode Composition

For this investigation three commercial alloys were used. The criteria for selecting these particular steels were: 1) availability 2) cost and 3) the presence of alloying elements that would show significant segregation. Table I gives the composition of the alloys studied.

Table I. Composition of alloys studied

(1) Vibrac EN-25 (supplied by the British Steel Corporation)

Fe	C	Mn	Si	S	P	Ni	Cr	Mo
Bal	0.28	0.67	0.22	0.058	0.012	2.5	0.72	0.6

Sn	Cu	Al
0.028	0.27	0.01

(2) AISI 4340 (supplied by British Steel Corporation)

Fe	C	Mn	Si	S	P	Ni	Cr	Mo
Bal	0.39	0.72	0.24	0.018	0.012	1.75	0.84	.24

(3) AISI 630 (17-4PH) (supplied by the Armco Steel Company)

Fe	C	Mn	Si	P	S	Cr	Ni	Co+Ta
Bal	0.07	1.0	1.0	0.025	0.025	16.5	4.0	0.3

Cu	Mo
4.0	0.5

2.2.2 Slag Composition

The major slag constituent was prefused calcium fluoride. It was combined with different percentages of recrystallized alumina grain (Norton Abrazive 99.9% purity).

The starting compact (used in all cases) consisted of a mixture of parent metal turnings and 60 g CaF_2 powder in the ratio of 15 g to

25 g per cm of compact.

2.3 Ingot Production

2.3.1 ESR Ingots

Table II summarizes the operating conditions for the ESR ingots used in this study. The production data for several low quality ingots analyzed was not available from the producers involved.

The technique used for the stop-start experiments involved shutting off the main power supply to the system. During this period the current recorder continued to operate. A section from the current chart during a "power-off" sequence is shown in Figure 5. Using the operating chart it was possible to get an accurate estimate of the interruption time.

2.3.2 VAR Ingots

Table III summarizes the operating conditions for the VAR ingots examined.

2.4 Specimen Preparation

All specimens to be examined under the optical microscope or the electron microprobe were polished down to 1 micron on a diamond lap. Larger specimens and specimens where only the macrostructure was of importance were polished on No. 0 or No. 00 emergy paper.

Table II.

ingot no.	mould dia. (cm)	electrode dia. (cm)	electrode comp.	electrode polarity	atmos-phere	slag comp.	voltage (volts)	current (amp)	melt rate (g sec^{-1})	ingot length
1	7.6	3.81	EN 25	-ve	air	CaF_2-27 wt.% Al_2O_3	23	1180	3.4	23
2	7.6	3.81	EN 25	-ve	air	CaF_2-27 wt.% Al_2O_3	23	1170	3.7	22
3	7.6	3.81	EN 25	-ve	air	CaF_2-27 wt.% Al_2O_3	23	1160	2.8	23.5
4	7.6	3.81	AISI 4340	-ve	air	CaF_2-25 wt.% Al_2O_3	23	1175	3.1	26
5	7.6	3.81	AISI 4340	-ve	air	CaF_2-25 wt.% Al_2O_3	23	1150	3.3	25
6	7.6	3.81	AISI 4340	-ve	air	CaF_2-27 wt.% Al_2O_3	23.5	1125	2.6	25.5
7	7.6	3.81	EN 25	-ve	argon	CaF_2-27 wt.% Al_2O_3	23.5	1200	3.1	23
8	7.6	3.81	EN 25	A.C.	argon	CaF_2-27 wt.% Al_2O_3	25	850	3.4	20
9	7.6	3.81	EN 25	A.C.	argon	CaF_2-27 wt.% Al_2O_3	25	825	3.6	11
10	7.6	3.81	EN 25	A.C.	argon	CaF_2-27 wt.% Al_2O_3	25	925	3.1	24

Table II. (Continued)

11	7.6	3.81	EN 25	-ve	argon	CaF_2-27 wt.% Al_2O_3	23	1275	2.7	23
12	10	6.3	EN 25	-ve	air	CaF_2-25 wt.% Al_2O_3	23.5	1550	6.4	48
13	10	6.3	EN 25	-ve	air	CaF_2-25 wt.% Al_2O_3	23.5	1550	6.1	51
14	7.6	3.81	AISI 630	-ve	argon	CaF_2-10 wt.% Al_2O_3	22.5	1090	3.4	18
15	7.6	3.81	AISI 630	A.C.	argon	CaF_2-10 wt.% Al_2O_3	24.5	800	3.0	21
16	7.6	3.81	AISI 630	A.C.	argon	CaF_2-10 wt.% Al_2O_3	23.5	800	3.09	23
17	7.6	3.81	AISI 630	A.C.	argon	CaF_2-10 wt.% Al_2O_3	23.5	800	3.2	20
18	7.6	3.81	AISI 630	-ve	argon	CaF_2-10 wt.% Al_2O_3	23.5	1400	2.8	22

Table III.

ingot no.	ingot dia.(cm)	ingot height(cm)	material	voltage (volts)	current (amps)	melt rate (g/sec)	Producer
V-1	16.5	17	AISI 630	23	4000	16.2	Armco
V-2	16.5	11	AISI 630	23	4000	14.6	Armco
V-3	10.0	25	AISI 4340	26	2900	--	Bureau of Mines
V-4	7.6	25	AISI 630	23	2000	9.1	Armco

2.5 Techniques Used to Analyze the Effects of Power Interruptions on the Structure and Composition of the Ingot

2.5.1 Etching

2.5.1.1 EN-25 and AISI 4340 Steels

Oberhoffer's etch in conjunction with 3 percent nital were used to detect changes in structure and composition resulting from power disruptions. Oberhoffer's etch consists of 1 g cupric chloride, 0.5 g stannous chloride, 50 g ferric chloride, 30 ml hydrochloric acid, 500 ml water, and 500 ml ethyl alcohol.[15] This etchant was particularly useful for examining the dendritic structure of the two low alloy steels. The 3 percent nital on the other hand was much more useful for detecting changes in the carbon concentration in the steel as a result of fluctuations in the power.

2.5.1.2 AISI 630 (17-4PH)

As there were several etchants available for AISI 630, they were chosen depending on the desired quality of the etch and the size of the specimen. For large specimens where only a macroetch was needed, the best technique was to immerse the specimen in a 50 percent hydrochloric acid solution for up to 36 hours. For smaller specimens a much faster macroetch consisted of 100 ml ethyl alcohol, 100 ml hydrochloric acid, and 50 ml of nitric acid. The best microetch was found to be Vilella's etch. This is a mixture of 5 ml hydrochloric acid, 1 g picric acid and 100 ml ethyl alcohol. This etchant was particularly useful for determining the presence of the δ-ferrite phase. Another etchant useful for identifying this phase

was Kalling's reagent. This was comprised of 100 ml hydrochloric acid, 100 ml ethyl alcohol and 5 g cupric chloride.

2.5.2 Sulphur Prints

A convenient way to observe the effect of a disruption in the steady state condition on the structure and composition of a steel, is to make a sulphur print of the affected region. Because of the very low sulphur contents of the three aloys studied, however, it was necessary to externally add sulphur to the system. This was done by adding approximately 4 g of iron sulphide between the electrode and the mould wall as shown in Figure 6. After each addition the system was given several minutes to return to equilibrium before any experiments were carried out.

The solidified ingot was cut axially in half and surface-ground. Photographic bromide paper was soaked in a 2 percent sulphuric acid solution for 3 to 4 minutes, then allowed to hang until the excess solution had drained away. The emulsion side of the paper was placed in direct contact with the ground ingot surface for up to 5 minutes. The exposed sulphur print was then fixed and dried. After each print the surface of the specimen was reground to expose unreacted FeS inclusions.[16]

2.5.3 Autoradiography

Another technique used to detect compositional and structural changes produced by deviations from the steady state condition is autoradiography. An experiment was devised whereby radioactive tin could be added to the melt under a closed atmosphere. Tin was selected

because of its very low vapour pressure and its density, which is close to that of iron. The isotope chosen was Sn^{113} which is an X-ray and soft gamma emitter and has a half-life of 112 days.[17]

The radioactive isotope was introduced into the system by embedding it in the electrode and melting it into the system. Figure 7 shows how the tin was situated in the electrode. The purpose of the aluminum was to ensure that there was no oxidation of the tin while it was melting and alloying.

As it was important to know the exact moment the tin entered the system, a series of preliminary experiments were performed to determine the minimum quantity of tin plus aluminum required to produce a perturbation in the operating chart. It was found that approximately 2 g produced a noticeable change in the operating current. The effect on the current when they enter the system is shown in Figure 9. The drop in the operating current occurs because the tin and the aluminum enter the system as one or two large drops thereby increasing the electrode-ingot gap.

Once produced, the radioactive ingots were cut axially in half and surface ground. They were then autoradiographed using exposure times ranging from 24 to 72 hours.

2.5.4 Microprobe Analysis

The best technique for determining compositional variations in elements such as nickel, chromium, and copper is to use the electron probe. The microanalysis was performed on a JEOL-JXA-3A microprobe using a voltage of 25 KeV and a beam current of 0.08 μa. A quartz

crystal was used in the spectrometer and K_α radiation was measured for all specimens.

Due to the low X-ray take-off angle ($\theta = 20°$), etched specimens could not be effectively examined. It was necessary, therefore, to lightly etch the specimens and mark the areas of interest with indentation on a microhardness tester. Microphotographs were then taken of the specimens before they were highly repolished on the 1 micron diamond lap.

Measurements with the microprobe were made by point counting for periods of 10 sec, at 20 micron intervals. The results were then printed out both numerically and graphically. All results were corrected using the MAGIC[18] program. Specific areas which showed concentration anomalies were quantitatively analyzed using their adsorbed electron and X-ray images.

2.6 Techniques Used to Determine the Extent of the Mixing in the Metal Pool

2.6.1 Sulphur Prints

A mixture of iron sulphide and tungsten powder was added to the melt using the technique described in Section 2.5.2. The pool profile outlined by the sulphur rich metal on the sulphur print was then compared with the profile outlined in the metal by the tungsten powder.

2.6.2 Sulphur Concentration Analysis

A controlled amount of iron sulphide was added to a melt in which solidification was allowed to proceed under steady-state conditions.

The ingot was subsequently sulphur printed and the exact position of the sulphur rich interface located. The change of sulphur concentration moving up the ingot was then determined by a chemical analysis of drillings taken at finite intervals along the centerline.

2.6.3 Radioactive Tin Concentration Analysis

Radioactive tin was introduced into the melt using the same technique outlined in Section 2.5.3. Thermal stability was maintained and the resulting autoradiograph was used to locate the tin rich interface. Drillings taken at finite intervals along the centerline were then monitored to give a concentration profile for the tin.

2.7 Determination of the Solidification Rate

2.7.1 Melt Record

The average solidification rate for 100 to 200 second intervals can be determined from the melt record. The parameters involved in this determination are the ratio of electrode to ingot diameters and the rate of electrode travel.

2.7.2 Tungsten Powder Addition

An alternate method for determining the solidification rate was the external addition of tungsten powder. The powder was added in the same manner as outlined for the addition of the iron sulphide to the melt. The additions were made at specific time intervals. Surface grinding the resulting ingot clearly shows up the tungsten bands and hence an average solidification rate can be determined.

2.8 Determination of the Heat Transfer in the System during the "Power-Off" Mode

Most of the available heat transfer data concerning the ESR unit pertains primarily to the steady state condition. It was necessary, therefore, to investigate the rates of heat transfer from the metal, the slag,and across the slag/metal interface during the "power-off" mode. The rates of heat loss from the slag and the metal to the mould cooling water were obtained by performing a series of "power-off" experiments in a mould which had thermocouples attached along its length. The configuration is shown schematically in Figure 9. Copper/constantan integral thermocouples were used to measure the change in the mould wall temperature under "power-off" conditions. Constantan wires (0.0254 cm dia.) were embedded in 0.1 cm diameter x 0.125 cm deep holes in the copper mould, and were plugged by 0.1 cm diameter copper wire. The copper mould was the positive terminal and cold junctions were maintained at 0°C by immersing them in ice cooled glass tubes containing mercury.

The experimental problems associated with temperature measurements inside an operating ESR unit are enormous. The high temperatures, intense magnetic fields, and high potentials present combined with the corrosive nature of the slag provide a formidable barrier to precise temperature measurements.

A series of trial and error experiments led to the thermocouple design shown in Figure 10. The boron nitride provided good protection as it was compatible with the W-3Re/W-25Re (0.092 cm dia.) thermocouple wire, and acted as an electrical insulator at the temperatures experienced. The boron nitride also resisted attack by the ESR slag

for a considerable time. The thermocouple tip was immersed in powdered graphite to prevent any oxidation of the thermocouple wires, and to provide some electrical conduction in the event of a wire break at the tip. The temperatures were read out to a Sargent model SR-4 recorder.

The procedure used to obtain the change in the slag and metal temperatures at the slag/metal interface resulting from a loss in power, was a trial and error immersion of the thermocouple into the system. The thermocouple was slowly lowered into the slag until a realistic temperature was being detected then the power was switched off, and the resulting temperature changes recorded. Once the power was terminated the termocouple became trapped in the slag cap or the ingot, so that its exact position could be determined.

2.9 Determination of the Volume Solidified during a Short Power Interruption

This experiment involved the external addition of approximately 15 g of tungsten powder between the electrode and the mould wall in a 10 cm diameter mould. At the same instant the powder was added to the system, the power was turned off. After a time interval ranging from 10 to 15 seconds a similar quantity of powder was added and simultaneously the machine was turned back on.

3. STRUCTURAL AND COMPOSITIONAL CHANGES PRODUCED BY PERBURBATIONS IN THE GENERAL HEAT BALANCE OF THE SYSTEM

3.1 An Evaluation of the Segregation and Banding in EN-25 and AISI 4340 Produced by Interruptions in the Power Supply to the System

The effects of the "power-off" condition on the structure and composition of EN-25 and AISI 4340 were investigated using various techniques. Although most of the experiments were performed using EN-25 as the electrode material, it was necessary to use AISI 4340 when EN-25 was not available. It should be noted, however, that the compositions of these two alloys are very similar.

3.1.1 The Nature of the Structural and Compositional Changes

The first step in the investigation was to determine the effects that power interruptions have on the ingot structure. To get a better understanding of these effects, however, the steady state structure was determined for the purpose of comparison. Ingot no. 1 was produced under steady state conditions and is shown in Figure 11. The structure is very uniform and has a well defined axial growth direction.

Having determined the steady state structure ingots no. 2 and no. 3 were produced containing deliberate power interruptions ranging in duration from 8 seconds to 65 seconds. Figure 12 shows ingot no. 3

etched with Oberhoffer's reagent. The effected regions are clearly marked by the light coloured bands. A micrograph of the 18 second power interruption region was examined to see if the light bands could be accounted for by a change in the ingot structure (Figure 13). The center of the banded region appears to show some refinement in the structure, but nearer the edges the dendrites have continued to grow with little or no change in their primary arm spacing.

Another possibility was that the lightly etched bands were associated with compositional changes in the effected regions. Considering the alloying elements present in the two steels, and their maximum concentrations in the liquid (Co/k_o) the three elements most likely to show any detectable change in concentration were carbon, nickel, and chromium. To check the possibility that the bands were produced by changes in the carbon concentration ingots no. 2 and no. 3 were etched with 3 percent nital which is used to indicate decarburization in steels (Figure 14). Comparing Figures 12 and 14 it can be seen that the previously light coloured bands etched up dark in the 3 percent nital. This indicated that the bands are probably regions of carbon enriched steel.

The banded regions were also analyzed for fluctuations in the concentration of both nickel and chromium on the electron probe. Step-scanning specimens from ingots no. 2 and no. 3, however, revealed no significant variations in the concentration of either element.

3.1.2 The Origin of the Carbon-Rich Bands

A possible explanation for the origin of the carbon rich regions has been proposed. For convenience the proposed model has been

divided into three stages: 1) turning the power off, 2) turning the power back on, and 3) re-establishing equilibrium conditions. The three stages are shown schematically in Figure 15.

Stage I

In the initial seconds of the "power off" mode, solidification in the metal pool would proceed normally, with the possible exception of the liquid metal in contact with the slag skin adjacent to the mould. Due to the high heat transfer in this region, this metal could begin to solidify. A general delay in the metal system's response to the "power-off" condition would probably occur, however, because the steady state heat supply to the metal pool would be in part maintained. As this flow of heat diminished with time the solidification rate in the system would gradually increase. As the liquid metal continued to solidify the relative concentration of carbon in the liquid would increase since the volume of liquid metal would be steadily diminishing.

The liquid slag, on the other hand, would cool rapidly because of its much higher rate of heat loss, and because its heat supply is primarily due to resistance heating. It would, therefore, begin to solidify; initially at the edges and top, and then around the electrode tip. As the slag skin at the edges and the top thickened the rate of heat loss from the system would decrease, reducing the solidification rate.

Stage II

When the power supply to the system is turned back on the electrode melt rate would be higher than its equilibrium value. The reason for this higher melt rate is that the heat generation in the molten slag would be increased for a given power input, because of the

liquid slag's reduced volume. The increased melt rate would have two main effects on the metal pool system. Firstly, there would be a large flux of heat into the remaining liquid metal pool. This heat would cause the solidification rate to decrease, and in cases where the liquid pool was completely or almost completely solidified it could result in some remelting of the interface. Secondly, the increased volume of liquid metal would result in a height of liquid metal (H_L) being established at the edge of the ingot. The net result of these two effects would be a much deeper liquid metal pool profile than the equilibrium configuration. Another effect of the increased heat generation in the slag during this stage would be the remelting of some of the slag that solidified during the "power-off" mode.

Stage III

As the volume of molten slag returns to its equilibrium value, the electrode melt rate would be decreased, reducing the heat supply to the metal system. Therefore, with the system returning to its thermodynamic steady state, the deep metal pool would become progressively less stable. In order for the pool to re-achieve its equilibrium configuration, the solidification rate in the center region of the ingot must increase. The result of the increased solidification rate is that the effective distribution coefficient (K_E) for carbon in the system would approach unity. As the value of K_E increases the concentration of carbon in the solidifying metal would be increased.

This proposed explanation for the origin of the carbon rich bands has been substantiated by several experimental results. Firstly, the fact that liquid metal enrichment by carbon does occur during the

"power-off" mode is supported by the carbon rich patches, which represent the final volume of liquid metal to freeze at the top of all the AISI 4340 and EN-25 ingots examined. These patches are clearly shown at the top of ingot no. 1 in Figure 11. Secondly, the possibility that the carbon rich bands were produced by an increase in the solidification rate when the power was turned off, was disproved by the fact that no transverse banding was observed in the final liquid pool of any of the ingots produced. This implied, therefore, that the carbon rich regions were associated with the power being re-established. Thirdly, it was shown with the use of tungsten powder additions during a long "power-off" experiment, that when the power was turned back on the resulting pool profile was very deep in the center part of the ingot (Figure 16). Particles of tungsten powder can be seen at the bottom of the carbon rich band. In this case there was undoubtedly some remelting of the equiaxed zone when the power was turned on. Finally, the photographs of ingots no. 2 and no. 3 (Figure 14) show that most of the banded regions are composed of many smaller bands which extend for some distance after the power has been turned back on. This phenomenon can readily be explained in terms of the temperature gradient that exists in the liquid metal at this stage. Because the heat content of the metal pool would not have been completely re-established the temperature gradient in the liquid would be lower than its equilibrium value. This would make the solidification rate much more sensitive to any change in the thermal conditions. Therefore, the fluctuations in the power input while the system was re-establishing its equilibrium thermal conditions would be

sufficient to produce the "step-like" banded structure.

On the basis of this experimental evidence, therefore, it appears that the proposed model is a realistic explanation of how the carbon rich bands are formed.

3.1.3 Alternative Techniques Employed to Investigate the Nature of the Segregation and Banding in EN-25 and AISI 4340 Produced by Interruption in the Power Supply

Two alternative techniques were used to investigate the effects of an interruption in the power supply on the ingots structure and composition. The two techniques employed were sulphur printing and autoradiography.

3.1.3.1 Sulphur Printing

Iron sulphide pellets were added to the melt as outlined in Section 2.5.2. Because the solubility of sulphur in solid iron is very low,[19] iron sulphide inclusions are formed when the sulphur rich metal solidifies. When a sulphur print is made of the sulphide rich zone, the iron sulphide inclusions evolve H_2S which reacts with the photographic paper turning it brown.

Figure 17 shows a sulphur print made from ingot no. 6 which contains several power interruption experiments. The dendritic structure of the ingot and the pool profiles at the time of each addition have been clearly outlined. The effects of the power interruptions on the composition of the ingot, however, are not

clearly represented on the sulphur print. There appears to be very little solute enrichment even in the longer"power-off" experiments. Because sulphur has a low distribution coefficient ($k_o = 0.1$)[19] more sulphur enrichment was expected. Due to the crude nature of the sulphur printing technique, however, the changes in sulphur concentration were probably too small to be detected.

3.1.3.2 Autoradiography

Radioactive tin was introduced into the metal pool as outlined in Section 2.5.3. and several power interruption experiments were performed. Figure 18 shows the autoradiograph for a section of ingot no. 11 in which the power was shut off for 23 seconds. The power was shut off approximately 5 seconds after the radioactive tin entered the metal pool.

The autoradiograph shows no change in the dendritic structure as a result of the power being turned off. There is, however, a tin rich band which is very similar to the carbon rich bands found by etching. This tin rich region was probably formed in the same manner as outlined in Section 3.1.2 for the formation of the carbon rich bands.

3.2 The Effect of the Slag Skin on the Formation of Carbon Rich Bands in EN-25 and AISI 4340 during Steady State Production

Banding during the steady state production of high carbon alloy steels (e.g. AISI 51100) is common. This "tree-ring" banding is clearly shown in Figure 19 which is a high carbon alloy steel produced by vacuum arc remelting. This type of banding can occur in steels with a

much lower carbon content, however, if there are significant irregularities in the slag skin thickness. Such irregularities in the slag skin thickness are produced by discontinuous changes in the electrode movement, or in the power settings.

Since the slag skin forms on the edge of the copper mould before the metal freezes, any irregularities in its thickness replicate themselves on the ingot surface. This effect can be clearly seen in Figure 20. Because the rate of heat removal radially from the metal pool is inversely proportional to the slag skin thickness, any irregularities in the thickness will effect the thermal stability of the system. The result of such thermal instabilities can be seen in Figure 21. This is a photograph of the top of ingot no. 13 and shows a series of carbon rich bands near the edge of the ingot. The way these bands are formed can be explained in terms of the schematic diagram shown in Figure 22. At point A the liquid metal would be solidifying at a rate which would be in part governed by the slag skin thickness (ΔX). Assuming that ΔX at point A is greater than the normal value, the solification rate at this point would be slower than the equilibrium rate. Because of the decreased solidification rate, the K_E value for carbon in the system would decrease and a thicker solute rich band would develop in front of the interface at point A. As the profile continued to advance towards point B, the solidification rate would increase due to the decreasing value of ΔX. As the rate increased, K_E would move towards unity and some of the carbon rich metal ahead of the interface would be solidified in producing a small concentration band. With the continued advance of the interface to point C the sequence would repeat itself.

3.3 An Evaluation of the Segregation and Banding in AISI 630

The effects of the "power-off" condition on the structure and composition of AISI 630 were investigated.

3.3.1 Structural Changes

The structural changes that resulted from the "power-off" condition were clearly revealed by a standard macro-etchant (Figure 23). The macrograph shows that there was a marked change in the steady state growth direction, particularly at the edges of the ingot where the maximum rate of heat loss occurs. It was also observed the growth direction of the grains near the centerline of the ingot became more radially inclined. A possible cause of this reorientation is that when the power was restored the solidification rate near the center of the ingot was suppressed resulting in a deeper pool profile. This would occur in the same manner as discussed in Section 3.1.2. Because of the low crystal growth anisotropy exhibited by AISI 630, the re-nucleated grains would tend to grow perpendicular to the new profile resulting in the more radially inclined orientation.

3.3.2 Compositional Changes

In order to determine whether or not the "power-off" condition produced any anomalies in the steady state composition of AISI 630, specimens were quantitatively analyzed on the electron probe. Specimens taken from ingot no. 14 (Figure 24) were scanned for nickel, chromium and copper. The microprobe survey of specimens A-1, A-2, B-1, and B-2 revealed no significant variation in the concentrations of the

three elements when compared with the steady state concentrations found in specimens C-1 and C-2.

3.3.3 Commercial Castings

Stainless steel ingots have been produced commercially, however, which do exhibit significant concentration banding (Figure 25). This is an AISI 630 grade stainless steel ingot which was produced by the Arcos Corporations continuous casting ESR process (Figure 26). The original section was cast in an 8 inch square mould and was subsequently hot rolled down to a 5.5 inch by 3.5 inch billet.

During normal operation on the above furnace, ingots are removed from an open-bottomed copper mould at a constant rate. The banded structure (Figure 25) probably resulted from a non-uniform withdrawal rate caused by the casting sticking in the mould.

In order to determine the exact nature of the banded structure, specimens were taken from both the banded and uniform regions of the ingot (Figure 27). An initial examination was done by etching the specimens with Vilella's and Kalling's reagents. The results showed that the dark bands contained a high percentage of the δ-ferrite phase (Figure 28). The next step was to determine the concentrations of the main alloying elements in the banded regions. Using the electron probe, the δ-ferrite particles were found to be high in chromium and low in both nickel and copper. Figure 29 shows the X-ray images for chromium and nickel in a banded region. The actual concentrations of chromium, nickel and copper in the areas of interest are shown in Table IV.

Table IV. Element concentrations in the banded regions.

Area	Ni wt.%	Cr wt.%	Cu wt.%
Steady-state region	4.58	15.51	3.40
δ-Ferrite particle	2.44	17.69	2.32
Inter-ferritic region	4.54	13.70	3.83
Non-ferrite band	4.05	11.28	3.48

In order to understand how the δ-ferrite bands formed and their effect on the mechanical properties of the steel, it was necesaary to examine the thermal history of an AISI 630 stainless steel. The 630 grade of stainless steel has been classified as a martensitic, precipitation-hardening steel. At the solution treating temperature of 1038°C the metal is austenitic and undergoes the transformation to martensite on cooling to room temperature. This transformation starts at approximately 132°C but is not complete until the temperature drops to around 32°C. The precipitation hardening compounds remain in solution as the metal cools. Subsequent heating to temperatures around 500 to 625°C for one to four hours precipitates the small particles that increase the steels strength and hardness.

The key to this precipitation hardening mechanism is that the solution treatment is carried out in the single phase austenitic region. Since the size and position of the different phase regions

are strongly dependent on the concentration of the alloying elements present, the composition of the steel must be carefully controlled. Figure 30 shows how the size of the two phase region is increased as the nickel concentration is decreased.

The δ-ferrite bands, therefore, probably formed because the steel composition in these areas was outside the specification range causing the solution treatment to occur in the two phase region. During the subsequent heat treatments the δ-ferrite phase was retained throughout, resulting in a mixture of austenite, martensite, and bands of δ-ferrite. Since the copper is less soluble in the δ-ferrite phase, the ferrite particles would not harden to the same extent as the matrix metal. The result, therefore, would be bands of weaker material that could deform at a lower stress level.

The specifications on AISI 630 allow for a maximum of 5 to 7 percent ferrite in the matrix.[20] The Schaeffler ferrite diagram shown in Figure 31 demonstrates how closely the composition of the steel must be controlled in order to keep the ferrite content within the specified range. Using this diagram the ferrite content of the unbanded regions was approximately 4 percent. In order to determine the ferrite content of the banded regions a standard line count was employed (Figure 32). The results indicated that the bands contained approximately 19 percent ferrite and therefore were well outside the specified range. The result of this increased ferrite content can be seen in Figure 33. This shows a section from the casting which has cracked along the banded structure during rolling.

4. MIXING IN THE LIQUID METAL POOL

In order to get a better understanding of the mixing in the metal pool it was important to examine both the origin and the extent of this mixing action.

4.1 Origin of the Mixing Action

With regard to the origin of the mixing action there are three main possibilites to consider: 1) thermal convection, 2) electromagnetic stirring, and 3) momentum and heat transfer from the falling drops. Generally the degree of thermal convection in the liquid metal would be negligible as the regions of highest temperature exist at the top of the molten pool. The degree of thermal convection could become significant only if the pool profile became deeply curved causing the isotherms in the liquid metal to have a pronounced curvature. It is unlikely that this situation would arise in a commercial ingot, however, as the pool depth is generally proportional to the ingot radius and therefore, relatively quite shallow.

The second possible cause of mixing in the liquid pool is electromagnetic stirring. Initiating this type of mixing are the Lorentz forces created around an electrically active conductor. These produce a magnetic field with which the current can interact.

However, such interactions with current path fields are essentially a function of the furnace's electrical configuration and, as such, are very unpredictable.

Electromagnetic stirring can be deliberately created, however, by imposing a magnetic field on the liquid pool. This technique is frequently employed in VAR furnaces where the field created by the radial coils (Figure 34-A) interacts with the large horizontal current component to produce a force on the liquid metal. This force causes the liquid metal to pile up against the mould wall in the force direction. By cycling the current in the coils at a low frequency (approximately 0.1 cps), the force direction changes and produces an oscillation of the liquid metal. A rotational mixing effect is also produced due to the slight asymmetry of the radial coils.

In a normal ESR unit (Figure 34-B) the main current component is parallel to the induced magnetic field; consequently there are no Lorentz forces created. The only exceptions are ESR machines operating with a live mould connection such as those converted from VAR units. This type of mould connection has a large horizontal current component, but it is primarily confined to the top of the slag. The result is a high degree of electromagnetic stirring in the slag. Therefore, the only way electromagnetic stirring could be induced in a normal ESR unit would be to produce a magnetic field with a horizontal component (Figure 34-C). However, in order to produce a field of sufficient strength in the liquid metal with this type of coil, a very large power input is required. This fact makes

the technique difficult to achieve in a mechanical sense, particularly as the ingot sizes increase. The foregoing discussion applies to direct current furnaces only. In furnaces employing alternating current, the interactions are much more complex, but the net effect is to produce only small forces.

The third and most likely cause of mixing in the liquid pool is momentum and heat transfer to the liquid metal by the falling droplets.[21] The type of convective motion set up in the system by the falling drops is shown schematically in Figure 35. The momentum of the falling drops carries them down into the pool entraining liquid behind them. Then, because of their higher temperature they tend to spread out and rise. At industrial melt rates (1200 to 1500 lbs hr^{-1}) sufficient momentum would be transfered to the metal pool to produce a continuous mixing action.

4.2 Evaluation of the Mixing Action

In order to evaluate the mixing action experimentally, 0.26 g of radioactive tin was added to the metal pool using the technique outlined in Section 2.5.2. Adding the tin in this manner would simulate the behaviour of the falling metal droplets, and if mixing was primarily due to heat and momentum transfer the following results would be expected.

1) The mixing action would be sufficient to allow the radioactive tin to outline the shape of the pool profile.

2) The mixing action would be sufficient to approach a state of complete mixing at the solidification rates used for ESR production

(0.005 to 0.03 cm sec^{-1}).

3) Due to the dendritic nature of the solidifying interface, the effective distribution coefficient (K_E) of the tin would approach unity (k_o = 0.67).[22]

The results of the radioactive tin experiment were consistent with the predicted results. Figure 36 is an autoradiograph of the metal pool which clearly outlines the pool profile. The rate of depletion of the tin with axial distance from the original interface was experimentally determined by monitoring drillings taken at finite intervals along the centerline of the ingot. Figure 37 shows a plot of the normalized concentrations of radioactive tin versus axial distance from the original interface (Appendix I-A). A theoretical curve was then plotted based on the assumptions that there was complete mixing in the liquid pool, and that the effective distribution coefficient for the tin was unity (Appendix I-B). The resulting profile showed very good agreement with the experimental curve indicating the predictions were essentially correct. The small deviation near the interface could indicate that there was some solute enrichment of the liquid metal.

A similar set of experiments were carried out using sulphur to determine the extent of the mixing in the liquid pool under steady state conditions. Iron sulphide mixed with tungsten powder was externally added to the system and the pool profile outlined by a sulphur print was compared with the profile outlined by the tungsten powder. The two profiles are shown in Figure 38. Since the two profiles are identical this implies that sulfur printing accurately

outlines the pool profile.

The rate of depletion of sulphur from the original interface was also determined. Drillings were taken from ingots no. 4 and no. 5 and were analyzed for their sulphur concentration. The resulting concentration profile for ingot no. 4 is shown in Figure 39. Because sulphur has a much lower k_o value than tin ($(k_o)_S = 0.1$), its concentration profile was expected to show more macrosegregation. Examining the profiles it can be seen that the concentration of sulphur does initially drop below the theoretical profile, but maintains a higher concentration at larger distances from the original interface.

On the basis of this information, therefore, several proposals can be made concerning the extent of the mixing action in the metal pool system. Firstly, the mixing is probably produced by a slow convective motion, which at the very slow solidification rates used in ESR production approaches a state of complete mixing. Secondly elements with k_o values between 0.5 and 1.0 (eg.Cr,Ni,Sn) would probably have very little macrosegregation associated with them, and their concentration would be relatively uneffected by a disruption in the power supply to the system. Thirdly, elements with k_o values below 0.5 (eg. C,S,P) could show some macrosegregation and their local concentration could be effected by an interruption in the power supply.

5. THERMAL PARAMETERS

During the construction of a simple heat balance for the slag and metal pool systems during the "power-off" mode, it became apparent that a better understanding of the liquid metal's superheat and the heat losses from the system during the "power-off" mode were necessary.

5.1 Evaluation of the Superheat in the Liquid Metal Pool

In order to get a better understanding of this parameter a series of calculations were carried out using different assumed temperature configurations in the metal pool. Since the liquid metal's superheat is directly proportional to ΔT_S ($\Delta T_S = T - T_{m.p.}$) this parameter will be used to represent the heat content.

5.1.1 ESR: 10 cm dia. ingot

To simplify the calculation, the pool geometry was assumed to be cylindrical. The height of the cylindrical pool was calculated so that it contained the same volume of liquid metal as the actual pool. Based on known temperatures in the system the limiting values for the temperature distribution were chosen.[23] The assumed pool geometry and the imposed boundary temperatures are shown in Figure 40.

The cylindrical metal pool was divided into segments having an arc of 1 radian (Figure 41). Suitable Δz and Δr values were chosen based on the dimensions of the cylindrical pool.

z' direction: 4 elements with $\Delta z = 0.5$ cm

1 element with $\Delta z = 0.25$ cm

r' direction: 5 elements with $\Delta r = 1$ cm.

The volume of each element was calculated using the general formula

$$\text{volume} = \text{base} \times \text{height}$$

$$V = 1/2[(r'\Delta r + \frac{\Delta r}{2})^2 - (r'\Delta r - \frac{\Delta r}{2})^2]\Delta z \qquad (5.1.1)$$

where Δr = the unit length

r' = the number of units away from the centerline.

Therefore for all the units with $r' > 0$

$$(V)_{r'>0} = r'\Delta r^2 \Delta z \qquad (5.1.2)$$

And for the triangular unit at the center where $r' = 0$ and $\Delta r = \frac{\Delta r}{2}$

$$(V)_{r'=0} = \frac{\Delta r^2 \Delta z}{8} \qquad (5.1.3)$$

Knowning the volume of each element it was possible to calculate the amount of superheat associated with each one of them for a given temperature distribution in the metal pool. For the purpose of this calculation it was assumed that the temperature distribution in the z direction was a linear function of z. The assumed temperature

distribution in the z direction is shown in Figure 42. From Figure 42 the maximum and minimum temperatures for each layer of cubes in the z' direction could be determined. These became the end points for the temperature distributions in the r' direction. Because the rate of heat transfer near the edges of the ingot would be much higher than the rate at the center, the temperature distribution in the r' direction could not be approximated by a linear function of r'. To compensate for this a series of temperature distribution curves were drawn which climbed rapidly near the edges and flattened out towards the center (Figure 43). Using Figure 43 $T_{r',z'}$ could be determined for each element.

Having determined the volume and temperature of each element it was then possible to calculate the amount of superheat associated with each one.

$$Q_S = mCp\ \Delta T_s$$

$$= (Cp\rho)V\Delta T_s \qquad (5.1.4)$$

where

$$\Delta T_s = T_{(r',z')} - 1500°C$$

Therefore, the average superheat for the entire cylinder can be determined as follows:

$$(\Delta T_s)_{Avg} = 2\pi\Sigma \frac{V\Delta T_s}{V_T} \qquad (5.1.5)$$

$$= \frac{10.40 \times 10^3}{178} \quad °C$$

$$= 58.4°C$$

In order to get some estimate of the range of $(\Delta T_s)_{Avg}$, the same calculation was done for two different temperature configurations. The distributions investigated and the resulting $(\Delta T_s)_{Avg}$ values are shown in Figures 44-A and 44-B. The results show that in a 10 cm diameter ingot of EN-25 or AISI 4340 the upper limit of $(\Delta T_s)_{Avg}$ is approximately 86°C and the lower limit of $(\Delta T_s)_{Avg}$ is approximately 47°C.

5.1.2 ESR: 61 cm diameter and 254 cm diameter

Approximate values of $(\Delta T_s)_{Avg}$ for industrial sized ingots were evaluated using the same technique demonstrated above. Two ingot sizes were examined: 1) 61 cm diameter and 2) 254 cm diameter. In both cases a cylindrical approximation for the pool shape was used. The assumed temperature distribution and the resulting $(\Delta T_s)_{Avg}$ values are shown in Figures 44-D and 44-E.

Based on these results it appears that the magnitude of $(\Delta T_s)_{Avg}$ increases very slowly with increasing ingot diameters.

5.1.3 VAR: 10 cm diameter

For the purpose of comparison, $(\Delta T_s)_{Avg}$ was calculated for a 10 cm diameter VAR ingot. Since the pool profile for this size of VAR ingot is V-shaped the pool was sectioned into a series of cones.

Figure 45 shows the pool geometry and assumed limiting temperatures. Although no direct measurement of the metal temperature below the electrode has been made, it is generally agreed that it falls in the range of 1800°C to 1900°C.[24] Therefore, the temperature in this region was assumed to be 1850°C. The top edge temperature was assumed to be at the melting point, as during normal VAR operation the height of liquid metal at the ingot surface is zero.

For the purpose of simplifying the calculation the temperature distribution in the z direction was assumed to be a linear function of z (Figure 46-A). The temperature distribution in the r direction however, was assumed to rise near the edge and taper off towards the center (Figure 46-B).

The volume of each conical element was calculated as follows:

$$\text{Volume} = (\text{Volume})_n - (\text{Volume})_{n-1}$$

$$= \frac{\pi}{3}\left[(r_n)^2 z_n - (r_{n-1})^2 z_{n-1}\right] \qquad (5.1.6)$$

where n = the number of the element being considered. The particular values of r and z for each element were determined from Figures 46-A and 46-B using temperature increments of 50°C. Knowing the average temperature of each element and its volume, it was then possible to determine the value of $V\Delta T_s$ for the entire metal pool. The average superheat ($(\Delta T_s)_{Avg}$) for the metal pool was then calculated.

$$(\Delta T_s)_{Avg} = \frac{V\Delta T_s}{V} \qquad (5.1.7)$$

$$= 121°C$$

The results of this comparison show that the metal pool during VAR production contains much more effective superheat than the metal pool during the ESR production of the same diameter ingot. This additional superheat produces the very deep metal pools associated with VAR ingots. As a result of the differences in pool depth between the two processes, several differences in the structure and quality of the final product can be seen;

1) VAR ingots have a much more radially oriented growth direction than those found in similar ESR ingots.

2) VAR ingots contain more shrinkage porosity and piping than similar ESR ingots.

5.2 Heat Transfer during the "Power-Off" Mode

Recently, there has been a great deal of information available concerning the rate of heat transfer from the slag and metal pool systems during the steady state.[25] This data could not be applied to the "power-off" condition, however, as many of the heat transfer parameters are changed during this period.

There are four main areas affected by the loss of heat input into the system (Figure 47).

1) The liquid metal/slag skin interface: Heat transfer in this region would be reduced by solidification of the metal at this interface and contraction of the ingot away from the water-cooled mould.

2) The liquid slag/slag skin interface: Heat transfer in this region would be reduced by solidification of the slag at this interface.

3) The liquid slag/atmosphere interface: The heat transfer in

this region would be reduced as the surface temperature of the slag decreased.

4) The liquid metal/liquid slag interface: The heat transfer in this region would change as the relative temperature between the two liquids changed and as physical nature of this interface changed.

To calculate the heat transfer profiles across the various interfaces during the "power-off" mode, a series of experiments were performed as outlined in Section 2.8. The apparatus and general procedure used have been discussed in detail by Joshi.[25]

5.2.1 Heat Transfer Across the Liquid Metal/Slag Skin Interface

Thermocouples in the mould recorded the change in the cooling water temperature with time during the "power-off" mode (Figure 48). This data was then converted to a rate of heat flow per unit area ($\dot{q}/A$) using Figure 49. Lines 1 and 3 on Figure 49 were used to determine $\dot{q}/A$ as they most accurately described this system. Knowing the surface area of each interface it was then possible to plot the total heat loss across each one against the duration of the "power-off" condition (Figure 50).

5.2.2 Heat Transfer Across the Liquid Slag/Slag Skin Interface

Employing the same technique illustrated above a rate of heat loss versus time curve for the "power-off" condition was calculated for the liquid slag/slag skin interface (Figure 50).

5.2.3 Heat Transfer Across the Liquid Slag/Atmosphere Interface

Employing the same technique illustrated above a rate of heat loss versus time curve for the "power-off" condition was calculated for the liquid slag/atmosphere interface (Figure 50).

5.2.4 Heat Transfer Across the Liquid Metal/Liquid Slag Interface

In order to determine the nature of the heat transfer across the slag/metal interface during the "power-off" mode, it was necessary to establish the temperature profiles on either side of the interface. Because of the experimental difficulty involved, however, only the profile for the slag was obtained. It was necessary, therefore, to approximate the metal temperature profile in order to get some estimate of the heat transfer across the slag/metal interface. The equilibrium metal temperature, directly below where the slag profile was obtained was estimated from the temperature profiles used in Section 5.1.1. Also, the time required for the metal in this area to begin solidifying was estimated to be approximately 15 seconds on the basis of the "power-off" experiments discussed in Section 3.1. Using this information an approximate temperature profile was constructed for the metal at the slag/metal interface. Figure 51 shows the two temperature profiles superimposed on one another. From Figure 51 the temperature difference across the interface ($\Delta T = T_{slag} - T_{metal}$) could be determined for any duration of the "power-off"condition. To calculate the rate of heat transfer, however, it was necessary to know the heat transfer coefficient at the interface (h_I). The actual value of this coefficient has never been accurately measured, although

most authors have used values ranging from 0.1 to 1.0 cal $cm^{-2}{}^{\circ}C^{-1}sec^{-1}$.[26,27] Figure 52 shows the rate of heat transfer per unit area across the slag metal interface during the "power-off" mode, for three assumed values of h_I. These profiles show that within this assumed range of the heat transfer coefficients there are large variations in the magnitude of the heat flow across the interface. To get a clearer understanding of what probably does occur at the interface, therefore, there were three points that must be considered. Firstly, assuming that h_I remains constant during the "power-off" mode, and that the assumed metal temperature profile is a reasonable approximation of the actual profile, then the net heat flow across the interface is approximately zero regardless of the value of h_I chosen. This conclusion is dependent to some extent on the shape of the assumed temperature profile. Reasonable variations in its shape, however, did not change the net heat flow significantly. Secondly, since the heat transfer across the interface is dependent on the degree of mixing, and since the degree of mixing could only decrease during the "power-off" mode, therefore h_I could only decrease in value. The third and most important point is concerned with the changes in the surface area to volume ratio as the ingot size increases. As the size of the ingot increases, the heat flow at the slag/metal interface would become increasingly insignificant when compared with the large heat contents in the metal and slag pools. It was felt on the basis of these considerations, and despite the shortage of data concerning the slag/metal interface, that the heat transfer across this interface during the "power-off" mode could be considered negligible. It was also felt that the validity of this assumption increased with the ingot size.

The resulting profiles revealed several interesting features about the rate of heat transfer from the slag and metal systems during the "power-off" mode. Firstly it can be seen in Figure 50 that the rate of heat loss ($\dot{q}$) from these interfaces drops off very rapidly and that they respond instantaneously to the "power-off" condition. Secondly, Figure 52 shows that the heat transfer across the slag/metal interface is very dependent on the value of the heat transfer coefficient due to the small temperature gradient across this interface. The effectiveness of auxillary electrodes to heat the slag and metal pool systems during an electrode change operation, therefore, will be very dependent on the exact value of this coefficient. If its value is close to 1.0 cal $cm^{-2} sec^{-1} {}^{\circ}C^{-1}$ there will be a considerable amount of heat transfer from the slag to the metal if the original slag temperature is maintained. This heat supply would reduce the extent of the solidification in the metal pool during the electrode change operation and thereby reduce any structural and compositional effects. On the other hand, if the heat transfer coefficient is close to 0.1 cal $cm^{-2} sec^{-1} {}^{\circ}C^{-1}$ the heat transfer across the slag/metal interface would be greatly reduced. The effect of the auxilliary electrodes, therefore, would be mainly confined to maintaining the slag systems temperature, thereby reducing the requirement for slag heating on power resumption.

6. THE EXTENT OF SOLIDIFICATION DURING THE "POWER-OFF" CONDITION

Heat balances were calculated for a small and a large scale ESR ingot as well as a small scale VAR ingot, in order to obtain some estimate of the volume of liquid metal and liquid slag that would solidify during a relatively short interruption in the system's power supply. Although these calculations contained several assumptions and can only be considered as approximations, they do provide a good indication of how the two systems react to the "power-off" condition. To circumvent the complex problems of pool shape change and temperature gradient changes during the "power-off" mode, the calculations were limited to a determination of the volume solidified in a given period of time.

6.1 Determination of the Volume Solidified in the Metal and Slag Pool Systems in a 10 cm dia. EN-25, ESR Ingot

The slag and metal pool configurations used in this calculation are shown in Figure 53.

The first step in this calculation was to determine the available heat contents (Q_A) of the two systems at the beginning of the "power-off" condition (t = 0). This is shown in Appendix II-1. For simplicity it was assumed that both systems retained their sensible heat during the"power-off" mode. Therefore:

$$Q_A = mC_p\Delta T_S + mL \qquad (6.1)$$

and from Appendix II-1

$$(Q_A)_M = 79 \text{ kcals}$$

$$(Q_A)_S = 98 \text{ kcals}$$

Having calculated the available heat content of both systems, the next step was to calculate the total heat loss (Q_L) from each for different durations of the "power-off" mode (Appendix II-2). The results of these calculations are shown in Tables V-A and V-B.

Knowing Q_A and Q_L it was then possible to calculate the volume percent solidified (P.S.) for the different lengths of "power-off" operation.

$$P.S. = \frac{Q_L}{Q_A} \times 100 \qquad (6.2)$$

The results are shown in Tables V-A and V-B.

Plotting the results of Tables V-A and V-B points out several interesting features about each system during the "power-off" mode (Figure 54). It can be seen that the volume percent solidified in the metal pool increases very uniformly with time which indicates that there are no gross changes in the solidification rate associated with the early stages of a power interruption. As the duration of the "power-off" condition increases, the heat loss from the system is primarily due to conduction down the ingot, and radially to the mould

Table V.

A. Volume solidified in the metal pool system

Time (sec)	Heat loss (kcals)			Total heat loss (kcals)	Available heat at t=0 (kcals)	Volume % solidified
	q_1	q_2	q_3			
2.5	1.6	1.3	0.3	3.2	79	4.0
5.0	2.8	2.6	0.6	5.9	79	7.5
7.5	3.6	3.8	1.0	8.4	79	10.6
10.0	4.4	5.1	1.3	10.8	79	13.7
12.5	4.9	6.4	1.6	12.9	79	16.4
15.0	5.5	7.7	1.9	15.1	79	19.1
20	6.1	10.2	2.7	19.0	79	24.1
30	6.3	15.3	3.8	25.4	79	32.1

B. Volume solidified in the slag pool system

Time (sec)	Heat loss (kcals)		Total heat loss (kcals)	Available heat at t=o (kcals)	Volume % solidified
	q_4	q_5			
2.0	1.0	4.2	5.2	98	5.3
5.0	2.2	9.6	11.8	98	12
10.0	3.4	14.3	17.7	98	18
15.0	4.3	16.0	20.3	98	20.7
30	5.8	17.5	23.3	98	24

wall. It is possible, however, that in addition there could be some heat transfer from the metal to the slag across the slag/metal interface. Photographs of the final pool volume show that some solidification does take place starting at the slag/metal interface (Figure 21). This phenomenon could supply additional heat to the slag at the expense of the metal pool.

Unlike the liquid metal, the slag system solidified rapidly in the initial stages of the power interruption but the solidifcation rate decreased quickly with time. The rapid drop in the solidification rate is primarily due to the low thermal conductivity of the solidified slag. When the power is turned off, the slag freezes in from the mould walls and the top, and thereby becomes insulated from its major sources of heat loss. Because the slag remains liquid for a much longer time than does the metal it is possible to re-restablish electrical continuity even though the metal pool might have completely solidified.

These results are consistent with the experimental observations and with the model for the formation of carbon concentration bands proposed in Section 3.1.2.

6.2 Volume Percent of Liquid Metal to Solidify Based on Tungsten Powder Addition Experiments

The volume solidified for a given "power-off" period was determined experimentally, for the purpose of checking the validity of the theoretical values obtained in Section 6.1. Tungsten powder was externally added to the system the moment the power supply was shut down and then again approximately 13 seconds ($\pm$ 2 second) later.

Figure 55 shows a section of ingot no. 13 which contains three such experiments. The resulting pool profiles for experiment no. 2 are shown in Figure 56-A, and an approximation of these is shown in Figure 56-B. The volume solidified was estimated by using cylindrical elements to calculate the volume encompassed by each profile. The result of this calculation showed that approximately 18.3 percent of the metal pool had solidified in the "power-off" interval. The results of the other tungsten addition experiments all agreed to within 10 percent of this value. Although the experimental values were slightly higher than the calculated percentages, the agreement is still good considering the assumptions that were made.

Tungsten addition experiments for longer durations were not possible as the top of the slag cap became solid after approximately 15 to 20 seconds of "power-off" operation.

6.3 Determination of the Volume Solidified in the Metal and Slag Pool Systems in a 61 cm dia. Ingot during a 60 Second Power Loss

In an effort to get a better understanding of the "power-off" mode and how it effects the larger commercial furnaces an attempt was made to calculate the approximate volumes of ingot and slag which solidified during a 60 second power interruption. The 60 second time interval was chosen as this is the approximate maximum length of time required to change an electrode in an industrial unit. Due to the lack of information available on the rates of heat transfer in commercial sized ingots, however, it was necessary to include in the analysis several major assumptions. Therefore, the results can only be interpreted

as order of magnitude values. The system is shown schematically in Figure 57.

The first step in the calculation once again, was to determine the available heat content of both the metal and slag pool systems (Appendix III-1). In order to determine the rate of heat loss during the "power-off" period (Appendix III-2) it was necessary to use the data for a 7.6 cm diameter ingot and assume that the heat loss was proportional to the surface area. Joshi used this technique to calculate a steady state heat balance for a 61 cm diameter ingot which was in reasonable agreement with commercially observed results.[25]

The results of the heat balance showed that approximately 10 percent of the metal pool and 10.3 percent of the slag pool would have solidified during a 60 second interruption in the power supply (Appendix III-3). It is unlikely, therefore, that any structural or compositional changes would be produced in the ingot as a result of the power loss. These results are reasonable considering the fact that Q_A is proportional to the volume of liquid (r^3) and Q_L is proportional to its surface area (r^2). Therefore, as the ingot radius increases, the effects of power disruptions on the system are reduced, for a given period of "power-off" operation.

6.4 Determination of the Volume of the Metal Pool Solidified in a 10 cm Diameter AISI 4340, VAR Ingot during a 12.5 Second Power Interruption

Because of a growing interest in the more subtle differences between the ESR and VAR processes, it was significant to investigate how the two

processes differ during the "power-off" mode. Traditionally, it has been felt that the VAR process would be much more sensitive to changes in the operating conditions as there is no hot slag layer to act as a thermal buffer.

In order to make this comparison a heat balance was done for ingot no. V-3 which contains two power interruptions of approximately 12.5 seconds (Figure 58). An approximation of the metal pool profile is shown in Figure 59.

The available heat content of the metal pool was calculated based on the same assumptions used for the 10 cm diameter ESR ingot (Appendix IV-1). Determination of the heat loss from the system during the"power-off" period was complicated by the lack of heat flow data pertaining to this mode of operation in a VAR ingot. Because of this lack of relevant information it was necessary to use the steady state heat loss profiles[28] shown in Figure 60. Using these curves and other available information (Section 5.1) it was possible to obtain an upper limit for the heat loss from the metal pool in 12.5 seconds (Appendix IV-2). Once having determined Q_A and Q_L the volume percent of liquid metal solidified during the "power-off" mode was calculated (Appendix IV-3). The result showed that the maximum amount of liquid metal which could freeze, based on the assumed data, was approximately 32.2 percent.

In order to determine whether or not the heat flow values used in the calculation were at all reasonable, the theoretical volume solidified was compared with the experimentally observed value. The two power interruptions and the final pool volume for ingot no. V-3 are clearly

outlined in Figure 58. The dark band produced by the second power interruption has been approximated in Figure 62 by two parabolas. The volume solidified was determined as follows:

$$\text{Volume percent solidified} = \frac{\pi\left[\int_0^{12} y_1^2\,dx - \int_0^{11} y_2^2\,dx\right] \times 100}{\pi\left[\int_o^{12} y_1^2\,dx\right]} \qquad (6.3)$$

$$= 18.5\%$$

It can be seen that the calculated value was approximately 1.7 times higher than the experimentally observed result. The error in the calculated value probably arose by using the radial heat flux profiles for the steady-state condition. It appears, therefore, that the radial heat flux is reduced during the "power-off" conditon and that the steady state profiles cannot be applied to this mode of operation. It should be noted, however, that despite the fact that the volume fractions solidified in 12.5 seconds were approximately the same for the two processes, the much larger volume of liquid metal in the VAR pool (V_{VAR}/V_{ESR} = 3.4) means that more metal solidified. It should also be noted in Figure 58 that the two power interruptions and the final pool volume have all etched up darker than the steady-state sections of the ingot using 3 percent nital. This indicates some increase in the carbon concentration. The probable cause of the increased carbon concentration is an increase in the system's solidification rate. Based on the limited information available, therefore, it

appears that interruptions in the VAR power supply produce a greater effect on the ingot's composition than do similar interruptions in an ESR unit.

7. ELECTRODE CHANGE OPERATIONS

In the previous section it was shown that in the time required to change the electrode in a 61 cm diameter tandem electrode machine only about 10 percent of the liquid metal and liquid slag would be solidified. However, this calculation did not take into account the addition of the new electrode into the system. In order to determine the overall effect of an electrode change on the heat balance, therefore, it was necessary to obtain an estimate of how the new electrode would influence the system.

7.1 Temperature Profile in a Commercial Electrode

Although temperature profiles have been experimentally determined for lab scale electrodes, no practical measurements have been carried out on the much larger commercial electrodes. To estimate the temperature distribution in these electrodes, therefore, profiles were calculated using the unsteady-state heat conduction equation. To simplify the calculation the electrode was approximated by a semi-infinite slab in which there was no heat loss in the radial direction. This assumption is justified based on the results of Mitchell and Szekely [27] who found that the radial heat flow component in the lab scale electrodes was very small. It was also assumed that the electrode tip was flat and that there was negligible immersion into the

slag bath. This is a reasonable assumption based on the observations made during industrial ESR production.

The general form of the unsteady-state heat conduction equation is:[32]

$$\alpha \frac{\partial^2 T}{\partial y^2} = \frac{\partial T}{\partial t} \qquad 0 \leq y \leq \infty \tag{7.1}$$

The boundary conditions for the addition of a new electrode into the system are:

1. $T = T_o$ at $t = 0$ $\quad y > 0$

2. $T \rightarrow T_o$ as $y \rightarrow \infty$

3. $h(T_b - T_o) = -K \frac{\partial T}{\partial y}$ at $y = 0$

where T_o is the initial temperature of the new electrode

T_b is the slag temperature.

Using these boundary conditions the solution to equation (7.1) has the form:

$$T(y,t) = (T_b - T_o)\left[\operatorname{erfc} \frac{y}{2\sqrt{\alpha t}} - e^{h'y + h'^2 \alpha t} \operatorname{erfc}\left(\frac{y}{2\sqrt{\alpha t}} + h\sqrt{\alpha t}\right)\right] \tag{7.2}$$

where h = the heat transfer coefficient across the base of the new electrode

$$h' = \frac{h}{K}$$

Using equation (7.2), therefore, it was possible to calculate the

temperature in the electrode at any position along its length (y) at any time (t), with the assumption that T_b remains constant. A general computer program was written for equation (7.2) and is shown in Appendix V.

7.2 Heat Content of a Commercial Electrode

In commercial ESR operations the minimum practical electrode to ingot diameter ratio is approximately 0.75. Therefore, for a 61 cm diameter ingot a 45.6 cm diameter electrode would be used. Having established the electrode size to be considered in the calculation the next step was a determination of the constants in equation (7.2).

Average values of ρ_s, Cp_s, and K_s for iron in the temperature range from 25°C to 1500°C of 7.8 g per cm^3, 0.16 cal per g °C, and 0.071 cal per cm sec °C, respectively were used in the calculations. Based on the results of Mitchell et al.,[27] and Elliot et al.[26] the heat transfer coefficient (h) at the electrode tip was assumed to be 0.04 cal per cm^2sec °C. It was later shown, however, that the calculation was insensitive to the value of h in the accepted range of values for the electrode tip (0.01 to 0.1 cal per cm^2sec °C). The reason for this insensitivity is that for this range of heat transfer coefficients the rate controlling step is conduction in the electrode and not the rate of heat supply to the electrode base.

Using the above information and assuming the initial temperature (T_o) was 25°C temperature profiles were calculated as a function of time for two assumed values of the slag bath temperature (T_b). The resulting profiles are shown in Figure 63. These profiles represent

the temperature distribution in the electrode at the instant the temperature of the metal 1.0 mm above the slag/electrode interface reached the melting point. The increased heat content of the electrode for both slag bath temperatures was then calculated using graphical integration.

Since $$Q_I = mC_p\Delta T \tag{7.3}$$

$$= V\rho C_p\Delta T$$

$$= \pi r^2 h\rho C_p\Delta T$$

$$= \pi r^2 \rho C_p \Sigma\, h\Delta T$$

therefore

$$(Q_I)_{T=1550} = \pi r^2 C_{ps}\rho\left[\sum_{y=0}^{15} y\Delta T - (15)(T_o)\right] \tag{7.4}$$

$$= 11962 \text{ kcals}$$

and

$$(Q_I)_{T=1650} = \pi r^2 C_{ps}\rho_s\left[\sum_{y=0}^{12} y\Delta T - (12)(T_o)\right] \tag{7.5}$$

$$= 9892 \text{ kcals}$$

There calculations, however, assume that the liquid slag system is an infinite heat source capable of maintaining T_b constant. Comparing these heat contents with the available heat content of the slag ($(Q_A)_s = 8 \times 10^3$ kcals), calculated in Appendix III.1.3 , clearly indicates

that the slag system is not an infinite heat source and that, in fact, the heat loss from the slag to the electrode is sufficient to completely freeze the slag. Therefore, in order to get the tip of the electrode to its melting point a very large power input into the system would be required, and the time to achieve this state would be considerably lengthened. Another probable consequence of the large thermal burden on the slag would be an increased rate of heat loss from the metal, across the slag/metal interface. This would result in the accelerated solidification of the metal pool producing irreversible structural and compositional changes. On the basis of these calculations, therefore, it is clear that unless the problems associated with the thermal burden of the electrode on the slag system are solved, the electrode change process holds very little potential for the production of large ingots.

7.3 Electrode Preheating

A possible solution suggested to alleviate the thermal burden problem is to preheat the electrode tip to within 200°C to 300°C of its melting point.[33] This would eliminate a large portion of the heat necessary to begin melting the electrode and reduce the time necessary to re-achieve steady-state conditions. In order to obtain an estimate as to the extent that preheating reduces the thermal burden on the liquid slag, several temperature profiles were calculated assuming that the electrode was being heated in a slag bath at 1200°C. Figure 64 shows the resulting profiles superimposed on the electrode profile for T_b equals 1550°C. On the basis of these profiles a preheating time of approximately 500 seconds at 1200°C provides the

best compromise between heat content in the tip region of the electrode and the thermal energy required to achieve it. Using this profile it was possible to calculate an approximate value for the heat input required to get the electrode tip to its melting point with a liquid slag temperature of 1550°C. This heat input Q_I was determined as follows:

$$Q_I = \pi r^2 C_{p_s} \rho_s \Sigma \; y\Delta T \qquad (7.4)$$

$$= 950 \text{ kcals}$$

where $\Sigma \; y\Delta T$ is the hatched area between the two profiles. This represents only 11.2 percent of the original available heat content of the liquid slag. Q_I could be still further reduced by preheating the electrode tip to within 100 to 200°C below its melting point and by maintaining the slag temperature at 1650°C with the use of auxilliary electrodes.

Using the conditions described in Figure 63 the time required to start melting with the preheated electrode would be approximately 60 sec. It has been shown (Section 5.2), however, that the heat supply to the metal pool is primarily from the molten droplets during the melting operation. Under these conditions, therefore, it would take approximately 120 seconds before the heat supply to the metal pool was re-established. It should be noted, however, that this represents a maximum time interval as the time required to change electrodes could be reduced from 60 seconds down to 20 to 30 seconds with more sophisticated equipment.

Assuming that it was 120 seconds before the new electrode began melt the maximum amount of liquid metal that would freeze would be 18.6 percent (Appendix VI). On the basis of the results from Section (3.2) this would result in minimal concentration banding particularly in alloys with low carbon, sulphur, and phosphorous concentrations.

The tandem electrode process, therefore, appears to be a feasible technique for producing large commercial ingots if preheated electrodes are used.

8. CONCLUSIONS

1. Power interruption experiments on AISI 4340 and EN-25 steels, produced only minor changes in the ingot structures. Significant compositional banding was observed for carbon but not for the other elements present. A possible model for the formation of the carbon concentration banding during the "power-on-off" sequence was proposed. Fluctuations in the slag skin thickness were found to produce carbon concentration bands at the edge of the ingot.

2. Power interruption experiments on AISI 630 (17-4PH) stainless steel produced significant structural changes due to the steels low crystal growth anisotropy. No changes in the concentration of Ni, Cr, and Cu were observed as a result of the "power-off" experiment in the ingots produced on the U.B.C. ESR unit. The nature of the banded structure found in some commercial ingots was identified as regions of high δ-ferrite content.

3. The most probable cause of the mixing action in the ESR metal pool is momentum and heat transfer from the falling metal droplets. The resulting mixing action is a slow convective motion which approaches a state of complete mixing at the slow solidification rates found in the ESR process. During a "power-off-on" situation, elements

with k_o value between 0.5 and 1.0 will have minimal concentration banding associated with them. Elements on the other hand, with k_o values lower than 0.5 could show significant concentration banding and macrosegregation.

4. The average superheat of the liquid metal pool for a 10 cm diameter ESR ingot was estimated to be 58°C. The outside limits of this superheat were found to be 47°C and 87°C. The average superheat of the liquid metal pool in a 61 cm diameter and 254 cm diameter ESR ingot were estimated to be 70°C and 80°C respectively. The average superheat of the liquid metal pool for a 10 cm diameter VAR ingot was estimated to be 121°C. This is much higher than that found in a similar sized ESR ingot and could account for the much deeper pool profiles observed in VAR ingots.

5. The rate of heat transfer at the liquid metal/slag skin, liquid slag/slag skin, and liquid slag/atmosphere interfaces were determined as a function of the "power-off" mode. They all decreased rapidly and showed an immediate response to the "power-off" condition. The rate of heat transfer across the liquid slag/liquid metal interface is critically dependent on the heat transfer coefficient across the interface due to the small temperature gradient. The net flow of heat across this interface for longer durations ($t > 15$ sec) of the "power-off" mode is approximately zero.

6. The liquid metal solidifies at an approximately uniform rate during the early stages of the "power-off" mode. The liquid slag solidifies rapidly at first insulating itself from its major sources of heat loss. This causes its solidification rate to decrease. The calculated values of the volume percents solidified based on a heat balance during the "power-off" mode were verified experimentally by tungsten powder additions. In a 61 cm diameter ESR ingot it was estimated that a maximum of 10 percent of the liquid metal and 10.3 percent of the liquid slag would solidify during a 60 second power interruption. The VAR process appears to be more sensitive than the ESR process to any disruptions in the systems power supply.

7. A general unsteady-state heat transfer program was written to calculate temperature profiles in an electrode that is immersed in a slag bath. Preheated electrodes must be used in the tandem electrode change machine if structural and compositional changes are to be avoided. The use of a preheated electrode and auxillary electrodes to maintain the slag temperature would ensure minimal structural and compositional changes in the ingot during an electrode change operation.

9. SUGGESTIONS FOR FUTURE WORK

1. Since it has been shown that the compositional irregularities are produced when the power was re-established, it would be a practical exercise to carry out a more detailed examination of this stage. By carefully controlling the power input into the system when re-establishing the equilibrium thermal conditions it may be possible to completely eliminate the formation of any compositional irregularities during the electrode change operation.

2. Although some information was obtained concerning the heat transfer across the slag/metal interface it would be of interest to carry out a more detailed examination of the heat transfer in this region. This would entail a determination of the heat transfer coefficient at this interface, as well as a better understanding of how the metal and slag temperatures change during the "power-off" mode. The results of this investigation would also provide some estimate as to the effectiveness of auxilliary electrodes in heating the slag and metal pools during the electrode change operation.

3. A series of power interruption experiments on a large commercial ingot could be used to check the validity of the many assumptions that had to be made in order to scale up the experimental results obtained on the lab-scale ESR unit.

APPENDIX I

DETERMINATION OF CONCENTRATION PROFILES

I.1 Determination of the normalized concentration of radioactive tin and sulphur

$$C_x = \frac{(C'_x - C_o)}{(C_i - C_o)} \qquad \text{(A.I-1.1)}$$

where:

C_o = the equilibrium concentration

C_i = the concentration at the interface

C'_x = the concentration at any point x from the interface

C_x = the relative fractional concentration at any point x from the interface.

I.2 Determination of the theoretical profile for k = 1 and complete mixing

To circumvent the pool shape problem the liquid pool was considered to be cylindrical. Because the geometry of the solidification front was assumed to be flat the volume of liquid metal solidified is proportional to the change in height (Δh).

$$\text{Volume solidified} \propto \frac{\Delta h}{h_o} \qquad \text{(A.I-2.1)}$$

where: h_o is the original height of the cylinder.

Since the liquid is assumed to be of uniform composition (C_L) and k

equal to unity, the concentration of the solid (C_S) is:

$$C_{S_1} = (C_L)_1 \frac{\Delta h}{h_o}$$

However, since the volume of liquid metal during ESR processing must remain constant a new volume of pure metal must be introduced which is equal to the volume solidified. Therefore the new composition of the liquid is

$$(C_L)_2 = (C_L - C_S)_1$$

When another equal increment of volume solidifies the concentration of the solid ($(C_S)_2$) is

$$(C_S)_2 = (C_L)_2 \frac{\Delta h}{h_o}$$

$$= (C_L - C_S)_1 \frac{\Delta h}{h_o}$$

A general form of this equation can be written as follows assuming $\frac{\Delta h}{h_o}$ is constant.

$$(C_S)_n = (C_L - C_S)^{n-1}_{n-1} \frac{\Delta h}{h_o} \qquad \text{(A.I-2.2)}$$

Using equation A.I-2.2 and assuming $C_L = 1$ and $\frac{\Delta h}{h_o} = 0.1$ a theoretical profile for solute dilution was calculated.

APPENDIX II

DETERMINATION OF THE VOLUME OF LIQUID METAL AND LIQUID SLAG WHICH SOLIDIFIES IN A 10 cm DIAMETER INGOT DURING A RANGE OF POWER INTERRUPTIONS

II.1 Heat content of the metal pool system and the slag pool system at the start of the "power-off" mode

II.1.1 Assumed Data

(a) the metal pool system:

(i) $T_{m.p.} = 1500°C$

(ii) $(C_P)_\ell = 0.18$ cal/g/°C

(iii) $L = 65.5$ cal/g

(iv) $\rho_{Avg} = 7.5$ g/cm^3

(v) $\rho_\ell = 7.0$ g/cm^3

(vi) $\Delta T_S = 58°C$

(b) the slag pool system:

(i) $T_{m.p.} = 1450°C$[29]

(ii) $T_{Avg} = 1660°C$[30]

(iii) $(C_p)_\ell = 0.3$ cal/g/°C

(iv) $L = 46.6$ cal/g

(v) $\rho_{Avg} = 2.6$ g/cm^3

II.1.2 Available heat content of the metal pool system.

Figure 53-B shows a schematic diagram of the metal pool system. The total heat content ($(Q_T)_M$) was calculated as follows:

$$(Q_T)_M = \Sigma \; mC_p\Delta T + mL$$

$$= V\rho_A C_p \Delta T + V\rho_\rho C_p \Delta T_S + V\rho_A L \qquad \text{(A.II-1.1)}$$

$$= 284 \text{ kcals} + 10 \text{ kcals} + 69 \text{ kcals}$$

$$= 363 \text{ kcals}$$

The available heat content of the metal pool system ($(Q_A)_M$) is the sum of the latent heat and superheat terms in equation A.II-1.1). This implies that the solid metal retains its sensible heat until the metal pool has completely solidified.

$$(Q_A)_M = V\rho_L C_p \Delta T_S + V\rho_A L \qquad \text{(A.II-1.2)}$$

$$= 79 \text{ kcals}$$

II.1.3 Available heat content of the slag pool system:

Figure 53-A shows a schematic diagram of the slag pool system. The total heat content ($(Q_T)_S$) was calculated as follows:

$$(Q_T)_S = \Sigma \; mC_p\Delta T + mL$$

$$= V\rho_L C_p \Delta T + V\rho_L C_p \Delta T_S + V\rho_L L \qquad \text{(A.II-1.3)}$$

$$= 402 \text{ kcals} + 54 \text{ kcals} + 44 \text{ kcals}$$

$$= 500 \text{ kcals}$$

The available heat content of the slag pool system ($(Q_A)_S$) is the sum of the latent heat and superheat terms in equation A.II-1.3. This implies that the solidified slag retains its sensible heat until the slag pool has completely solidified.

$$(Q_A)_S = V\rho_L C_p \Delta T_S + V\rho_L L \qquad \text{(A.II-1.4)}$$

$$= 98 \text{ kcals}$$

II.2 Rate of heat loss from the slag and metal pool systems.

For the purpose of this calculation it was assumed that the rate of heat loss ($\dot{q}$) from any part of the system was directly proportional to its surface area. It was also assumed that the heat transfer across the slag/metal interface ($\dot{q}_6$) was negligible.

II.2.1 Heat loss from the metal pool system for different durations of the "power-off" mode

Figure 53-B shows the main regions of heat loss from the liquid metal pool.

II.2.1.1 Heat loss across the liquid metal/slag skin interface (q_1)

Using Figure 50 and an area correction factor (K_A) the heat loss from this region for any time (t) was calculated as follows:

$$q = K_A \sum_{t=1}^{t} \dot{q}_t \qquad \text{(A.II-2.1)}$$

where $K_A = \frac{(4.7)(1.5)}{(4.45)(1.5)} = 1.06$

(a) $t = 2.5$ seconds

$$q = 1.06\ \Sigma(0.63 + 0.60 + 0.27)\text{kcals}$$

$$= 1.6\ \text{kcals}$$

(b) $t = 5$ seconds

$$q = 1.06\ [\sum_{t=1}^{2} + \Sigma(0.53 + 0.48 + 0.43)]\text{kcals}$$

$$= 2.8\ \text{kcals}$$

(c) $t = 7.5$ seconds

$$q = 1.06[\sum_{t=1}^{5} + \Sigma(0.38 + 0.33 + 0.15)]\text{kcals}$$

$$= 3.6\ \text{kcals}$$

(d) $t = 10$ seconds

$$q = 1.06[\sum_{t=1}^{7} + \Sigma(0.29 + 0.26 + 0.23)]\text{kcals}$$

$$= 4.4\ \text{kcals}$$

(e) $t = 12.5$ seconds

$$q = 1.06[\sum_{t=1}^{10} + \Sigma(0.20 + 0.18 + 0.08)]\text{kcals}$$

$$= 4.9\ \text{kcals}$$

(f) $t = 15$ seconds

$$q = 1.06[\sum_{t=1}^{10} + \Sigma(0.20 + 0.18 + 0.16 + 0.14 + 0.12)]\text{kcals}$$

$$= 5.5\ \text{kcals}$$

(g) $t = 20$ seconds

$$q = 1.06 \sum_{t=1}^{15} + 1.06(5)(0.1)$$

$$= 6.1 \text{ kcals}$$

(h) $t = 30$ seconds

$$q = 6.1 \text{ kcal} + 1.06(10)(0.1)$$

$$= 6.3 \text{ kcals}$$

II.2.1.2 Heat loss by conduction down the solidified ingot (q_2)

Using the rate of heat loss down a 7.6 cm diameter ingot determined by Joshi[31] ($\dot{q} = 0.3$ kcals/sec) and the area correction factor (K_A), the heat loss across this interface for any time (t) was calculated.

$$q = K_A \dot{q} t \qquad \text{(A.II-2.2)}$$

where $$K_A = \frac{(10)^2}{(7.6)^2} = 1.7$$

(a) $t = 2.5$ seconds

$q = 1.3$ kcals

(b) $t = 5$ seconds

$q = 2.5$ kcals

(c) $t = 7.5$ seconds

$q = 3.8$ kcals

(d) t = 10 seconds

q = 5.0 kcals

(e) t = 12.5 seconds

q = 6.0 kcals

(f) t = 15 seconds

q = 7.5 kcals

(g) t = 20 seconds

q = 10.0 kcals

(h) t = 30 seconds

q = 15.0 kcals

II.2.1.3 Heat loss across the solid metal/slag skin interface

Using the minimum rate of heat loss for conduction from the metal in figure (q = 0.1 kcal/sec) and the area correction factor (K_A), the heat loss across this interface at any time (t) was calculated.

$$q = K_A q t \qquad \text{(A.II-2.3)}$$

where $K_A = \frac{(10)L}{(7.6)L} = 1.3$

(a) t = 2.5 seconds

q = 0.3 kcals

(b) t = 5 seconds

q = 0.6 kcals

(c) t = 7.5 seconds

q = 1.0 kcals

(d) t = 10 seconds

q = 1.3 kcals

(e) t = 12.5 seconds

q = 1.6 kcals

(f) t = 15 seconds

q = 1.9 kcals

(g) t = 20 seconds

q = 2.7 kcals

(h) t = 30 seconds

q = 3.8 kcals

II.2.2 Heat loss from the slag pool system for different durations of the "power-off" mode

Figure 53-A shows the main regions of heat loss from the liquid slag pool.

II.2.2.1 Heat loss across the slag-air interface (q_4)

Using Figure 50 and an area correction factor (K_A) the heat loss across this interface for any time (t) was calculated as follows:

$$q = K_A \sum_{t=1}^{t} \dot{q}_t \qquad \text{(A.II-2.4)}$$

where $K_A = \frac{(4.8)^2}{(4.45)^2} = 1.16$

(a) t = 2 seconds

$q = 1.16\ \Sigma(0.47 + 0.41)$

$= 1.0$

(b) t = 5 seconds

$q = 1.16\ \Sigma(0.47 + 0.41 + 0.35 + 0.34 + 0.28)$kcals

$= 2.2$ kcals

(c) t = 10 seconds

$q = 1.16[\sum_{t=1}^{5} + \Sigma(0.25 + 0.23 + 0.21 + 0.20 + 0.19)]$kcals

$= 3.4$ kcals

(d) $t = 15$ seconds

$$q = 1.16[\sum_{t=1}^{10} + \Sigma(0.18 + 0.17 + 0.16 + 0.15 + 0.14)]\text{kcals}$$

$$= 4.3 \text{ kcals}$$

(e) $t = 30$ seconds

$$q = 1.16[\sum_{t=1}^{15} + \Sigma(0.13 + 0.12 + 0.12 + 0.11 + 0.10 + 0.10 + 0.09 + 0.08 + 0.07 + 2(0.06) + 4(0.05))]\text{kcals}$$

$$= 5.8 \text{ kcals}$$

II.2.2.2 Heat loss across the liquid slag-slag skin interface (q_5)

Using Figure 50 and an area correction factor (K_A) the heat loss across this interface for any time (t) was calculated as follows:

$$q = K_A \sum_{t=1}^{t} \dot{q}_t \qquad \text{(A.II-2.5)}$$

where $A = \frac{(4.8)(5.0)}{(4.45)(4.5)} = 1.2$

(a) $t = 2$ seconds

$$q = 1.2 \ \Sigma(1.89 + 1.75)\text{kcals}$$

$$= 4.2 \text{ kcals}$$

(b) $t = 5$ seconds

$$q = 1.2 \ \Sigma(1.89 + 1.75 + 1.60 + 1.45 + 1.30)\text{kcals}$$

$$= 9.6 \text{ kcals}$$

(c) $t = 10$ seconds

$$q = 1.2\left[\sum_{t=1}^{5} + \Sigma(1.25 + 1.0 + 0.85 + 0.7 + 0.52)\right]\text{kcals}$$

$$= 14.3 \text{ kcals}$$

(d) $t = 15$ seconds

$$q = 1.2\left[\sum_{t=1}^{10} + \Sigma(0.4 + 0.33 + 0.28 + 0.23 + 0.20)\right]\text{kcals}$$

$$= 16.0 \text{ kcals}$$

(e) $t = 30$ seconds

$$q = 1.2\left[\sum_{t=1}^{15} + \Sigma(0.17 + 0.14 + 0.12 + 0.11 + 0.09 + 0.08 + 0.07 + 0.06 + 7(0.05))\right]\text{kcals}$$

$$= 17.5 \text{ kcals}$$

APPENDIX III

DETERMINATION OF THE VOLUME OF LIQUID METAL AND LIQUID SLAG THAT SOLIDIFIES IN A 61.0 cm DIAMETER INGOT DURING 60 SECONDS OF "POWER-OFF" OPERATION

III.1 The available heat content of the metal and slag pool systems at the start of the "power-off" mode

III.1.1 Assumed data

(a) the metal pool system

(i) $T_{m.p.} = 1500°C$

(ii) $(C_p)_{\ell} = 0.18$ cal/g/°C

(iii) $L = 65.5$ cal/g

(iv) $\rho_{Avg} = 7.5$ g/cm^3

(v) $\rho_{\ell} = 7.0$ g/cm^3

(vi) $\Delta T_S = 70°C$

(b) the slag pool system (CaF_2 + 25 wt.% Al_2O_3)

(i) $T_{m.p.} = 1450°C$

(ii) $(C_p)_{\ell} = 0.3$ cal/g/°C

(iii) $L = 46.6$ cal/g

(iv) $\rho_{Avg} = 2.6$ g/cm^3

(v) $\Delta T_S = 210°C$

III.1.2 The available heat content of the metal pool system

The total heat content of the system ($(Q_T)_M$) was calculated as follows:

$$(Q_T)_M = \Sigma m C_p \Delta T + mL$$

$$= V\rho_A C_p \Delta T + V\rho_L C_p \Delta T_S + V\rho_L L \qquad \text{(A.III-1.1)}$$

$$= (58.1 \times 10^3 + 2.6 \times 10^3 + 14.3 \times 10^3)\text{kcals}$$

$$= 75 \times 10^3 \text{ kcals}$$

The total available heat content $(Q_A)_M$ is assumed to be the sum of the latent heat and superheat terms in equation (A.III-1.1).

$$(Q_A)_M = V\rho C_p \Delta T_S + V\rho_A L \qquad \text{(A.III-1.2)}$$

$$= 17 \times 10^3 \text{ kcals}$$

III.1.3 The available heat content of the slag pool system

The total heat content $((Q_T)_S)$ was calculated as follows:

$$(Q_T)_S = \Sigma m C_p \Delta T_S + mL \qquad \text{(A.III-1.3)}$$

$$= V\rho_A C_p \Delta T + V\rho_A C_p \Delta T_S + V\rho_A L$$

$$= (33.6 \times 10^3 + 4.8 \times 10^3 + 3.5 \times 10^3)\text{kcals}$$

$$= 42 \times 10^3 \text{ kcals}$$

The total available heat content $(Q_A)_S$ is assumed to be the sum of the latent heat and superheat terms in equation A.III-1.3.

$$(Q_A)_S = V\rho_A C_p \Delta T_S + V\rho_A L \qquad \text{(A.III-1.4)}$$

$$= 8 \times 10^3 \text{ kcals}$$

III.2 Rate of the heat loss from the slag pool and metal pool systems during the "power-off" mode

For the purpose of this calculation it was assumed that the rate of heat loss ($\dot{q}$) from any part of the system was directly proportional to the surface areas involved. This assumption made it possible to use the heat transfer profiles experimentally determined for the 7.6 cm diameter ingots. It was also assumed for simplicity that the net heat flow across the slag/metal interface (q_6) was zero.

III.2.1 Heat loss from the metal pool system during the 60 seconds of "power-off" operation

III.2.1.1 Heat loss from the metal pool across the liquid metal/slag skin interface (q_1) in 60 seconds

Using Figure 50 and an area correction factor (K_A) the heat loss across this boundary for any time (t) was calculated as follows:

$$q = K_A \sum_{t=1}^{t} \dot{q}_t \qquad \text{(A.III-2.1)}$$

where $K_A = \dfrac{r_1 \ell_1}{r_2 \ell_2} = \dfrac{(30.5)(10.0)}{(4.45)(1.5)} = 45.7$

It was also assumed that the minimum value for the rate of heat loss across this interface was 0.1 kcals/sec. Therefore the heat loss in 60 seconds was

$$q_1 = 45.7 \sum_{t=1}^{60} q_t$$

$$= 490 \text{ kcals}$$

III.2.1.2 Heat loss from the metal pool across the liquid metal/solid metal interface (q_2)

The rate of heat loss across this interface for the 7.56 cm diameter ingots was approximately 0.3 kcals/sec, therefore:

$$q_2 = K_A(0.3)t \text{ kcals} \qquad \text{(A.III-2.2)}$$

where $K_A = \frac{(r_1)^2}{(r_2)^2} = \frac{(30.5)^2}{(3.78)^2} = 65$

hence $q_2 = (65)(0.3)(60)$

$= 1172$ kcals

It should be noted, however, that this represents the maximum heat flow possible in this direction. Because the heat loss down the ingot is inversely proportional to the ingot height this value would only be applicable near the bottom of the ingot and would decrease with the ingot height. The actual value, therefore, could be between 30 to 50 percent smaller than the calculated value.

III.2.1.3 Heat loss from the metal pool across the solid metal/slag skin interface

The rate of heat loss across this interface for the 7.6 cm diameter ingots was approximately 0.1 kcals/sec, therefore:

$$q_3 = K_A(0.1)t \text{ kcals} \qquad \text{(A.III-2.3)}$$

where $K_A = \frac{61.0L}{7.8L} = 7.8$

hence $q_3 = (7.8)(0.1)(60)$

$= 47$ kcals

III.2.1.4 The total heat loss $(q_L)_M$ from the metal pool during the 60 seconds of "power-off" operation

$$(q_L)_M = q_1 + q_2 + q_3 \qquad \text{(A.III-2.4)}$$

$= (490 + 1172 + 47)$kcals

$= 1709$ kcals

This represents a maximum value for the amount of heat lost from the metal pool in 60 seconds.

III.2.2 Heat loss from the slag pool system during the 60 seconds of "power-off" operation

III.2.2.1 Heat loss across the slag/air interface (q_4)

Using Figure 50 and the area correction factor (K_A) the heat loss across this interface at any time (t) was calculated as follows:

$$q_4 = K_A \sum_{t=1}^{t} q_t \qquad \text{(A.III-2.5)}$$

where $K_A = \frac{(30.5)^2}{(4.45)^2} = 47$

therefore $q_4 = (47)(8.4)$ kcals

$= 394$ kcals

III.2.2.2 Heat loss across the liquid slag/slag skin interface (q_5)

Using Figure 50 and the area correction factor K_A the heat loss across this interface for any time (t) was calculated as follows:

$$q_5 = K_A \sum_{t=1}^{t} q_t \qquad \text{(A.III-2.6)}$$

where $K_A = \frac{(30.5)(10)}{(4.45)(5)} = 13.8$

therefore $q_5 = (13.8)(27.8)$ kcals

$= 384$ kcals

III.2.2.3 The total heat loss $(q_L)_S$ from the liquid slag during the 60 seconds of "power-off" operation

$$(q_L)_S = q_4 + q_5 \qquad \text{(A.III-2.7)}$$

$= (394 + 384)$ kcals

$= 778$ kcals

This represents a maximum value for the amount of heat lost from the slag pool in 60 seconds.

III.3 Volume of liquid metal and liquid slag to freeze during the 60 second "power-off" mode

III.3.1 The percentage of the liquid metal pool that would solidify in 60 seconds under the assumed conditions

The total available heat content (1.2)

$$(q_A)_M = 17 \times 10^3 \text{ kcals}$$

The total heat loss in 60 seconds (2.1.4)

$$(q_L)_M = 1709 \text{ kcals}$$

Therefore the percentage of the metal pool that would be solidified in 60 seconds

$$\text{Volume percent solidified} = \frac{(q_L)_M}{(q_A)_M} \times 100 = 10\% \qquad \text{(A.III-3.1)}$$

III.3.2 The percentage by volume of the liquid slag that would solidify in 60 seconds under the assumed conditions

The total available heat content (1.3)

$$(q_A)_S = 8 \times 10^3 \text{ kcals}$$

The total heat loss in 60 seconds (2.2.3)

$$(q_L)_S = 778 \text{ kcals}$$

Therefore the percentage of the slag pool that would be solidified in 60 seconds

$$\text{Volume percent solidified} = \frac{(q_L)_S}{(Q_A)_S} \times 100 = 10.3\% \qquad \text{(A.III-3.2)}$$

APPENDIX IV

HEAT BALANCE FOR A 10 cm DIAMETER VAR INGOT DURING A 12.5 SECOND POWER INTERRUPTION

IV.1 Determination of the heat content of the system

IV.1.1 Thermal data

(a) Melting point = 1500°C

(b) C_p = 0.18 cal/g/°C

(c) L = 65.5 cal g^{-1}

(d) ρ_{Avg} = 7.5 g cm^{-3}

(e) ρ_L = 7.0 g cm^{-3}

(f) ΔT_S = 120°C

IV.1.2 Total heat content of the metal pool system (Q_T)

$$Q_T = V\rho_A C_p \Delta T + V\rho_\rho C_p \Delta T_S + V\rho_A L \qquad \text{(A.IV-1.1)}$$

$$= 936 \text{ kcal} + 71 \text{ kcals} + 231 \text{ kcals}$$

$$= 1238 \text{ kcals}$$

IV.1.3 Total available heat content of the metal pool system (Q_A)

$$Q_A = V\rho_\rho C_p \Delta T_S + V\rho_A L \qquad \text{(A.IV-1.2)}$$

$$= 302 \text{ kcals}$$

This value assumes that the metal pool retains its sensible heat until both the superheat and the latent heat are removed.

IV.2 Determination of the heat loss from the pool in 12.5 seconds

There are three main sources of heat loss in the VAR system: 1) radiation from the surface of the metal, 2) conduction through the sides of the ingot, and 3) conduction down the ingot.

IV.2.1 Heat loss by radiation from the surface of the liquid metal (q_1)

(a) Assumed data

(i) The average temperature of the metal at the surface was 1650°C.

(ii) The electrode was removed.

(iii) The shape factor (S) for the system was 1.0.

(iv) The emisivity (ε) for the metal was 0.37.

(b) The amount of heat loss from the metal due to radiation in 12.5 seconds was:

$$q_1 = SA\varepsilon\sigma[T_1^4 - T_2^4]t \qquad \text{(A.IV-2.1)}$$

$$= 6.72 \text{ kcals}$$

IV.2.2 Heat loss through the sides of the ingot

In order to obtain some estimate of the rate of heat flow through the sides of the ingot it was necessary to have a profile which showed the change in the heat flux with distance below the top of the ingot. In a paper published by the Bureau of Mines several profiles are

given for steel electrodes melted at different rates of power input (Figure 60). It was assumed that the power input was proportional to the cross-sectional area of the ingot so that the 10 cm diameter ingot could be scaled up to fit the profiles.

The power input into ingot no. V-3 was calculated on the basis of its operating conditions.

$$\text{i.e. power input (KW)} = (\text{volts})(\text{amps}) \qquad \text{A.IV-2.2)}$$

$$= (25)(2900)$$

$$= 72.5 \text{ KW}$$

This corresponds to a power input of approximately 300 kilowatts for a 20.32 cm diameter ingot. Although this is a higher power input than run no. 9 in Figure 60, the profile still provides a good approximation of the rate of heat transfer during steady-state conditions. Because the rate of heat transfer will decrease during the "power-off" mode this profile will provide a maximum value for the radial heat loss during the "power-off" mode. Figure 61 shows the heat flux profile for run no. 9 in metric units.

(a) Assumed data

(1) The heat conduction above the ingot top during the "power-off" condition was assumed to be negligible. This was reasonable since the high flux values in this area represented arc instabilities, and hot metal splashing on the crucible walls, and therefore, would not occur during the "power-off" mode.

(2) The radial heat flux lower than 12 cm below the ingot surface was considered negligible.

(b) Calculation of the radial heat loss from the ingot (q_2)

$$q_2 = A\left(\sum_{n=1}^{12} h\Delta T\right)t \qquad \text{(A.IV-2.3)}$$

where the average flux ($h\Delta T$) is determined at 1 cm intervals. Therefore,

$$q_2 = \pi(10)(1)(0.214)(12.5) \text{ kcals}$$

$$= 84 \text{ kcals}$$

IV.2.3 Heat loss by conduction down the ingot (q_3)

(a) Assumed data:

(1) The rate of heat loss was proportional to the rate for a similar sized ESR machine.

(2) The rate of heat loss was proportional to the surface area.

Using the rate of heat loss down a 7.6 cm diameter ESR ingot as determined by Joshi (q = 0.3 kcal/sec) and the area correction factor (K_A), the heat loss down the ingot was determined.

$$q_3 = K_A(0.3)(12.5) \text{ kcals} \qquad \text{(A.IV-2.4)}$$

where $K_A = \frac{(10)^2}{(7.6)^2} = 1.7$

Therefore

$$q_3 = 6.4 \text{ kcals.}$$

IV.2.4 Total heat loss from the liquid pool in 12.5 seconds (Q_L)

$$Q_L = q_1 + q_2 + q_3 \qquad \text{(A.IV-2.5}$$

$$= (6.7 + 84.0 + 6.4) \text{ kcals}$$

$$= 97.1 \text{ kcals}$$

This represents the maximum heat loss from the system during the 12.5 second power interruption.

IV.3 Percentage of the metal pool that solidified in 12.5 seconds of "power-off" operation

$$\text{Volume percent solidified} = \frac{Q_L}{Q_A} \times 100 \qquad \text{(A.IV-3.1)}$$

$$= 32.2\% \text{ solidified}$$

APPENDIX V. COMPUTER PROGRAM TO DETERMINE THE UNSTEADY-STATE TEMPERATURE PROFILE IN AN ESR ELECTRODE.

```
FORTRAN IV G COMPILER        MAIN          12-13-71        10:43:33        PAGE 0001

0001                ALPHA = .057
0002                HP = .564
0003                H = .04
0004                TP=130.
0005                TIME = TP
0006                TP=5.
0007                TU = 25.
0008                TB=1650.
0009                TF = TB-TU
0010                DO 2 N=1,14
0011                WRITE (6,9)
0012                Y = .1
0013                B = SQRT(ALPHA*TIME)
0014                DO 1 M=1,35
0015                C = Y/(2.*B)
0016                TEMP =TF*((1.-ERF(C))-EXP(-HP*(Y+HP*ALPHA*TIME))*(1.-ERF(C+H*B)))
0017                TEMP = TEMP + TU
0018                WRITE (6,10) TIME,Y,TEMP
0019                IF(Y.GE.15.) Y=Y+5.
0020                IF (Y.LT.15..AND.Y.GE.1.) Y=Y+1.
0021                IF(Y.LT.1.) Y=Y+.1
0022          1     CONTINUE
0023                WRITE (6,11)
0024           2    TIME = TIME + TP
0025           9    FORMAT (8X'TIME',12X,'DISTANCE',7X,'TEMP'/)
0026           10   FORMAT (1X,3(1PE15.7,5X))
0027           11   FORMAT (1H1)
0028                STOP
0029                END
```

APPENDIX VI

DETERMINATION OF THE VOLUME OF LIQUID METAL THAT SOLIDIFIES IN A 61.0 cm DIAMETER INGOT DURING 120 SECONDS OF "POWER-OFF" OPERATION

VI.1 Available heat content of the metal pool system at the start of the "power-off" mode

From Appendix III.1.2.

$$(Q_A)_M = 17 \times 10^3 \text{ kcals}$$

VI.2 Rate of heat loss from the metal pool system during the "power-off" mode

This calculation contains the same assumptions found in Appendix III.2.

VI.2.1 Heat loss from the metal pool across the liquid metal/slag skin interface in 120 seconds

Using Figure 50 and an area correction factor (K_A) the heat loss across this boundary was calculated as follows:

$$q = K_A \sum_{t=0}^{t} q_t$$

where $K_A = \frac{r_1 \ell_1}{r_2 \ell_2} = 45.7$

Therefore the heat loss in 120 seconds was

$$q_1 = \sum_{t=1}^{60} q_t + \sum_{t=60}^{120} q_t \qquad \text{(A.VI-2.1)}$$

$$= 490 \text{ kcals} + (45.7)(0.1)(60)$$

$$= 764 \text{ kcals}$$

VI.2.2 Heat loss from the metal pool across the liquid metal/solid metal interface

The rate of heat loss across this interface for the 7.56 cm diameter ingots was approximately 0.3 kcals/sec, therefore,

$$q_2 = K_A(0.3)t \qquad \text{(A.VI-2.2)}$$

where $K_A = \dfrac{(r_1)^2}{(r_2)^2} = 65$

hence $q_2 = 2344$ kcals

VI.2.3 Heat loss from the metal pool across the solid metal/slag skin interface

The rate of heat loss across this interface for the 7.6 cm diameter ingot was approximately 0.1 kcals/sec, therefore,

$$q_3 = K_A(0.1)t \qquad \text{(A.VI-2.3)}$$

where $K_A = \dfrac{r_1 \ell_1}{r_2 \ell_2} = 7.8$

hence $q_3 = 94$ kcals

VI.2.4 Total heat loss $(Q_L)_M$ from the metal pool during the 120 seconds of "power-off" operation

$$(Q_L)_M = (764 + 2344 + 94) \text{ kcals} = 3202 \text{ kcals} \quad \text{(A.VI-2.4)}$$

VI.3 The percentage of the metal pool that would solidify in 120 seconds of "power-off" operation

The total available heat content (7.1.1)

$$Q_A = 17 \times 10^3 \text{ kcals}$$

The total heat loss in 120 seconds (7.1.4)

$$Q_L = 3202 \text{ kcal}$$

Therefore

$$\text{Volume percent solidified} = \frac{Q_L}{Q_A} \times 100 = 18.8\% \quad \text{(A.VI-3.1)}$$

It should be noted that this represents the maximum amount of liquid metal that would solidify in this time period.

REFERENCES

1. Chalmers B., "Principles of Solidification", John Wiley (1964).

2. Chalmers B., and King R., (Editors), Pergamon Press (1959), 8, 203.

3. Turkdogan E.T., and Grange R.A., J.I.S.I. (1970), 208, 482.

4. Jatczak C.F., Giradi D.J., and Rowland E.S., Trans. A.S.M. (1956) 48, 279.

5. Weinberg F., and Buhr R.K., "The Solidification of Metals", Iron and Steel Inst., (1967) 295.

6. Thresh H., Bergeron M., Weinberg F., and Buhr R.K., Trans A.I.M.E. (1968), 48, 279.

7. Flemings M.C., Poirier D.R., Barone R.V., and Brody H.D., J.I.S.I. (1970) 208, 371.

8. Kattamis T.S., and Flemings M.C., Trans A.I.M.E. (1956) 233, 992.

9. Morton S.K., M.A.Sc. Thesis, University of British Columbia (1971).

10. Fredriksson H., and Jarleborg O., J. Metals (1971) 23,(9), 32.

11. Takada H., Fukuhara Y., and Miura M., internal report, Kobe Steel Ltd., Japan.

12. De Vries R.P., and Mumau G.R., J. Metals (1968), 20, (11), 33.

13. Firganek H., Jezierski K., and Siewierski J., Pace Inst. Huts, (1969) 21 (3), 141.

14. Etienne M., Ph.D. Thesis, University of British Columbia, (1970).

15. Buhr R.K., and Weinberg F., J.I.S.I. (1967) 205, 1161.

16. Kehl G.L., "The Principles of Metallographic Laboratory Practice", McGraw-Hill (1949), 186.

17. Lillie W.D., and Ward F.R. (Editors), "Radioisotope Applications Engineering,"D. Van Nostrand Co., Inc. (1961).

18. Microprobe Analysis General Intensity Correction, Fortran Program adapted by O'Brien T.E., Department of Metallurgy, U.B.C.

19. Hansen M., and Anderko K., "Constitution of Binary Alloys", McGraw-Hill (1958) 705.

20. Rein D.M., Armco Steel Corporation, private communication (1971).

21. Campbell J., J. Metals (1970) 22 (7) 23.

22. Hansen M., and Anderko K., op cit, 718-719.

23. Mitchell A., and Joshi S., University of British Columbia, private communication (1971).

24. Beall R.A., Bureau of Mines, Albany Oregon, private communication (1971).

25. Joshi S., Ph.D. Thesis, University of British Columbia (1971).

26. Maulvault A., and Elliot J.F., Electric Furnace Proceedings (1970) 28, 13.

27. Mendrykowski J., Poveromo J.J., Szekely J., and Mitchell A., Met. Trans., to be published.

28. Clites P.G., and Beall R.A., (Washington) U.S. Dept. of the Interior, Bureau of Mines (1967), R.I. 7035.

29. Burel B.C., M.A.Sc. Thesis, University of British Columbia (1969) 33.

30. Joshi S.J., op. Cit., 13.

31. Joshi S.J., University of British Columbia, private communication (1971).

32. Szekely and Themelis, "Rate Phenomena in Process Metallurgy", Wiley, (1971), 188.

33. Swoboda K., and Kleinhagauer O, German Pat., 1,903,843, 10 December (1970).

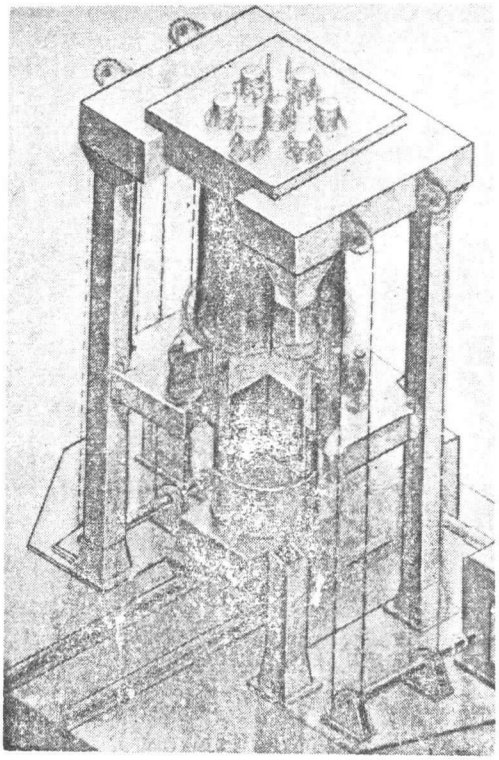

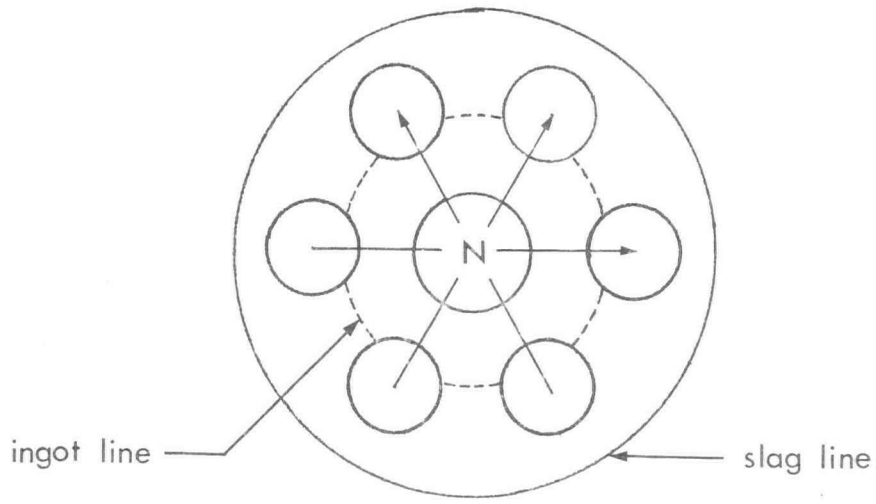

Figure 1. Three phase, seven electrode, bifilar furnace.

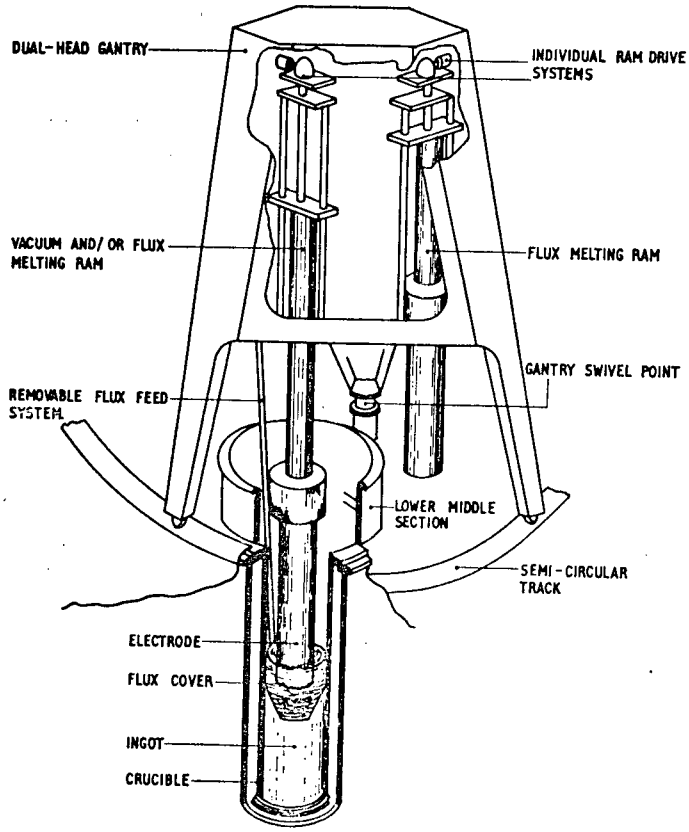

Figure 2. Tandem electrode change machine.

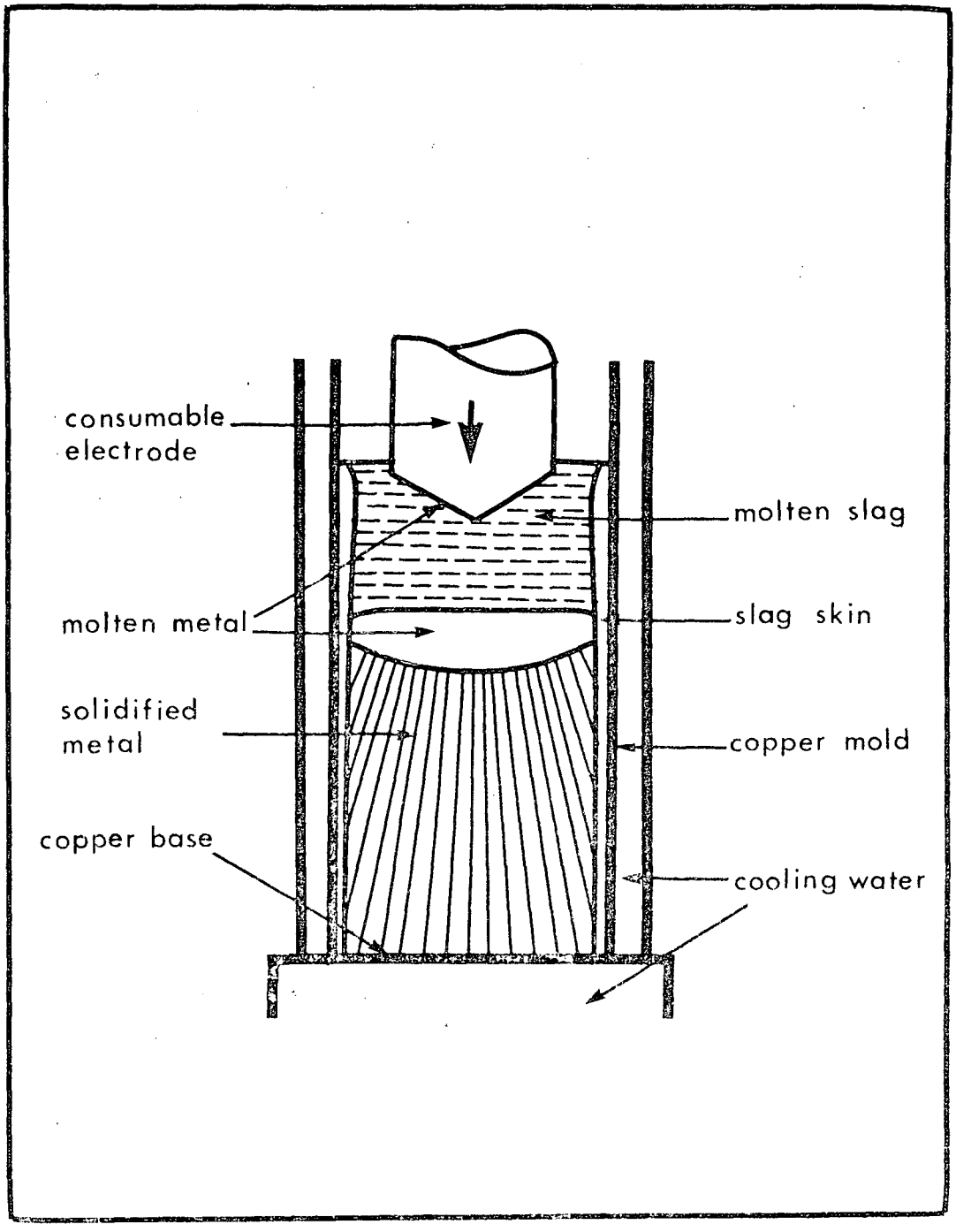

Figure 3. Schematic diagram of the U.B.C., ESR unit.

Consumable electrode vacuum arc melting furnace of Lectromelt design.

A—cooling water
B—control console
C—busbars
D—rectifiers
E—crane
F—furnace head
G—ram
H—vacuum pumps
J—middle section
K—gas to atmosphere
L—water jacket
M—crucible
N—electrode
O—ingot

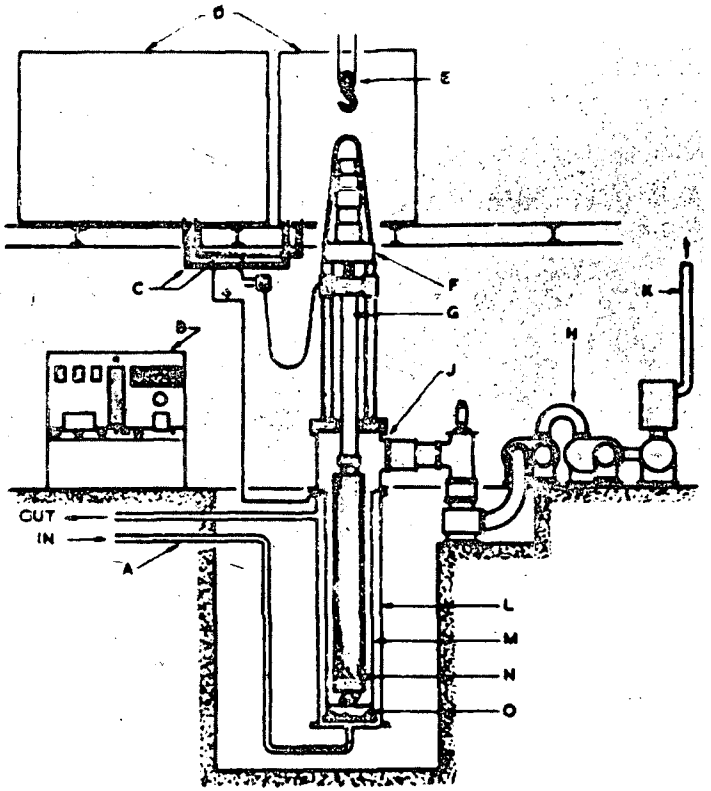

Figure 4. Schematic diagram of a VAR furnace.

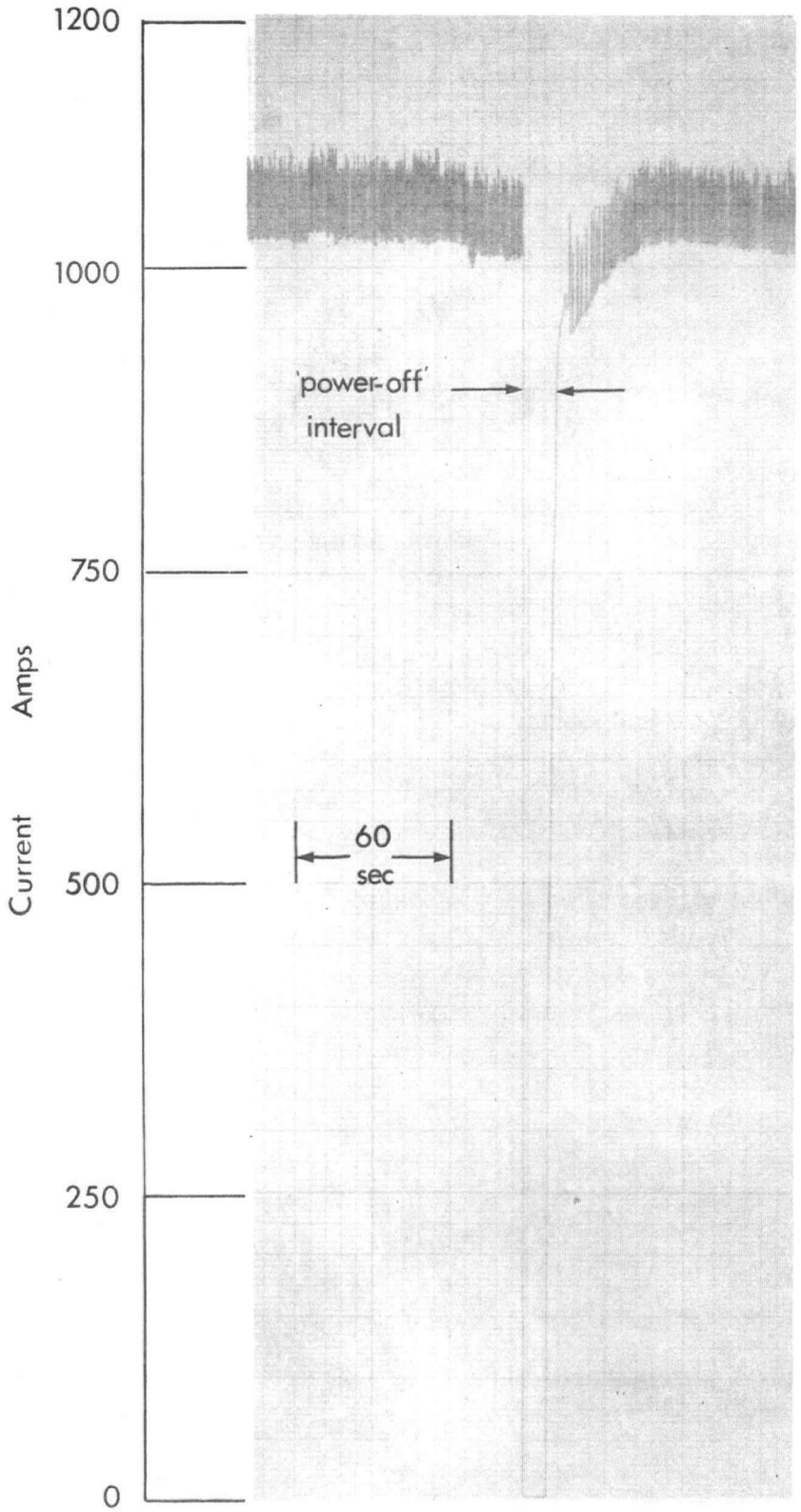

Figure 5. Operating chart during a "power-off" sequence.

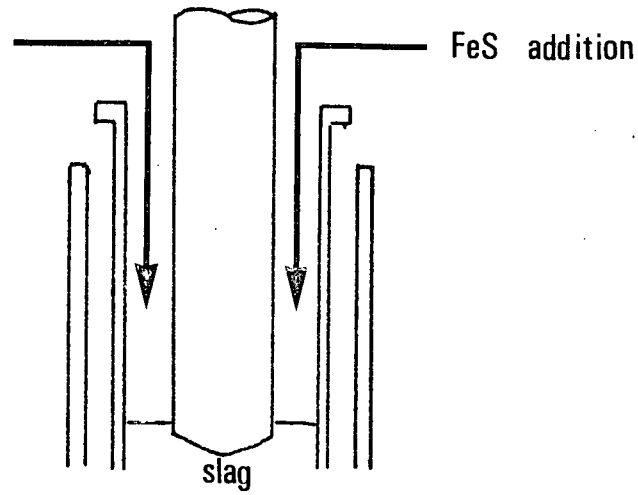

Figure 6. External addition of FeS to the melt.

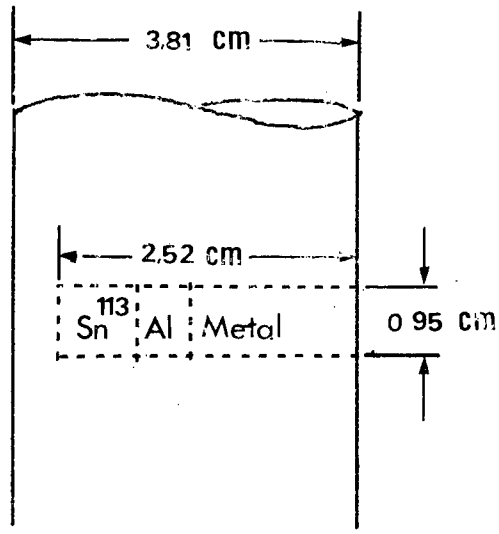

Figure 7. Configuration of the Sn^{113} in the electrode.

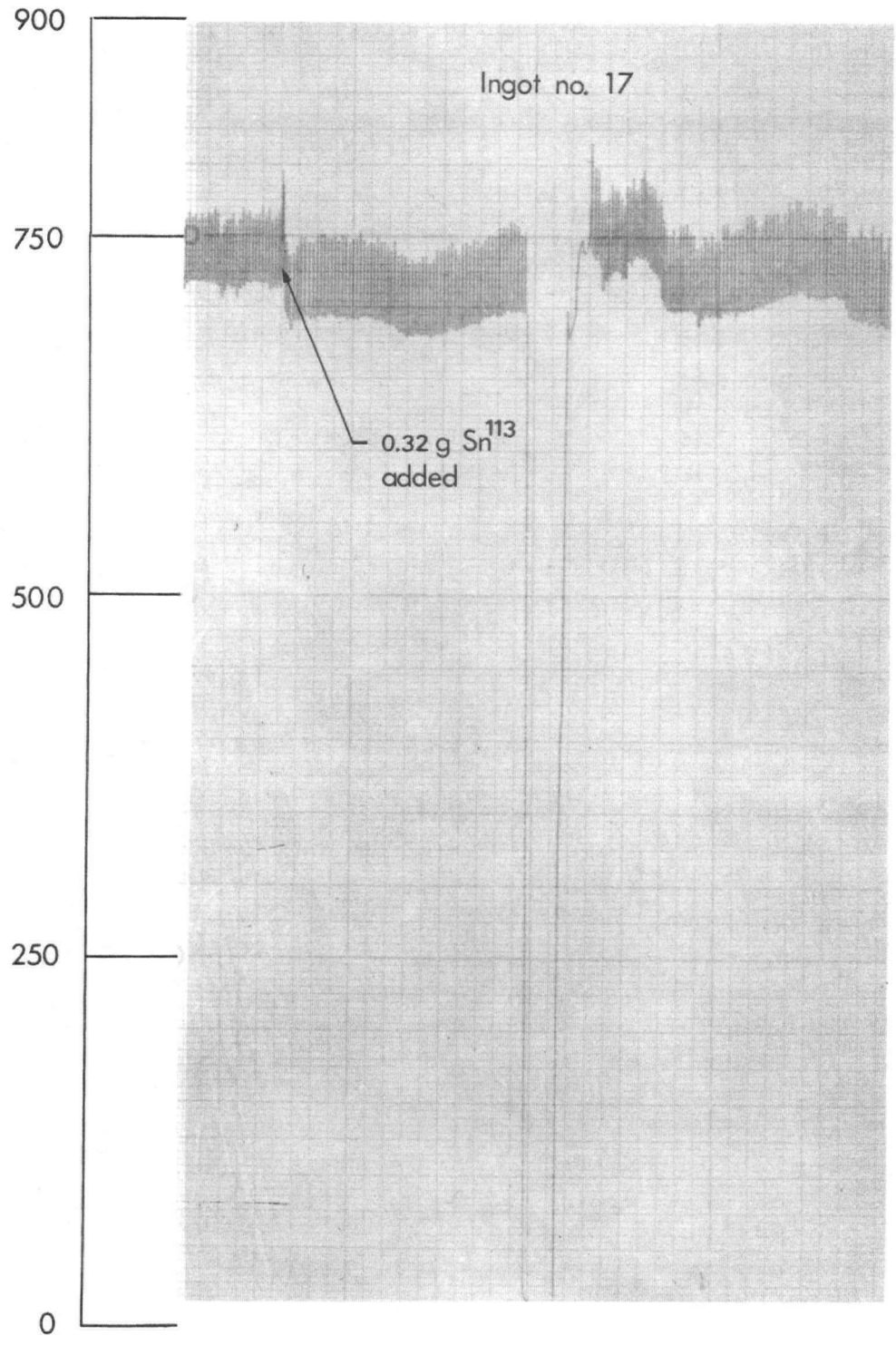

Figure 8. Operating chart during a Sn^{113} experiment.

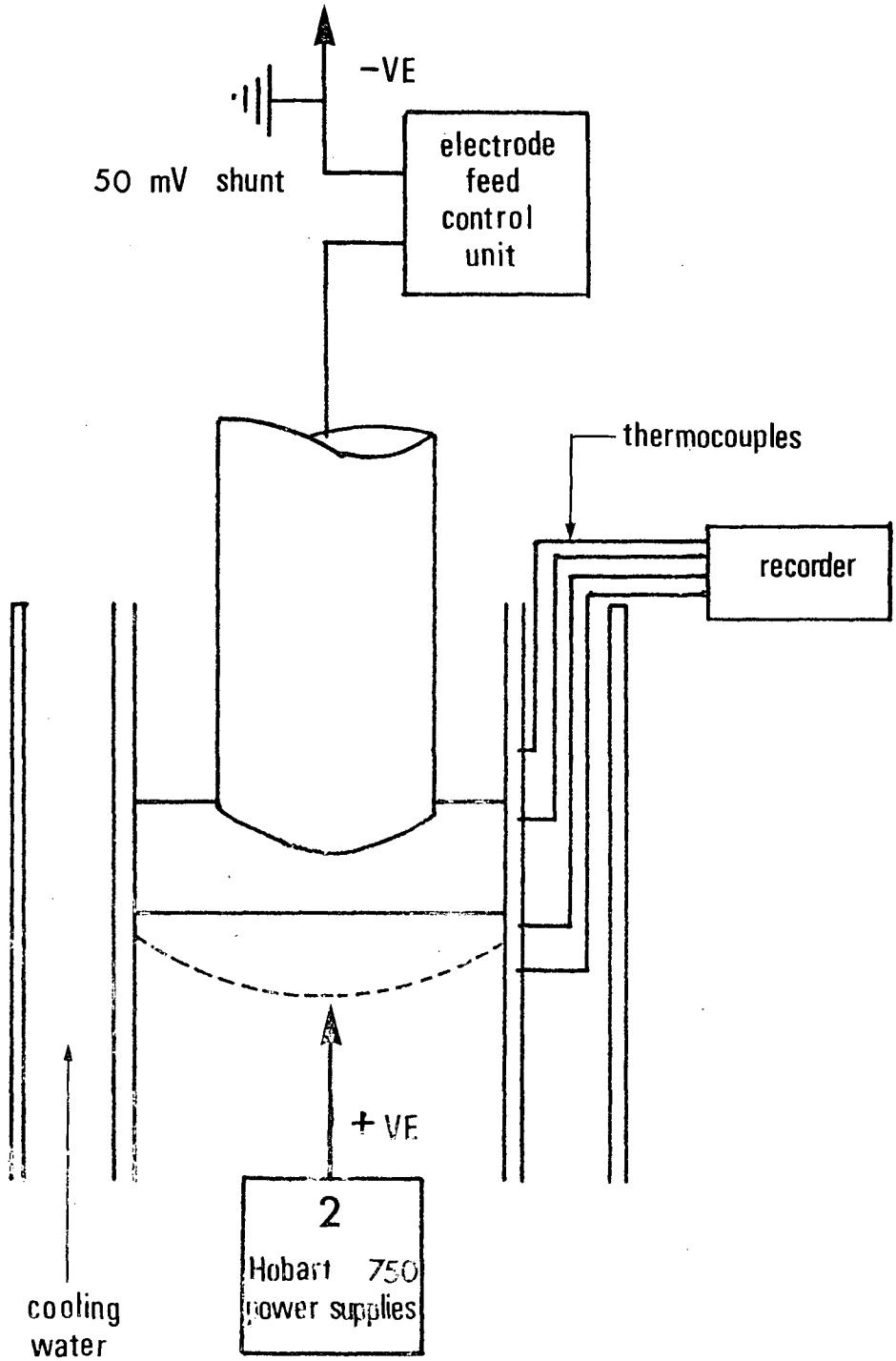

Figure 9. Schematic outline of the experimental setup for heat transfer measurements.

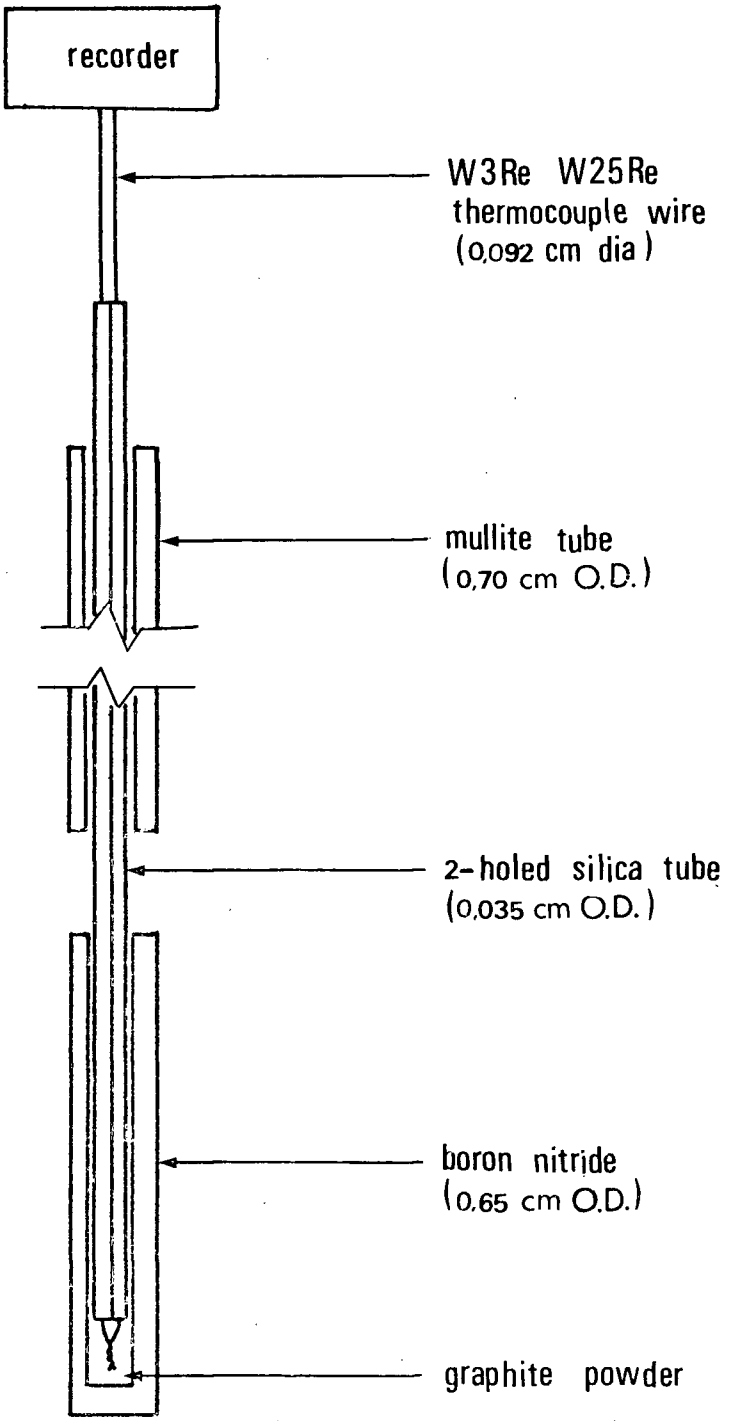

Figure 10. Thermocouple for measuring slag and metal bath temperatures.

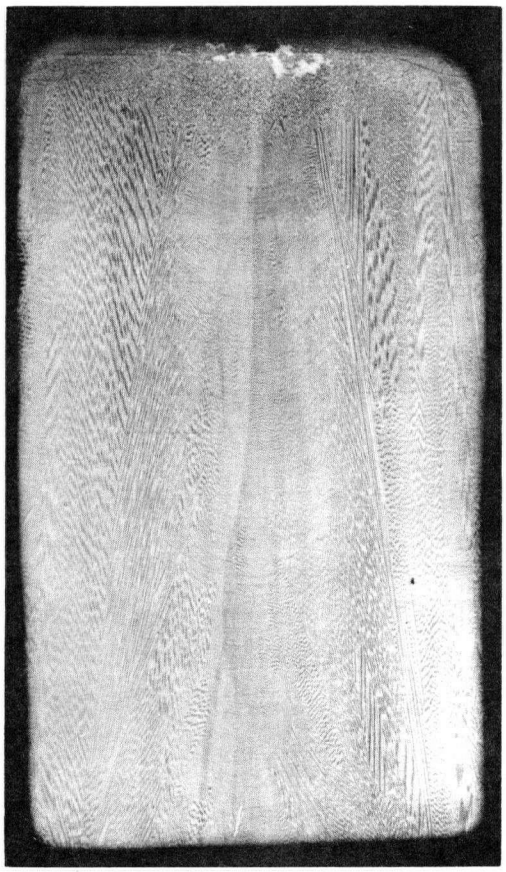

Figure 11. Macrograph of ingot no. 1 showing the steady state structure of EN-25 steel Etch:Oberhoffer's reagent.

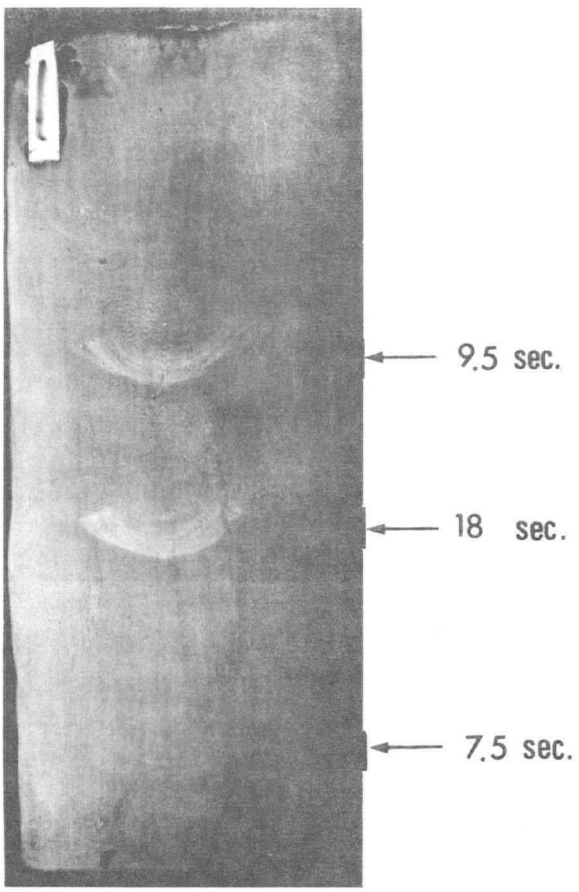

Figure 12. Macrograph of ingot no. 3 containing three power interruptions, Etch:Oberhoffer's reagent.

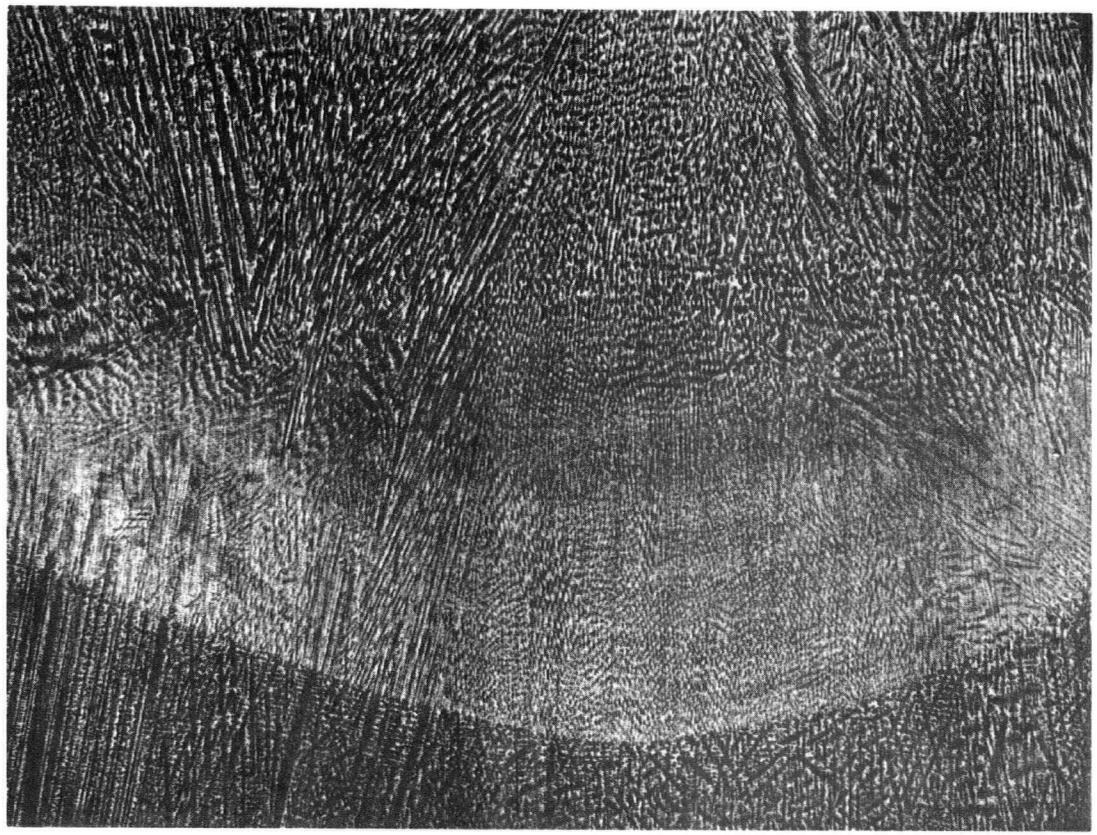

Figure 13. Micrograph of the 18 sec power interruption in ingot no. 3 mag. 6X, Etch:Oberhoffer's reagent.

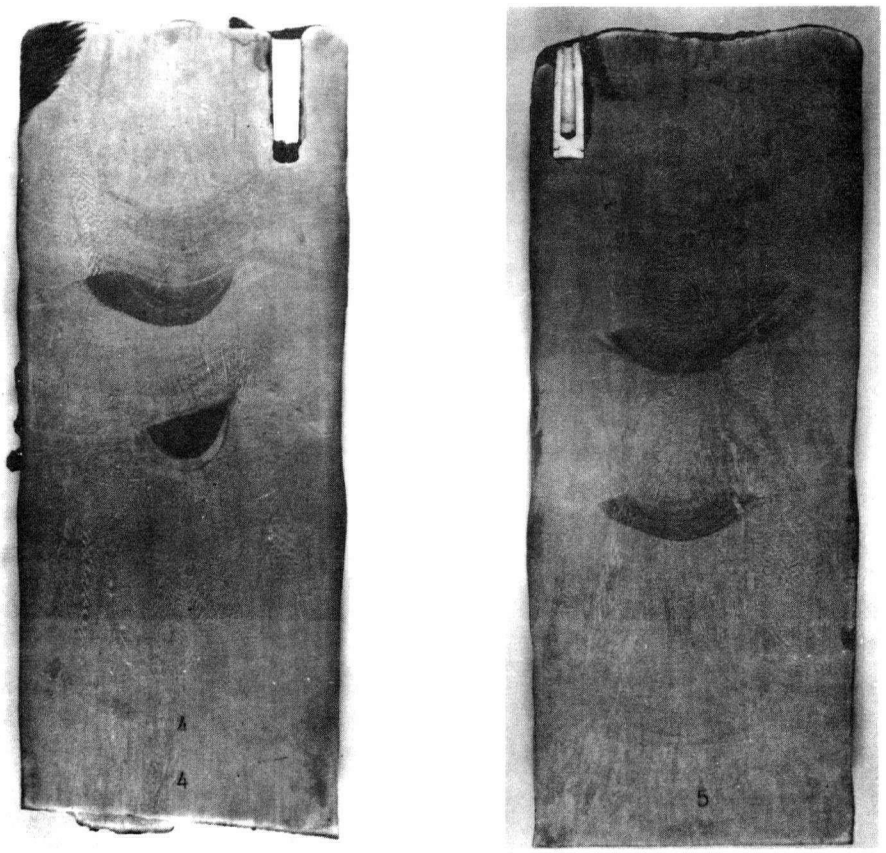

Figure 14. Macrographs of ingots etched with 3 percent nital. (A) ingot no. 2 and (B) ingot no. 3.

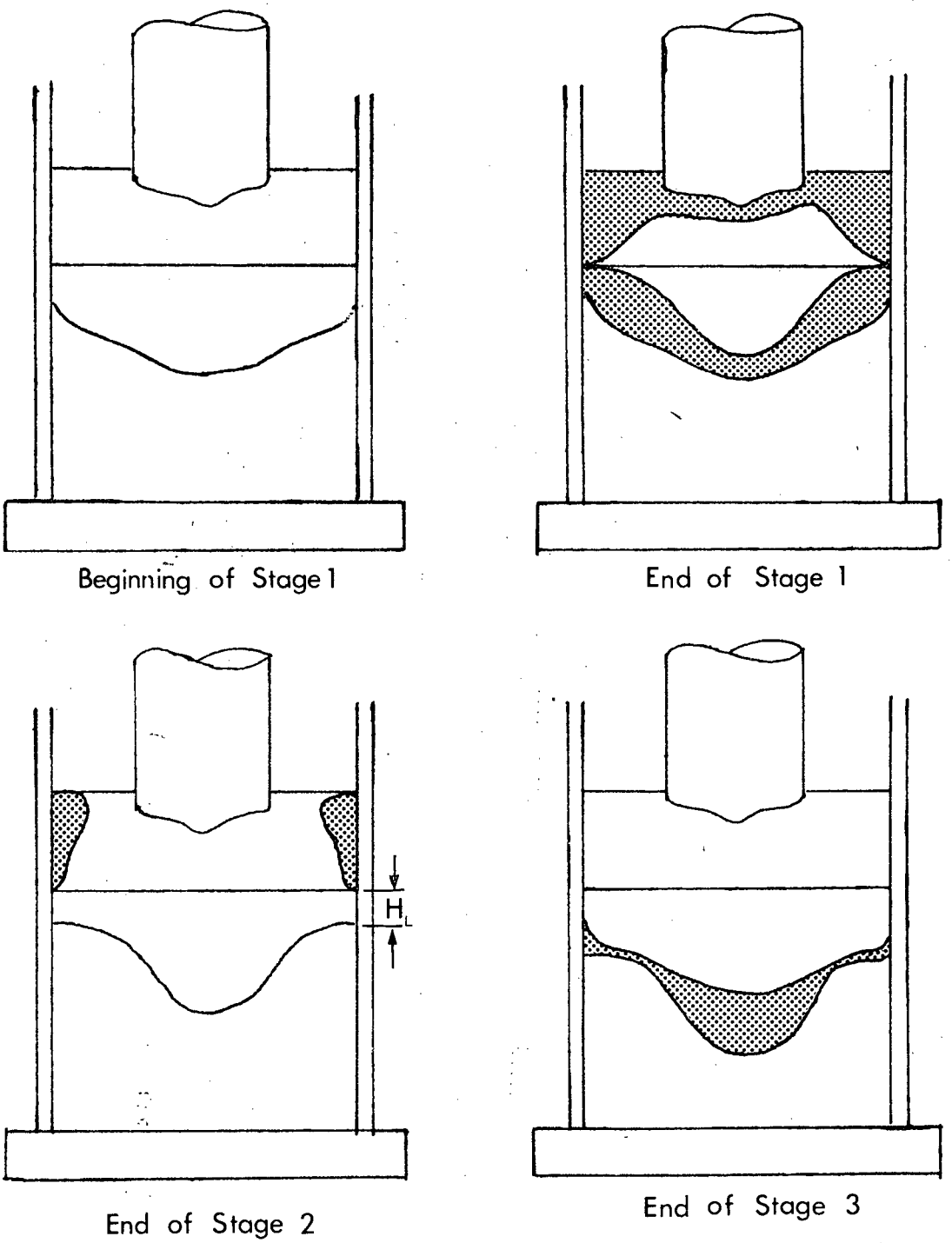

Figure 15. Schematic representation of the carbon band formation model.

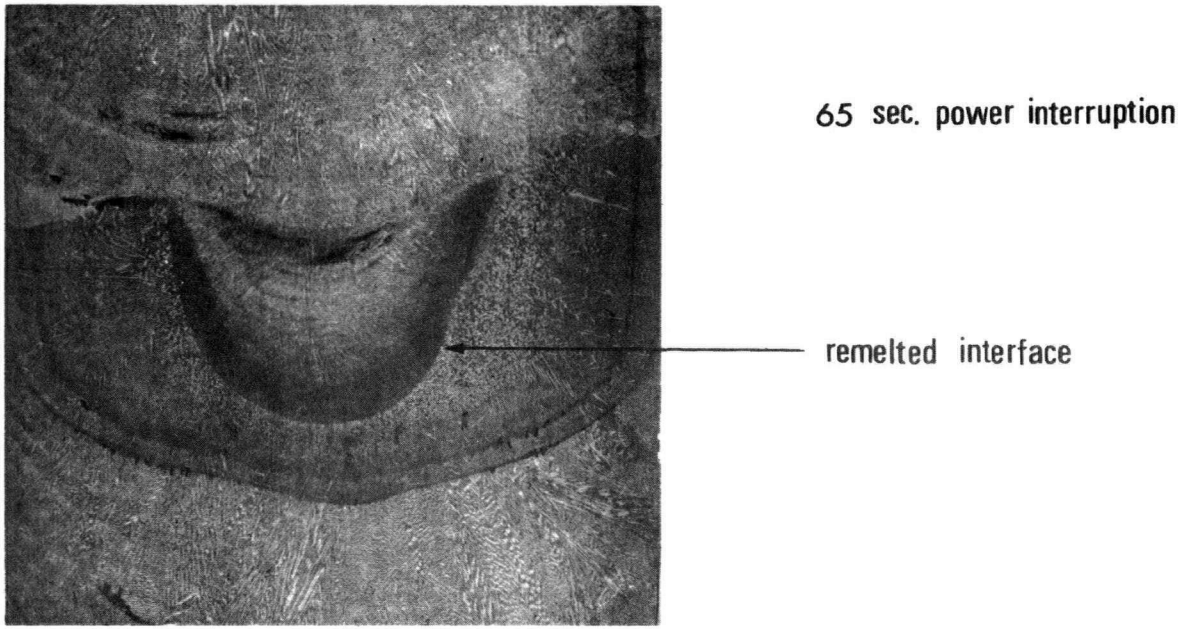

Figure 16. Pool profile outlined with W powder additions (ingot no. 13) Etch 3% Nital.

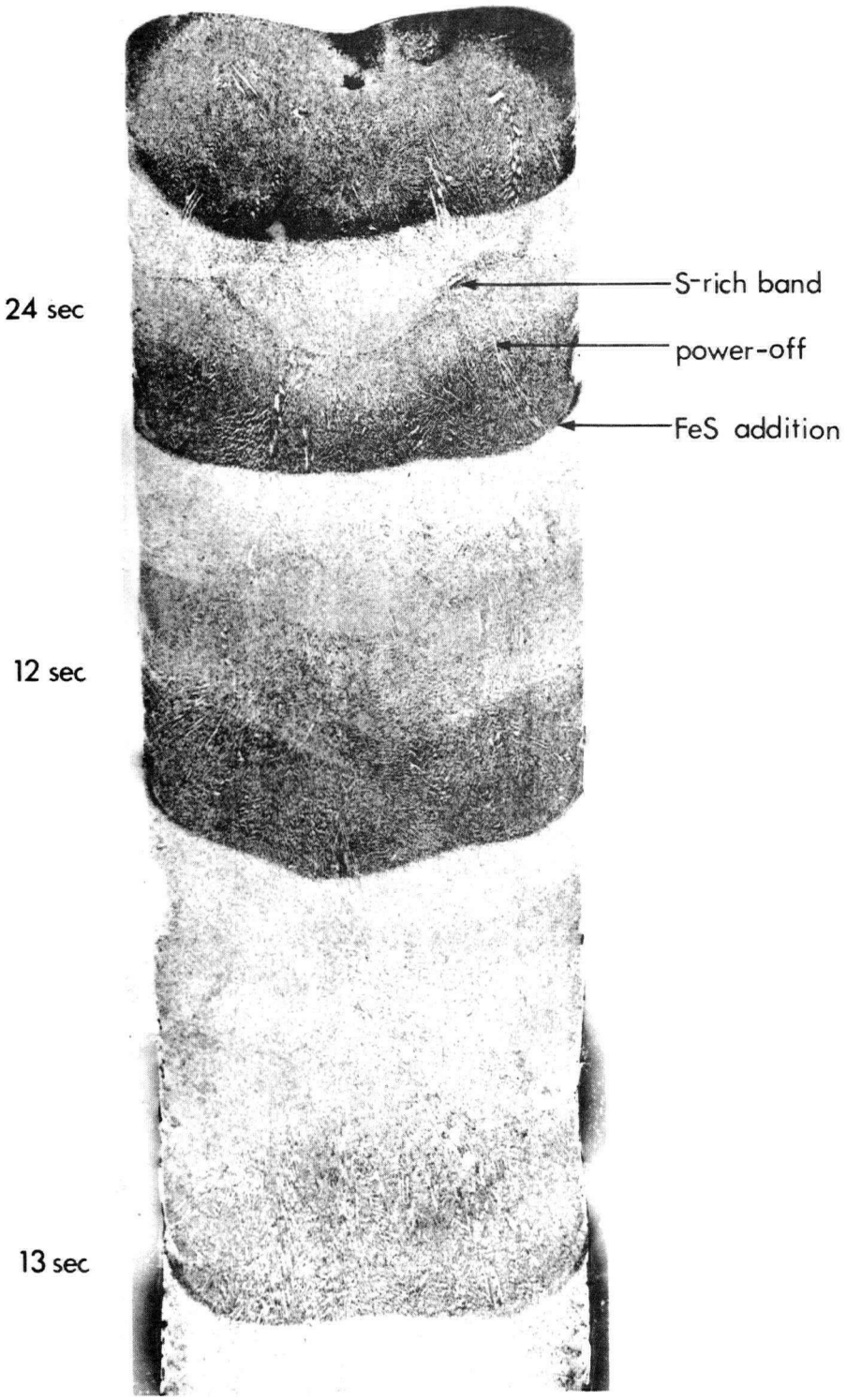

Figure 17. Sulphur print of ingot no. 6 containing several power interruptions.

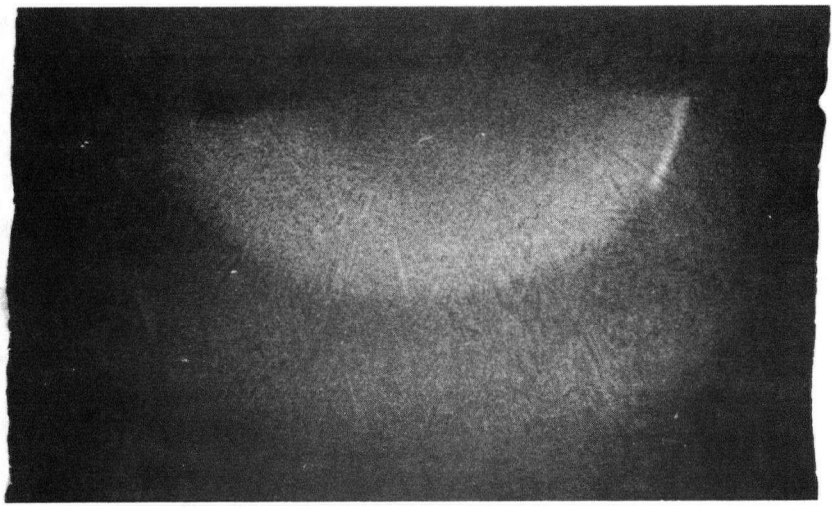

Figure 18. Autoradiograph of a section from ingot no. 11 containing a 23 second power interruption.

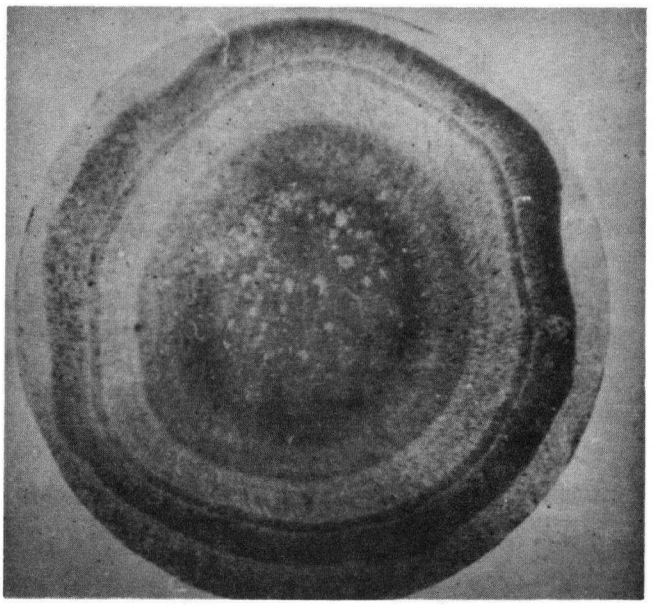

Figure 19. "Tree-ring" banding in a high carbon alloy steel produced by vacuum arc remelting.

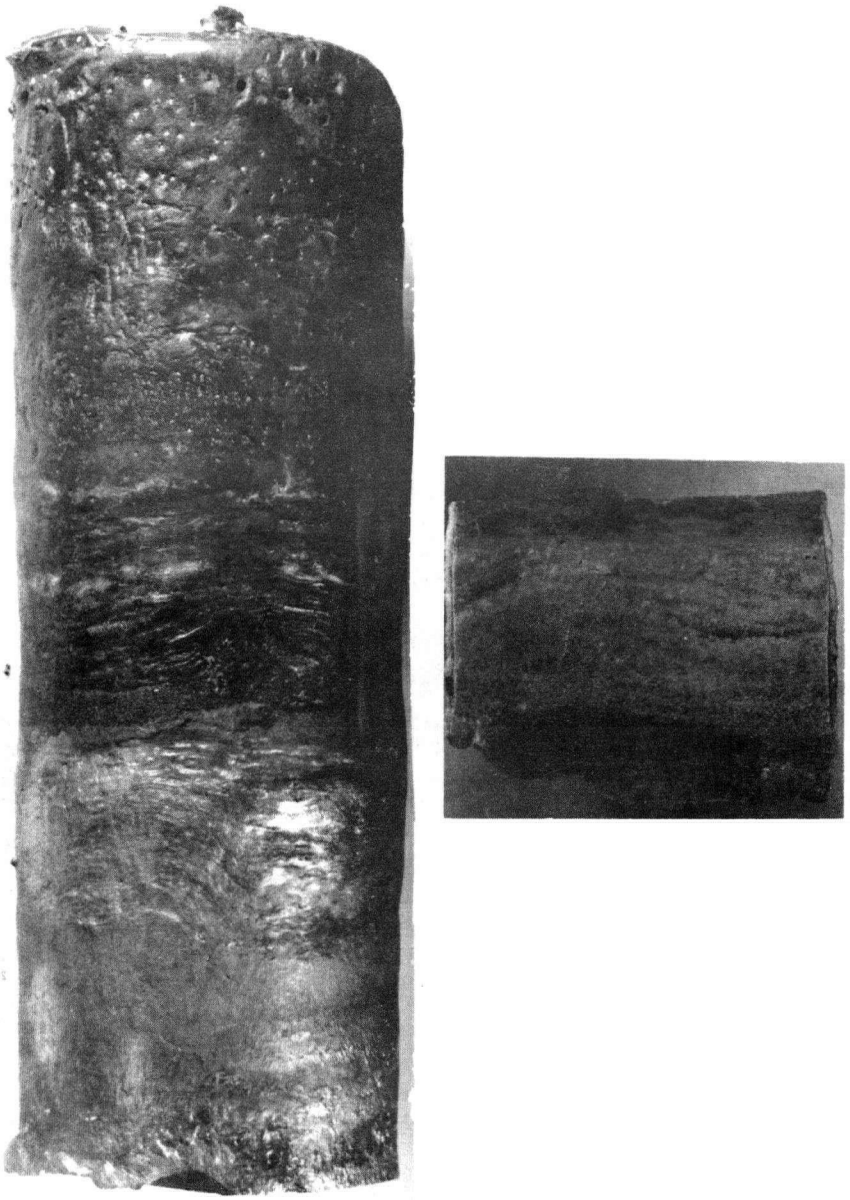

Figure 20. Irregularities in the slag skin thickness reproduced in the metal.

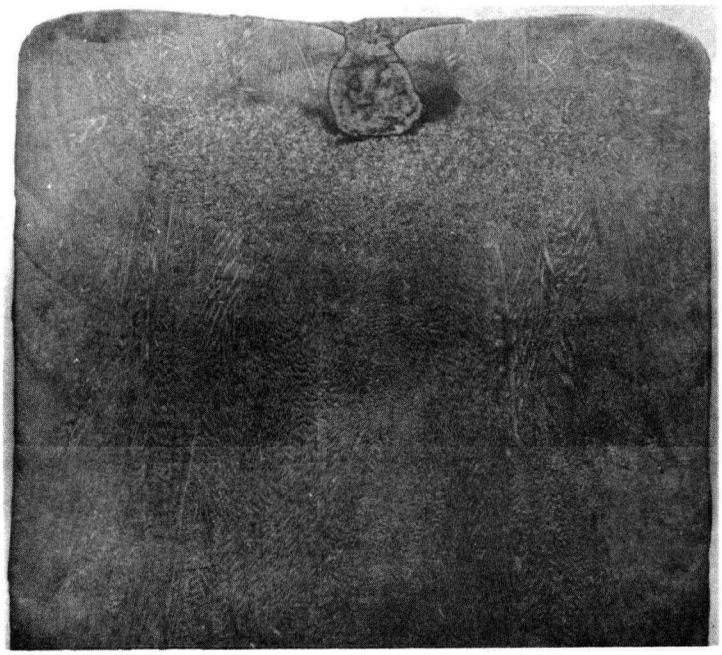

Figure 21. Banding in ingot no. 13 produced by irregularities in the slag skin thickness, Etch 3% Nital.

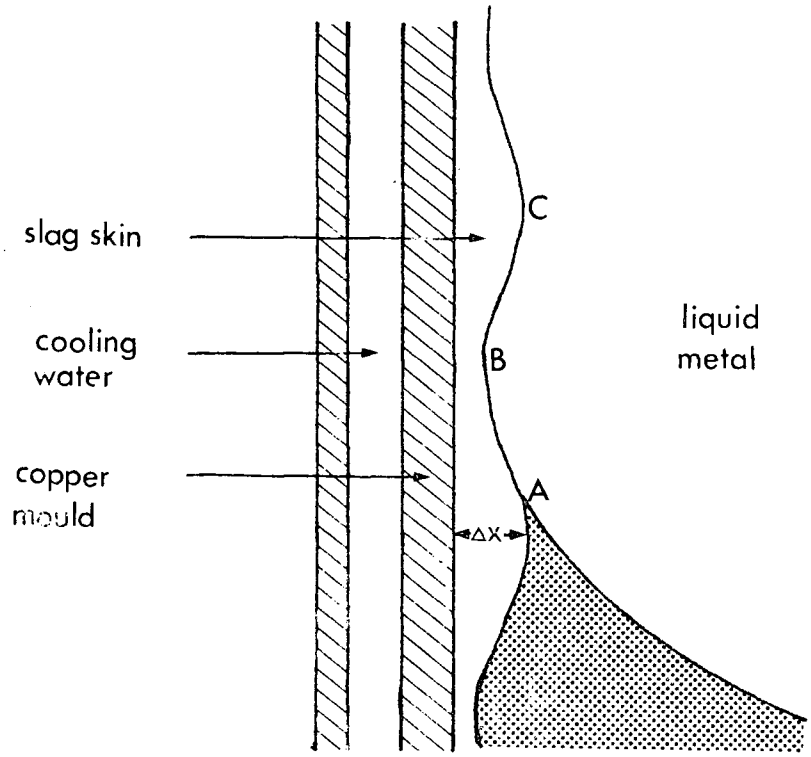

Figure 22. Schematic representation of banding due to irregularities in the slag skin thickness.

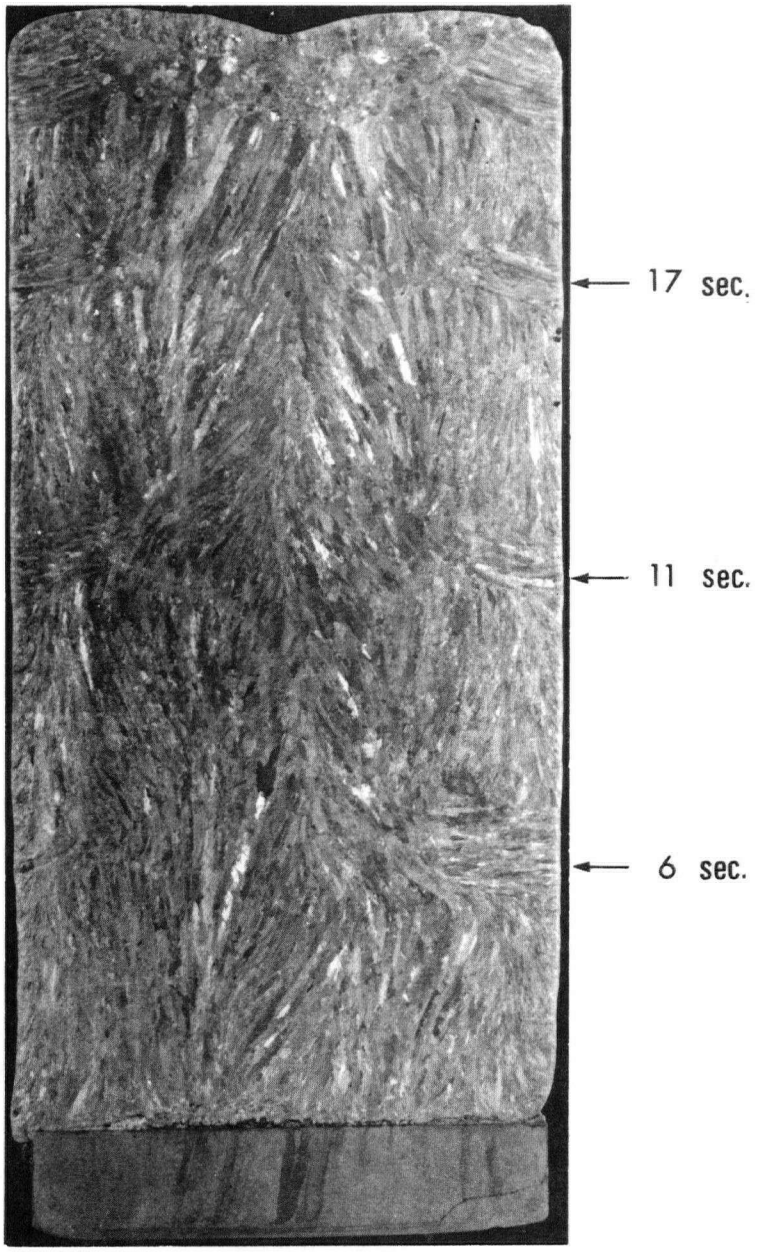

Figure 23. Macrograph of ingot no. 14 containing several power interruptions, Etch 100 ml ethyl alcohol, 100 ml HCl, 50 ml HNO_3.

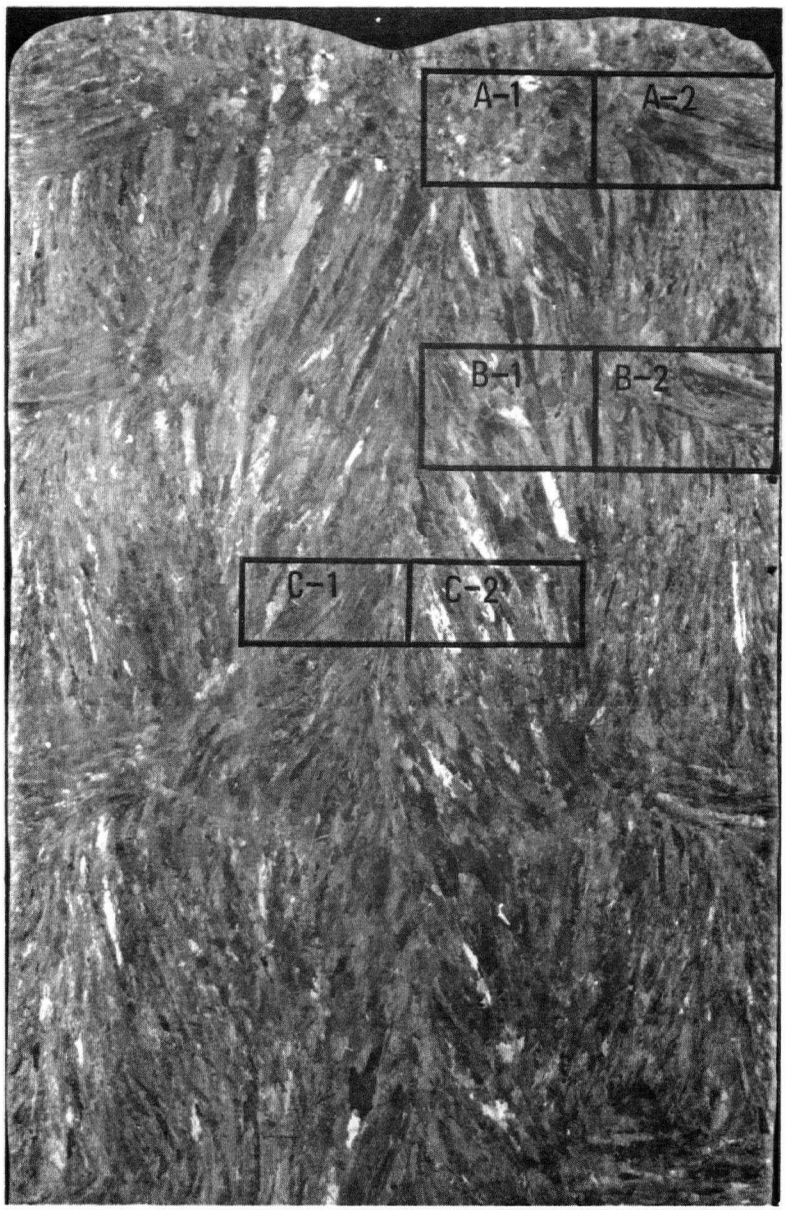

Figure 24. Location of specimens from ingot no. 14 for analysis on the electron probe.

Figure 25. Concentration banding in a commercial AISI 630 ingot.

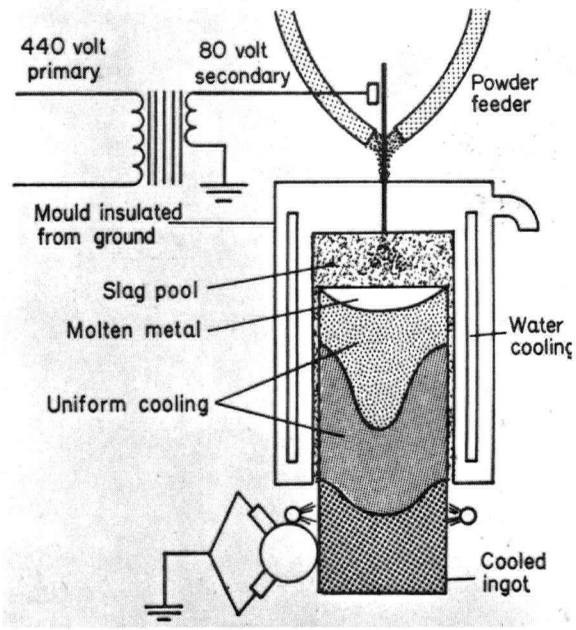

Figure 26. Arcos Corporation's continuous casting ESR process.

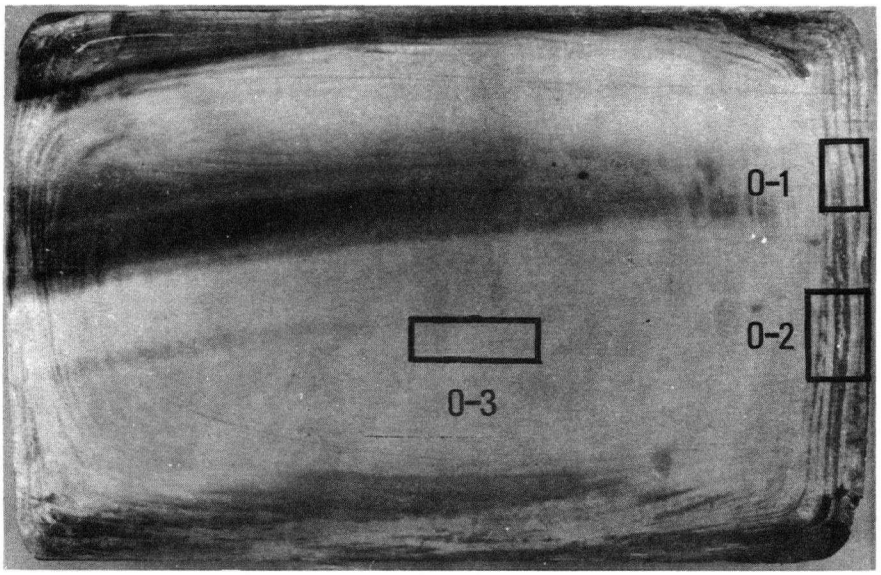

Figure 27. Location of specimens used in the banding analysis.

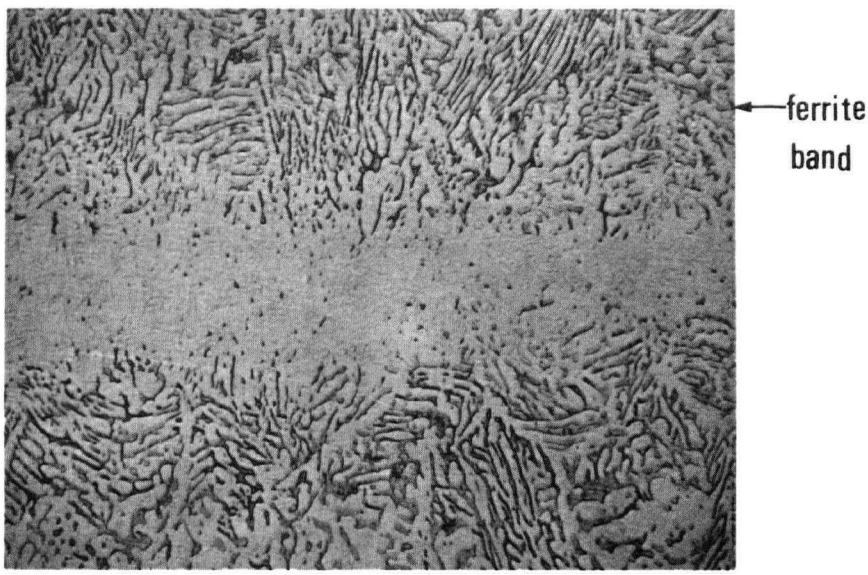

Figure 28. Micrograph of the banded structure. X 48
Etch: Kalling's reagent.

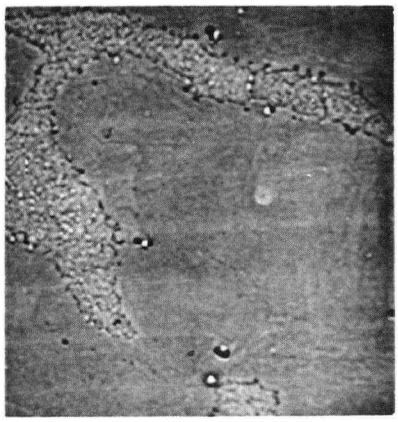

Absorbed electron image

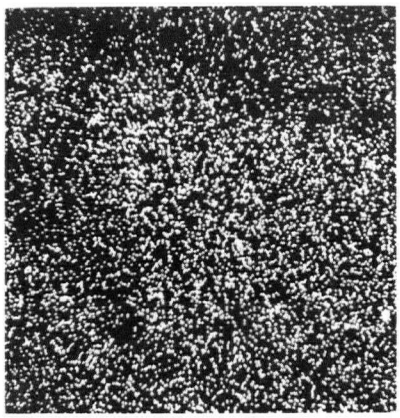

Ni X-ray image

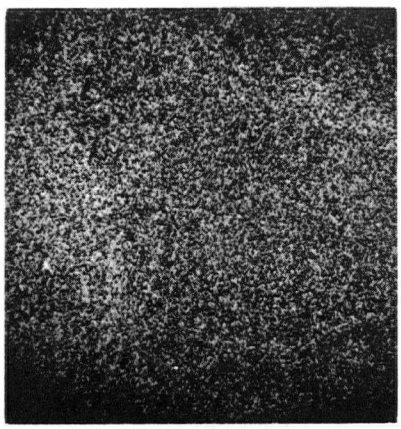

Cr X-ray image

Figure 29. Absorbed electron image and X-ray images for nickel and chromium in the banded area X 1000.

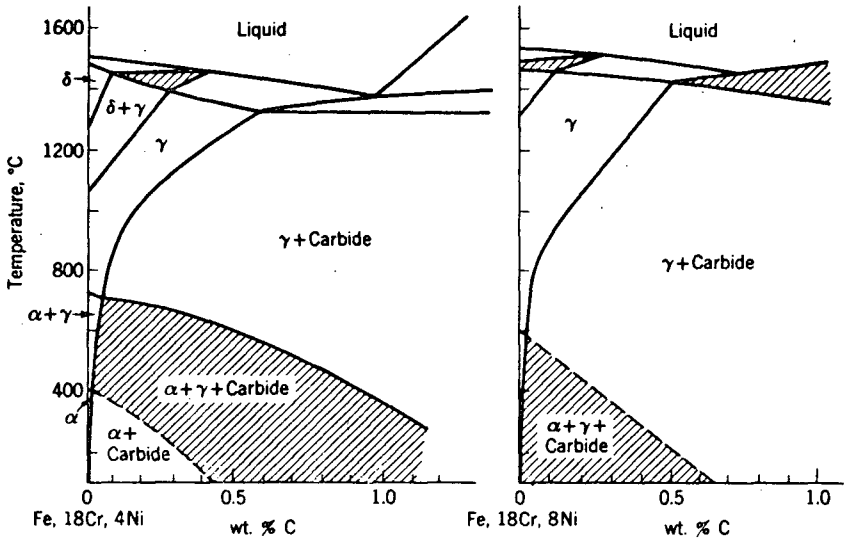

Figure 30. Pesudo-binary phase diagrams of Fe + 18% Cr + 4% Ni versus varying carbon content and Fe + 18% Cr + 8% Ni versus varying carbon content.

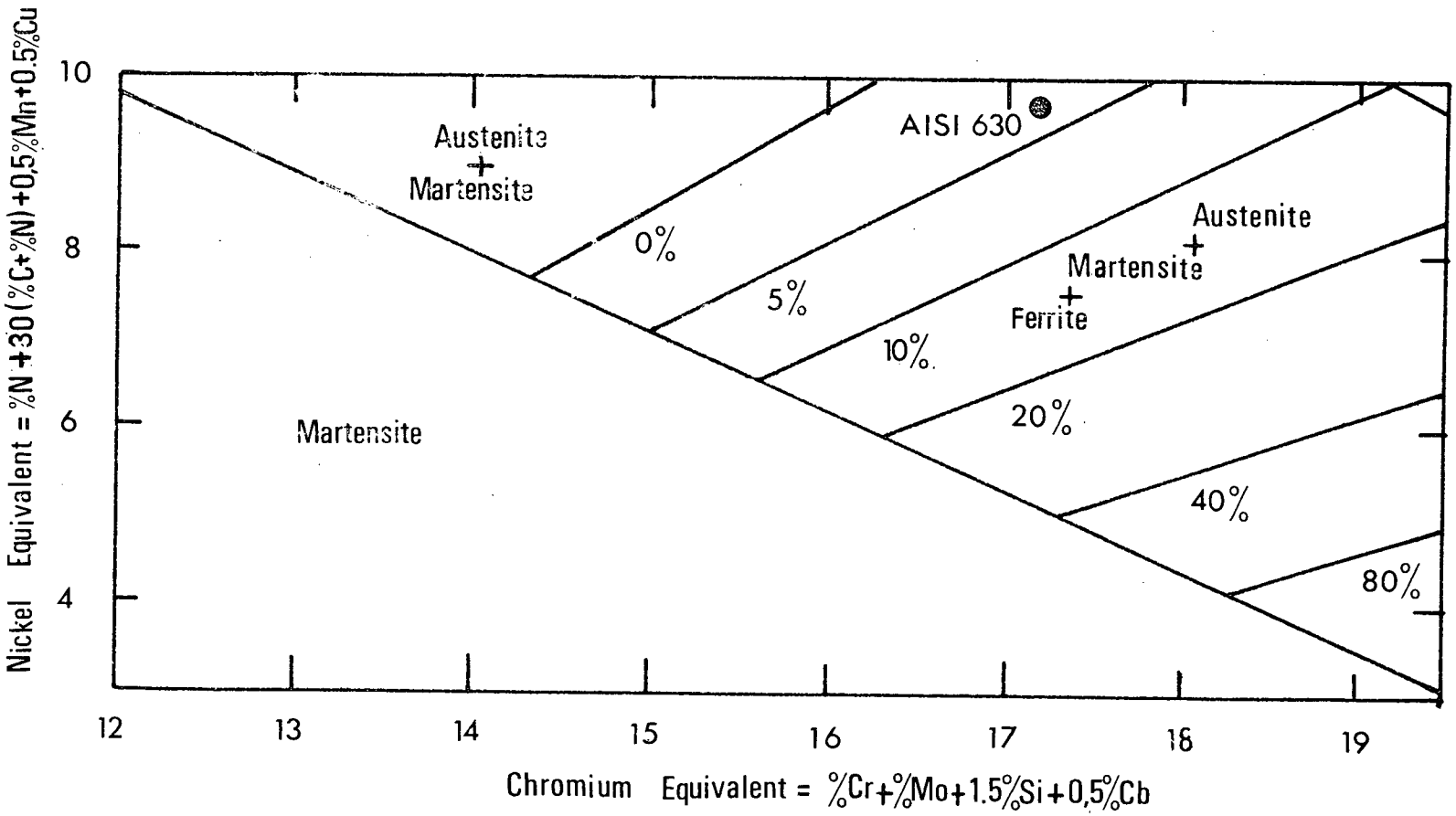

Figure 31. Schaeffler ferrite diagram for AISI 630 steel.

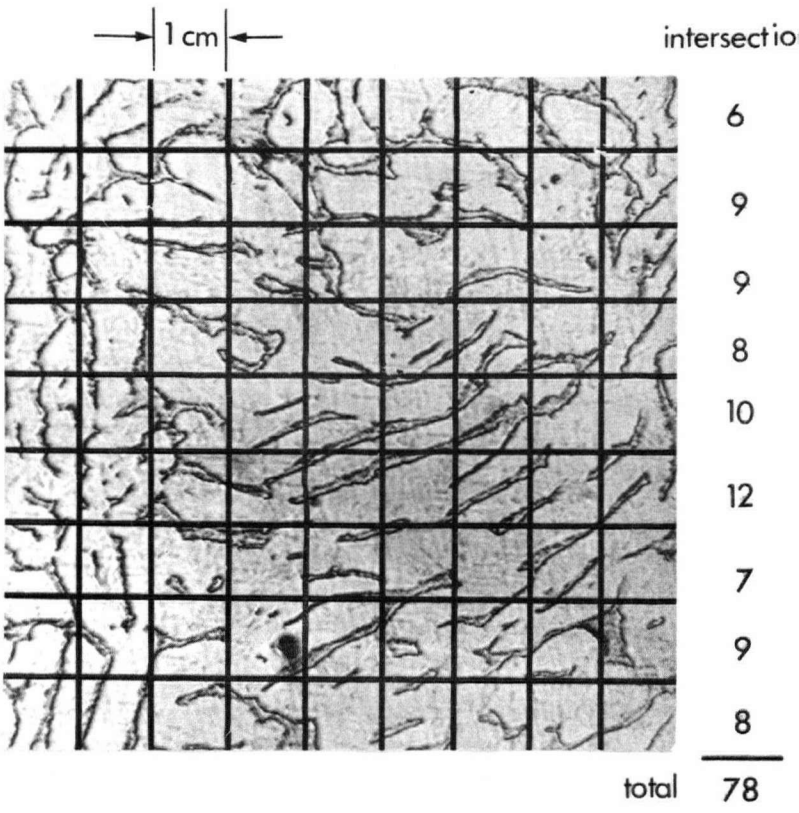

Figure 32. Standard line count for percent ferrite determination.

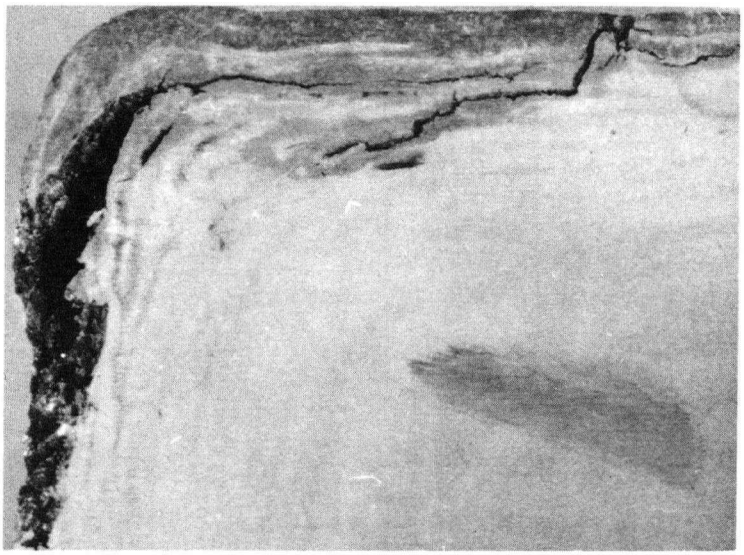

cross-section

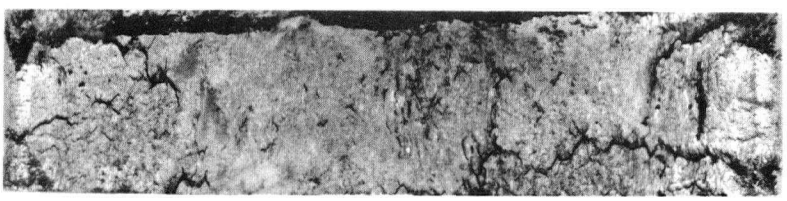

edge

Figure 33. Crack formation during rolling.

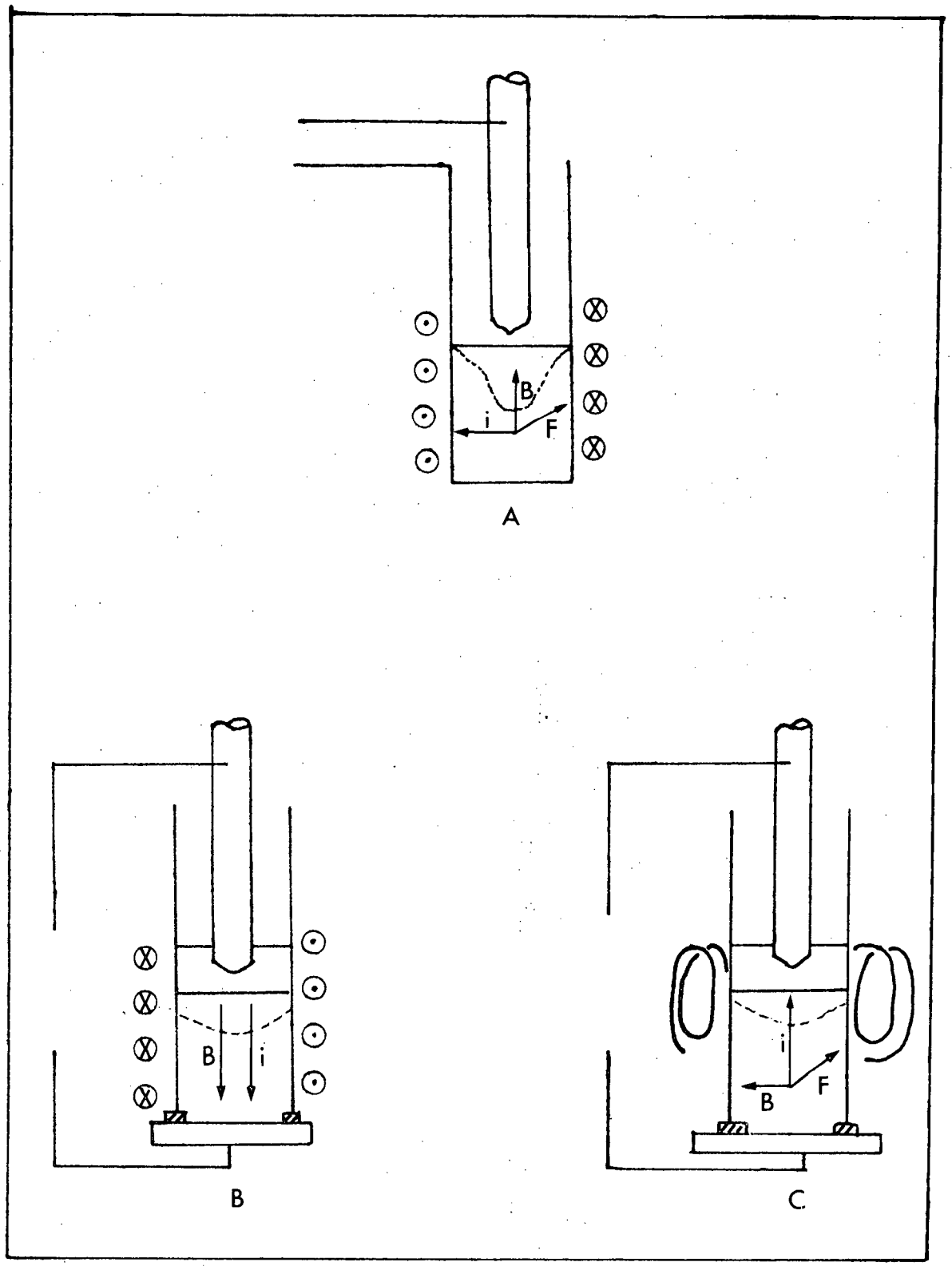

Figure 34. Different electromagnetic stirring coil configurations.

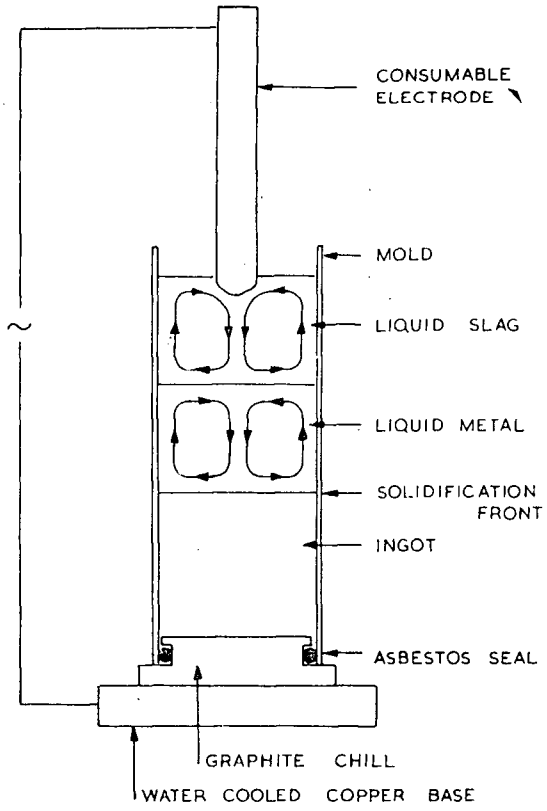

Figure 35. Convective motion in the slag and metal pool produced by the falling metal droplets.

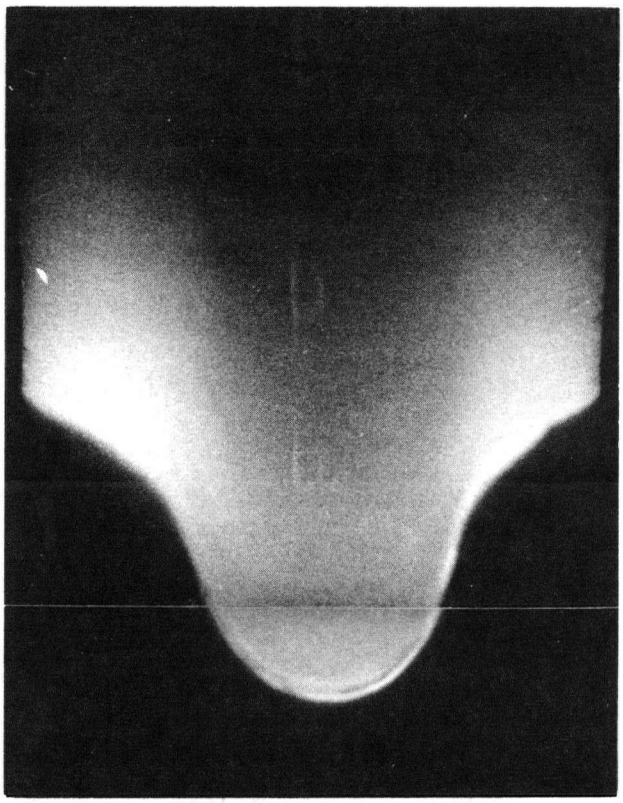

Figure 36. Autoradiograph of ingot no. 10.

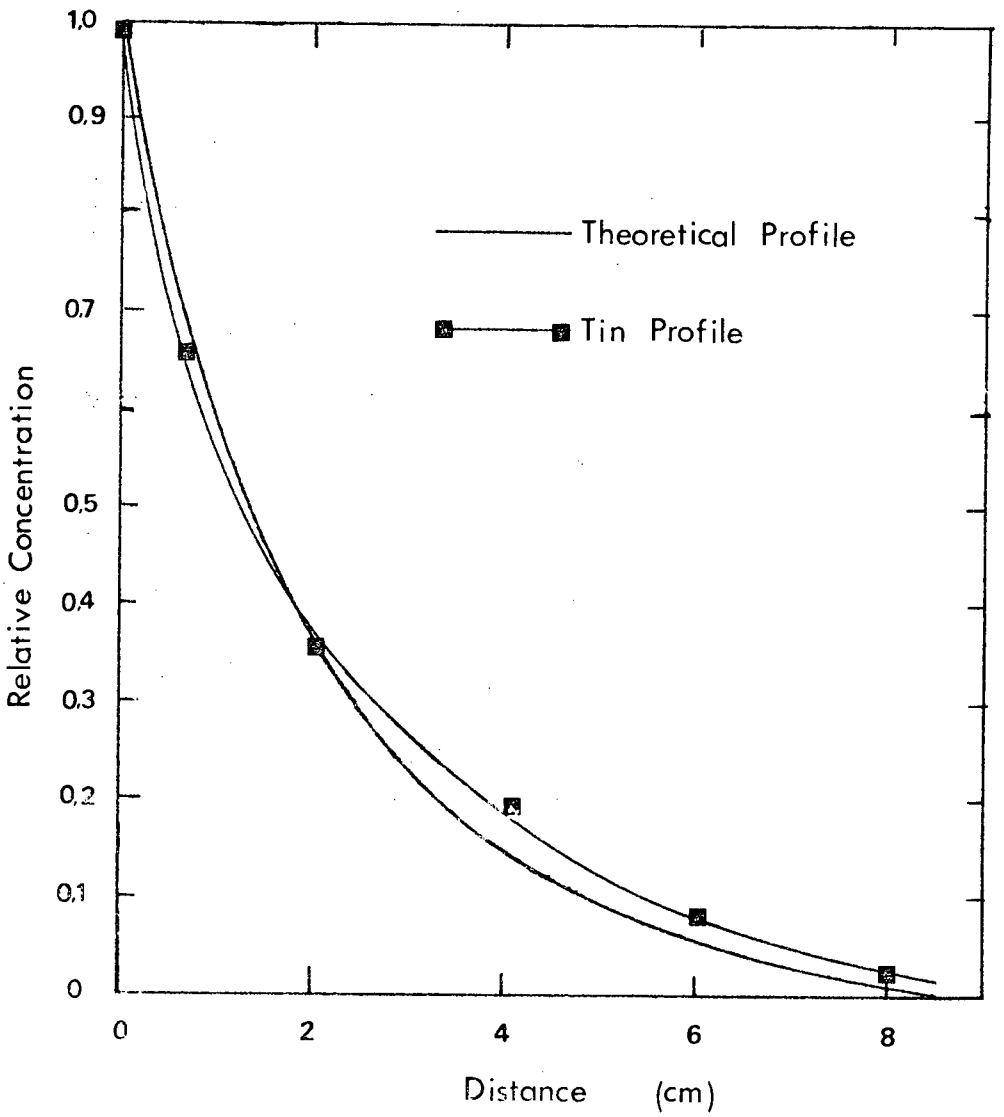

Figure 37. Plot of the relative concentrations of radioactive tin versus axial distance from the original interface.

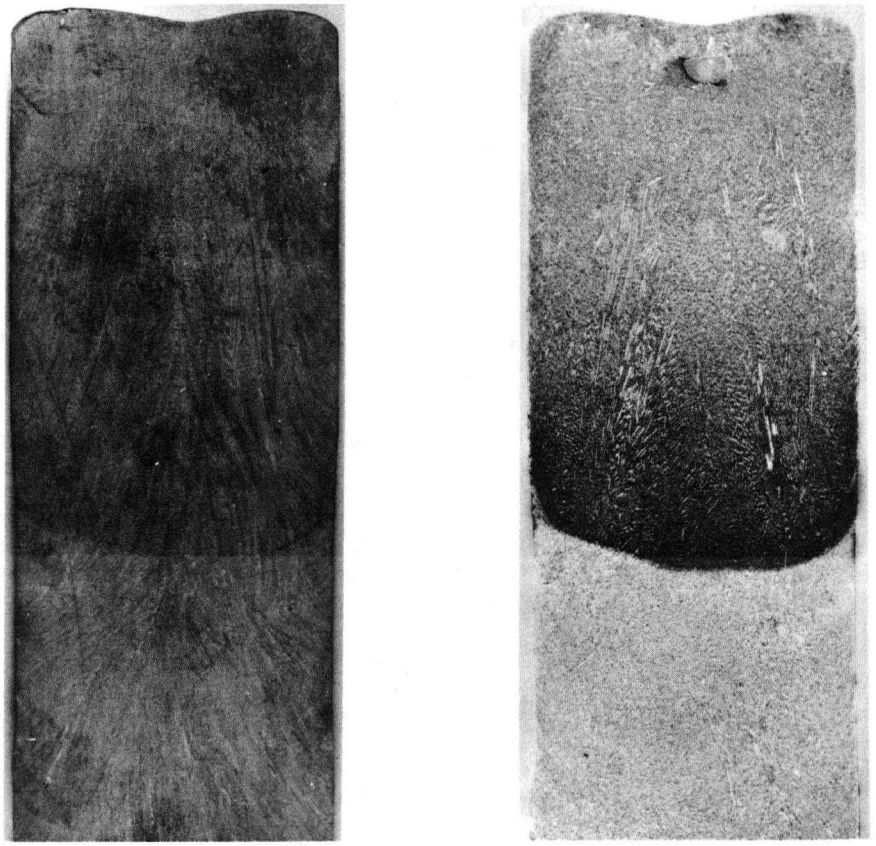

A B

Figure 38. Pool profile outlined by (A) tungsten powder, (B) iron sulphide.

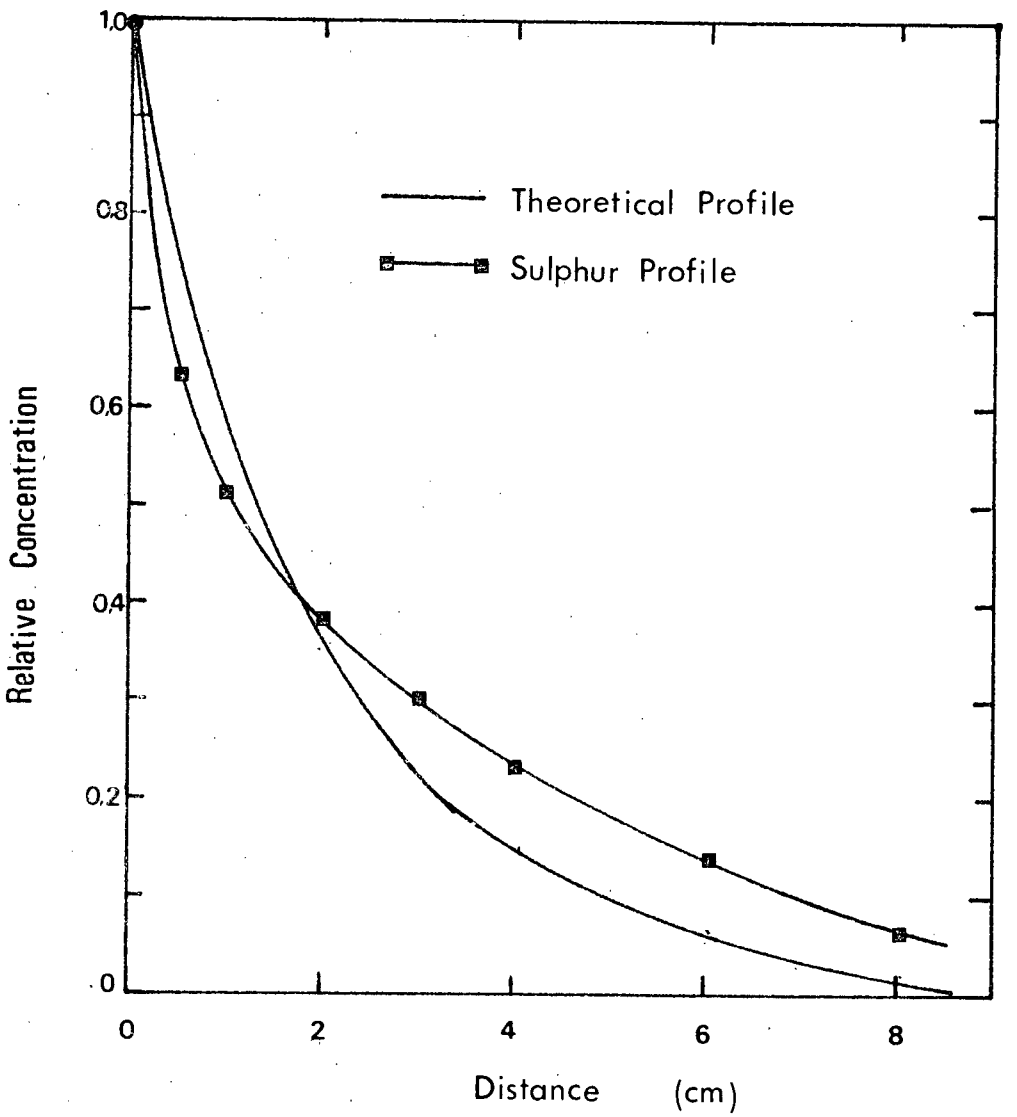

Figure 39. Plot of the relative concentrations of sulphur versus axial distance from the original interface.

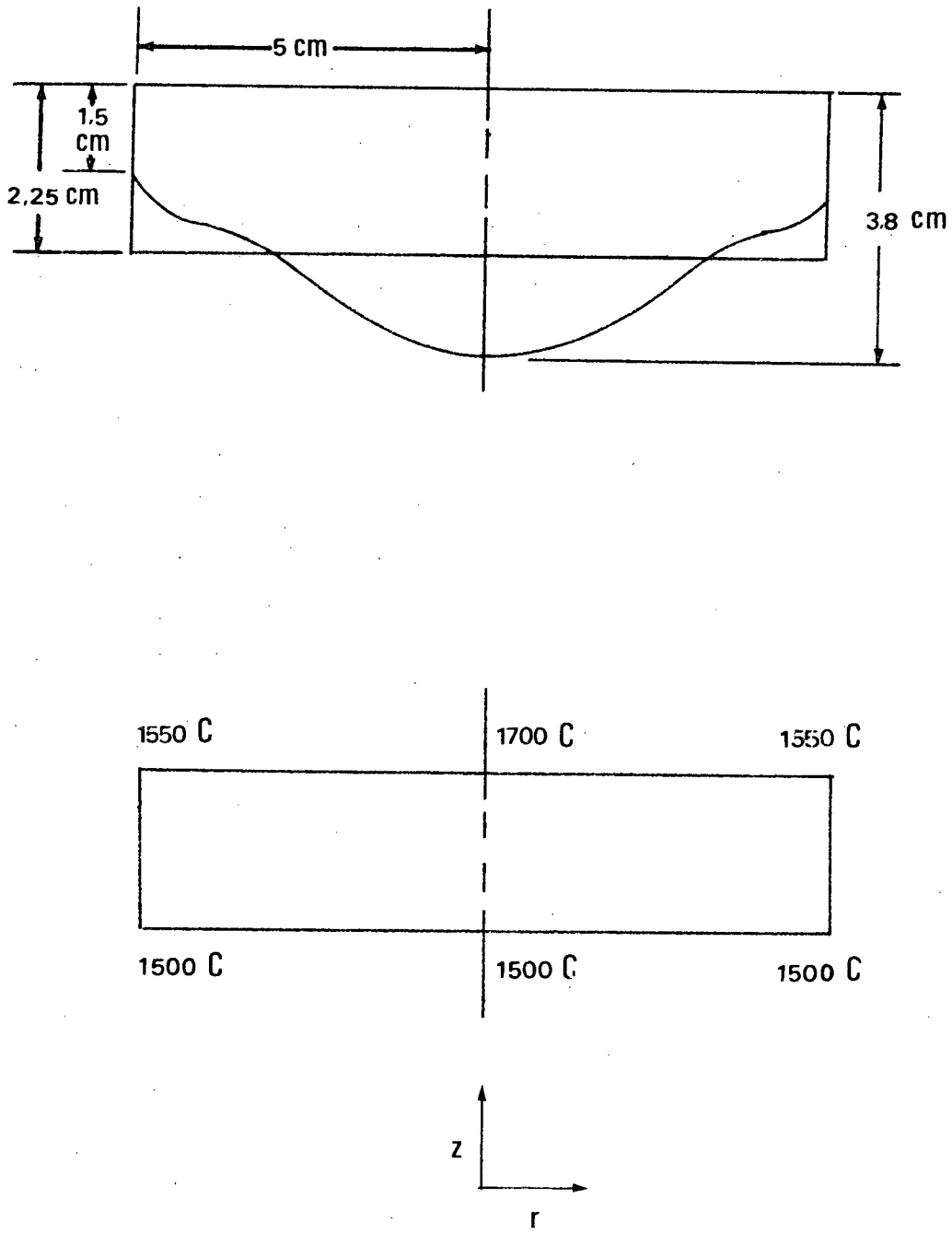

Figure 40. Assumed pool geometry and imposed boundary temperatures in a 10 cm dia. ESR ingot.

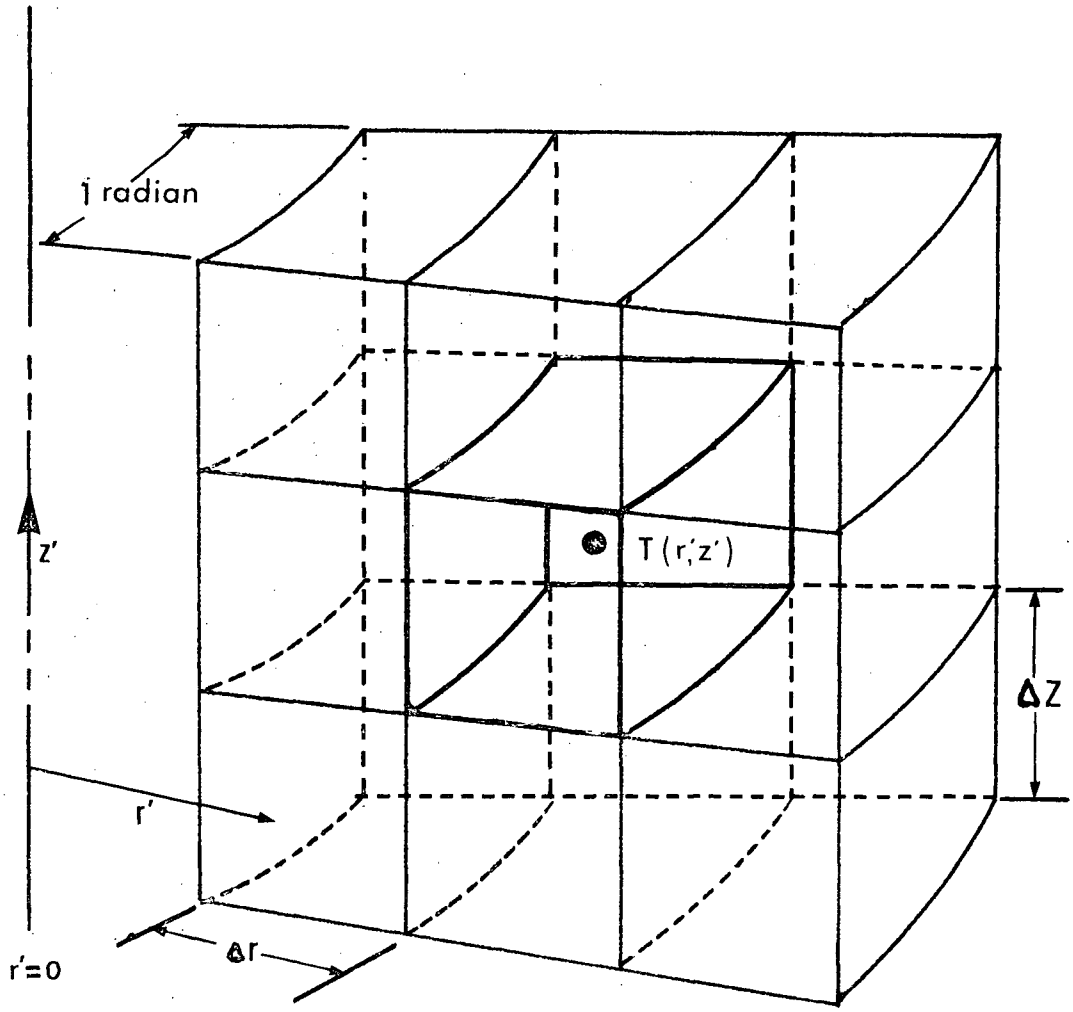

Figure 41. Subdivision of the metal pool.

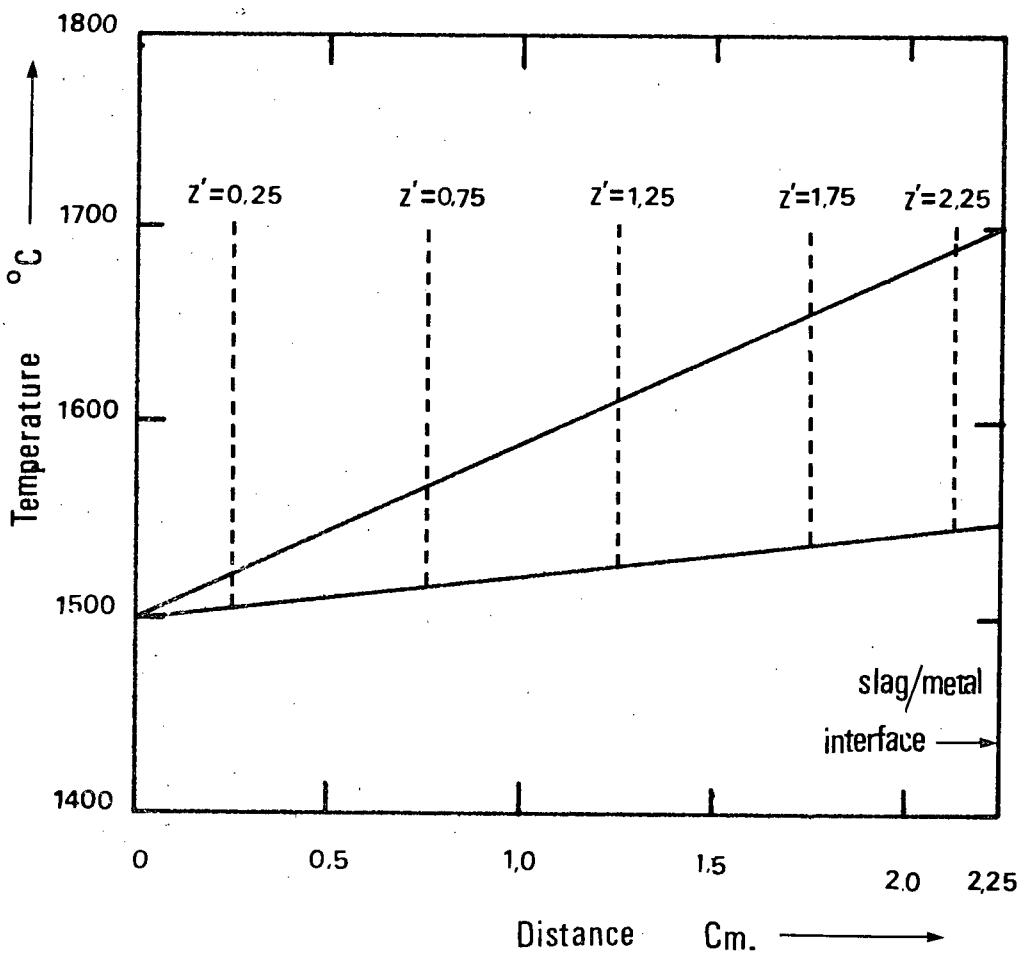

Figure 42. Assumed temperature distribution in the z direction.

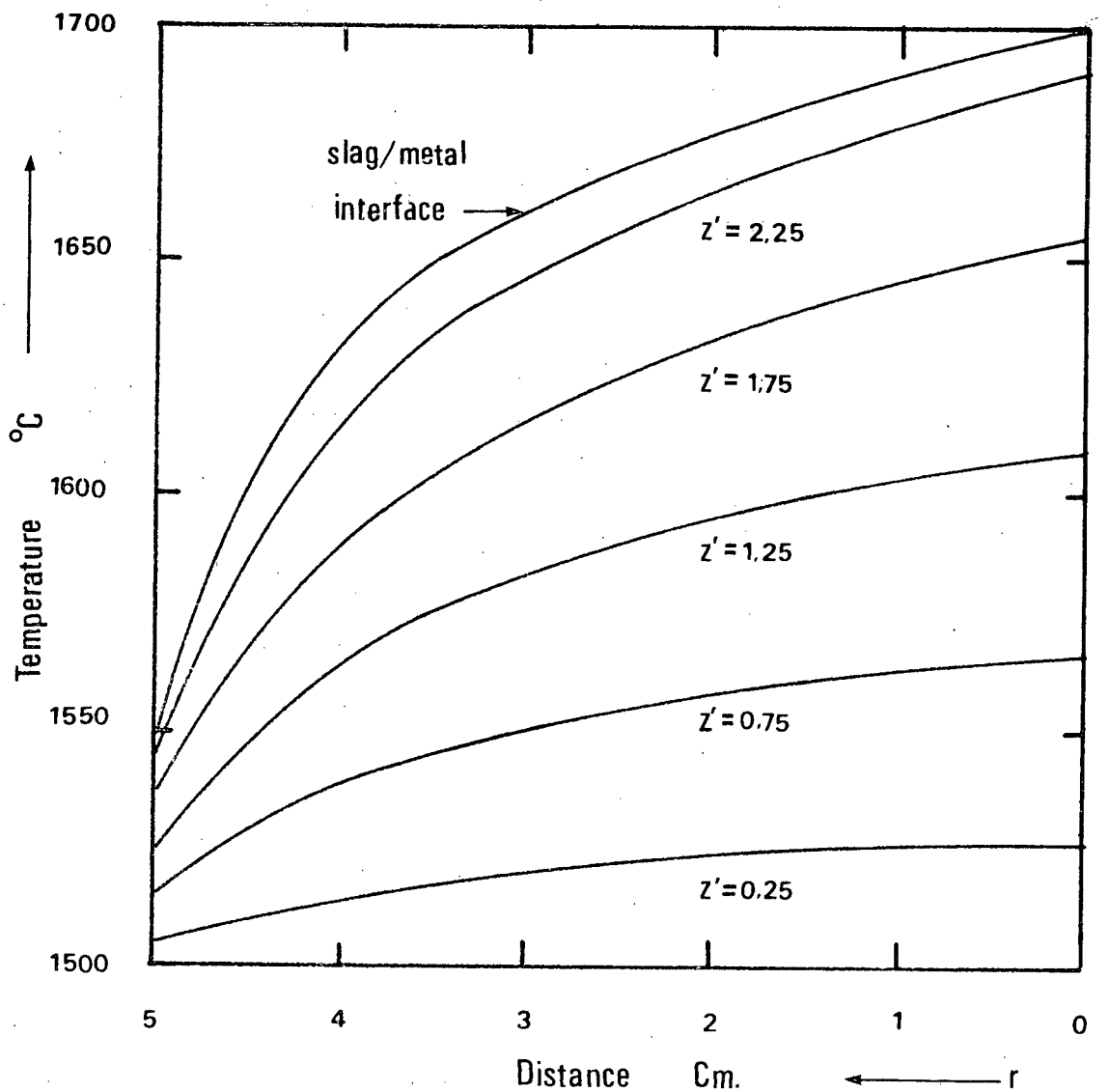

Figure 43. Assumed temperature distribution in the r direction.

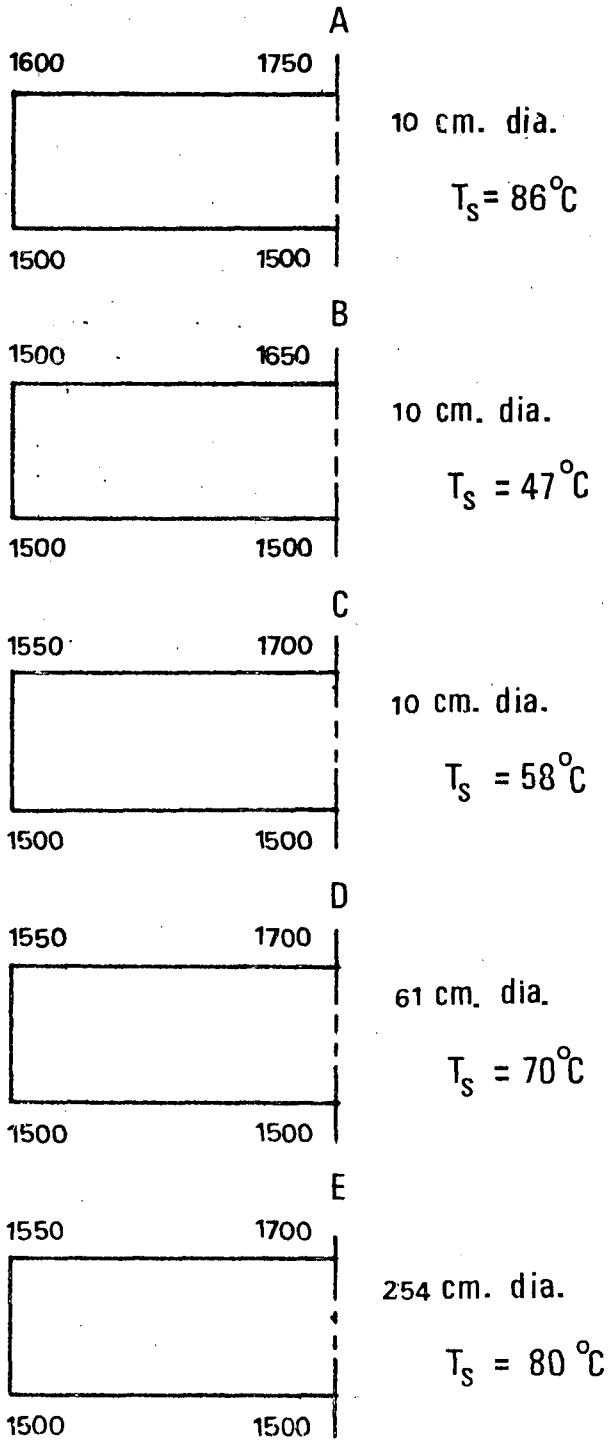

Figure 44. Assumed temperature distributions and corresponding $(\Delta Ts)_{Avg}$ values.

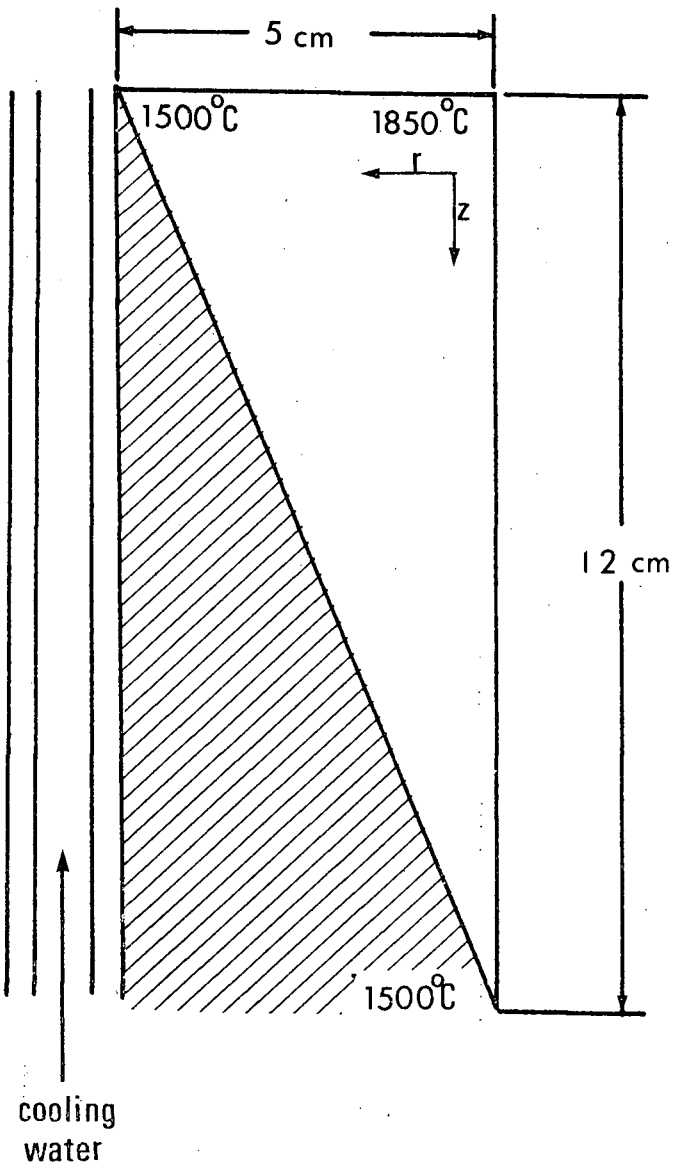

Figure 45. Assumed pool geometry and imposed boundary temperatures in a 10 cm dia. VAR ingot.

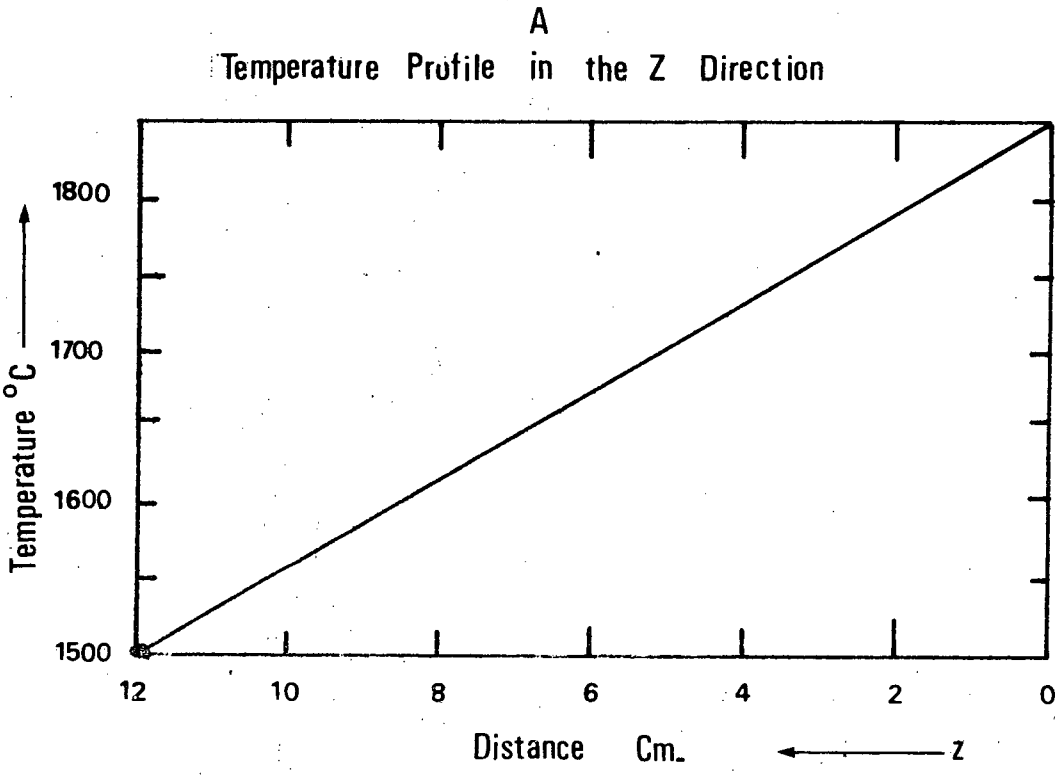

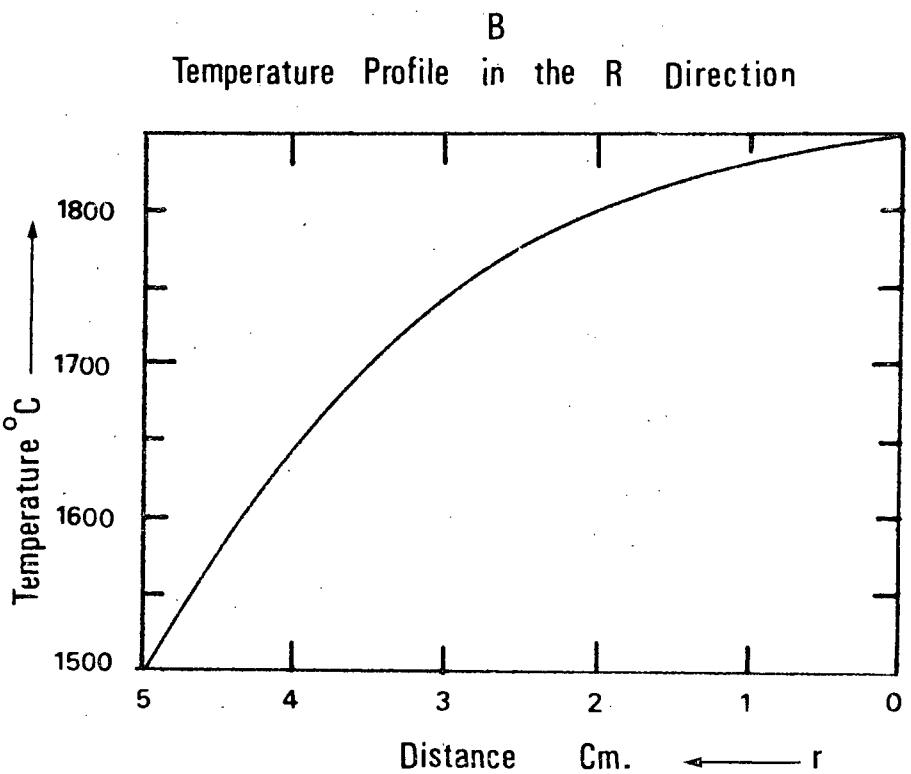

Figure 46. Assumed temperature distributions in the z and r directions.

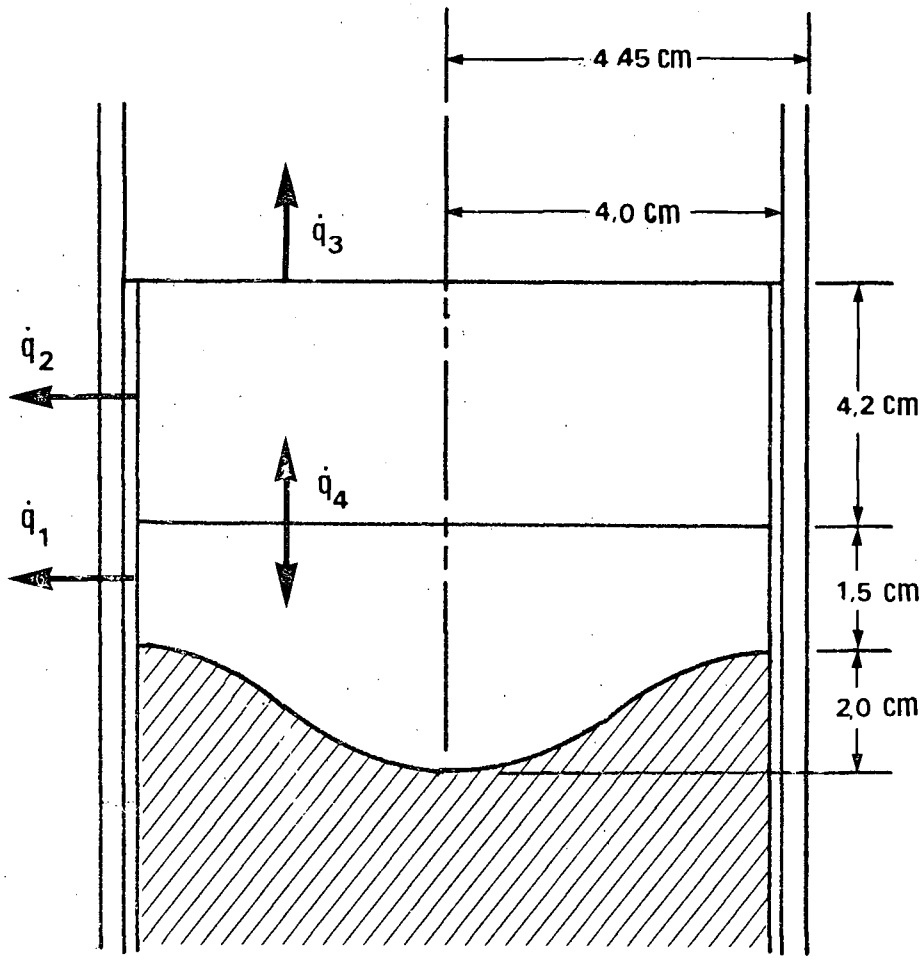

Figure 47. Regions where the rate of heat loss is effected by the "power-off" mode for a 10 cm dia. ESR ingot.

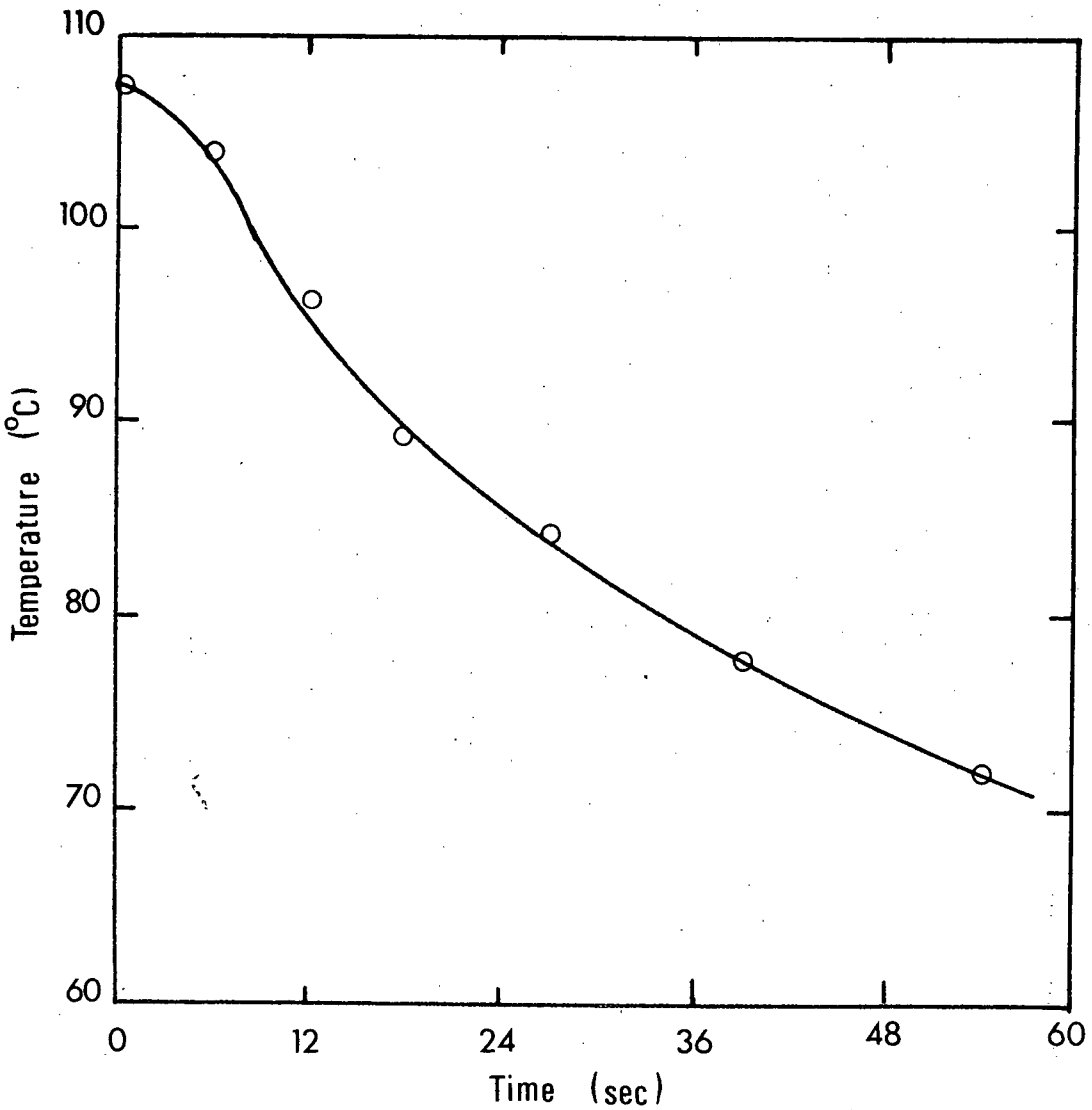

Figure 48. Plot of the change in the mould wall temperature versus time during the "power-off" mode.

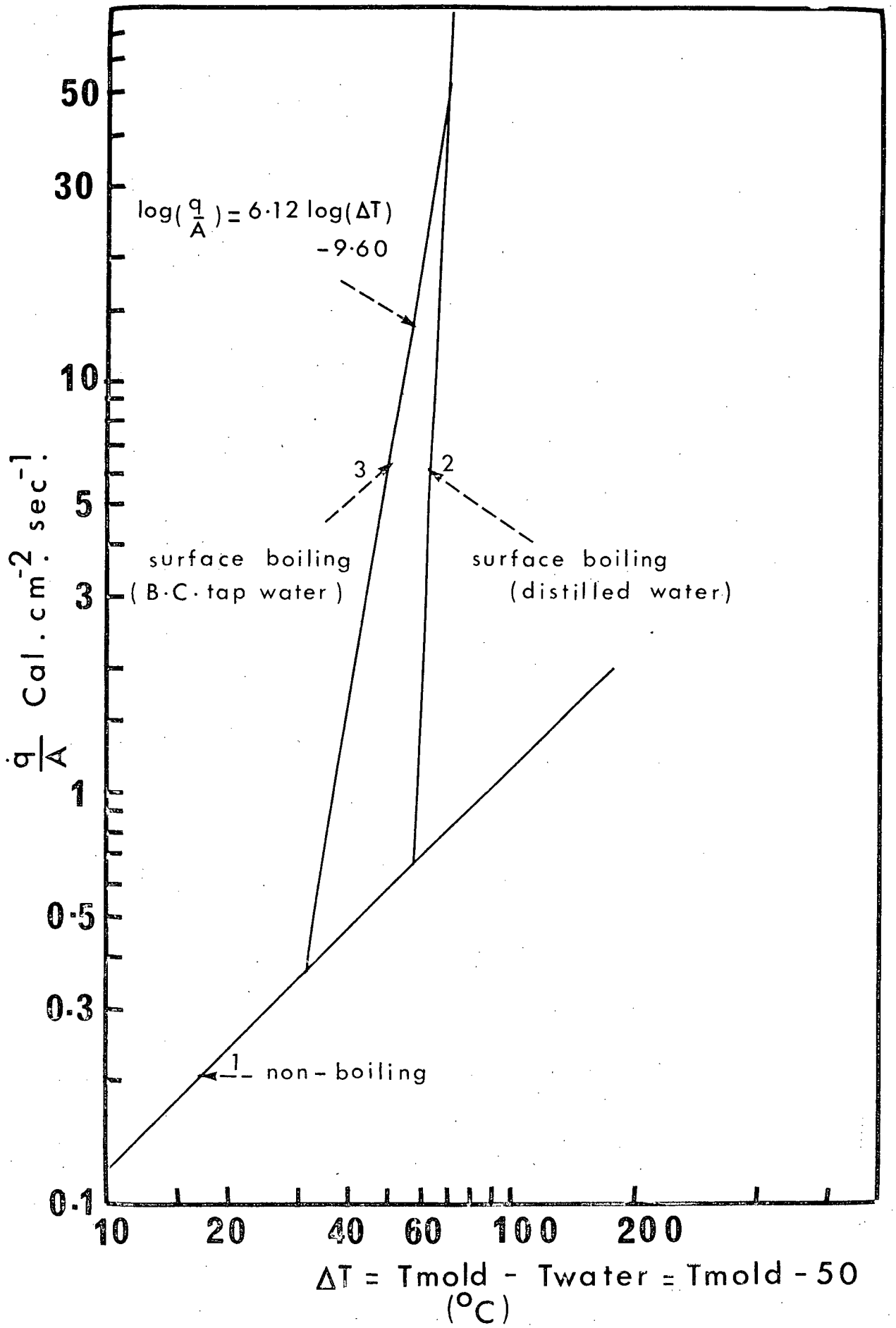

Figure 49. Plot of (q/A) vs. ΔT for (a) non-boiling and (b) surface boiling conditions.

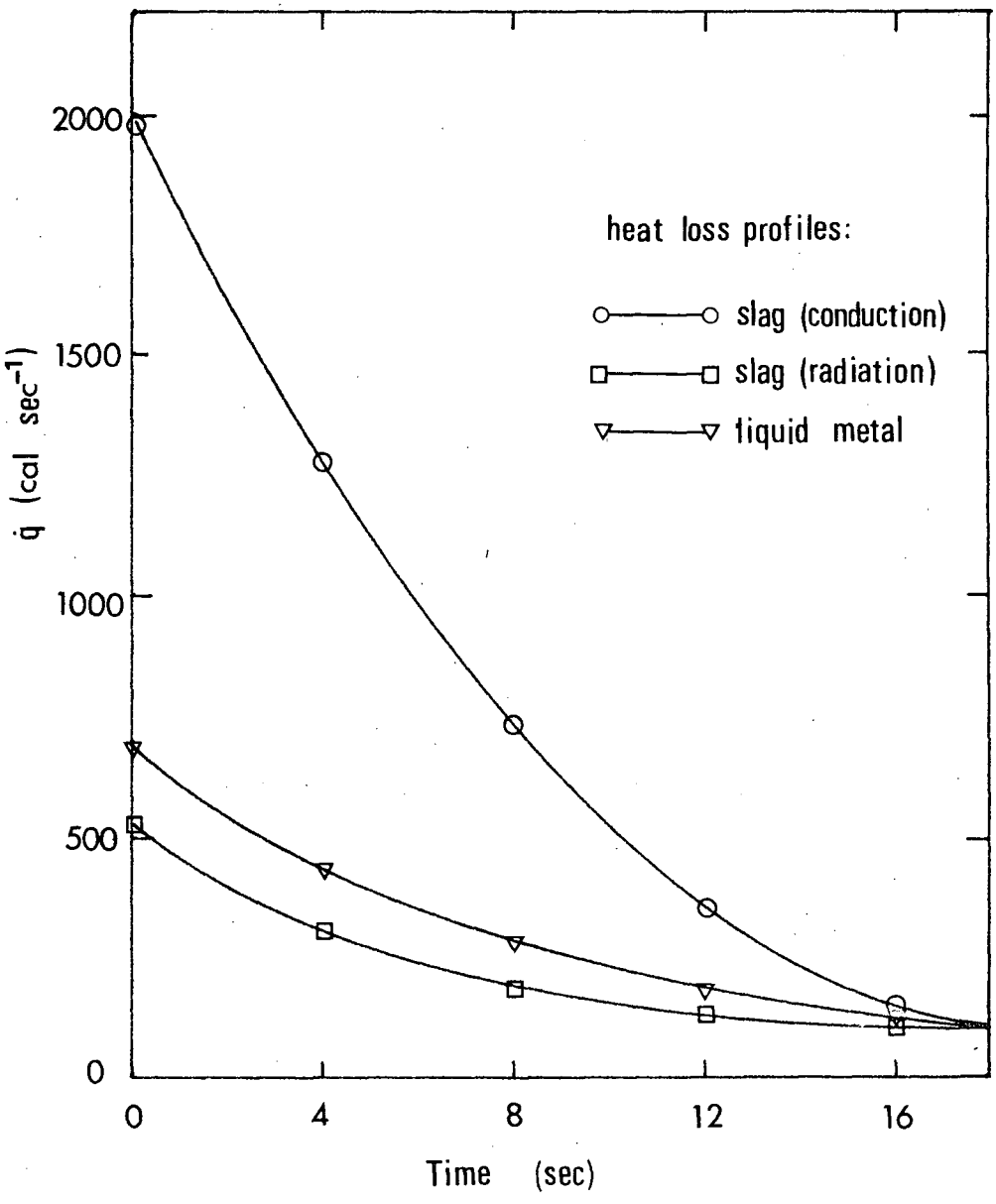

Figure 50. Plot of $\dot{q}$ vs time for (a) slag (conduction), (b) slag (radiation) and (c) liquid metal.

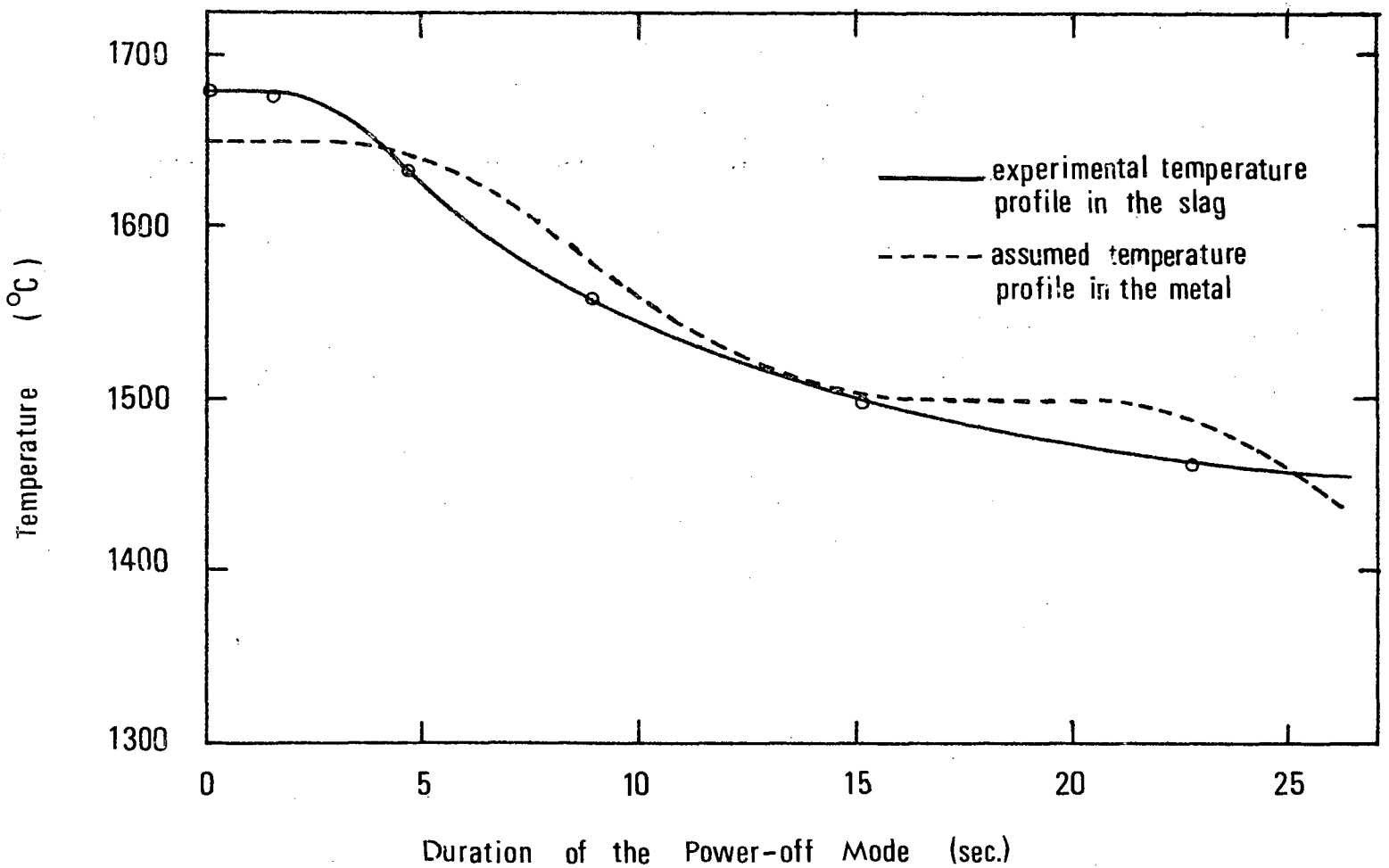

Figure 51. Plot of temperature vs time for (a) the slag and (b) the metal.

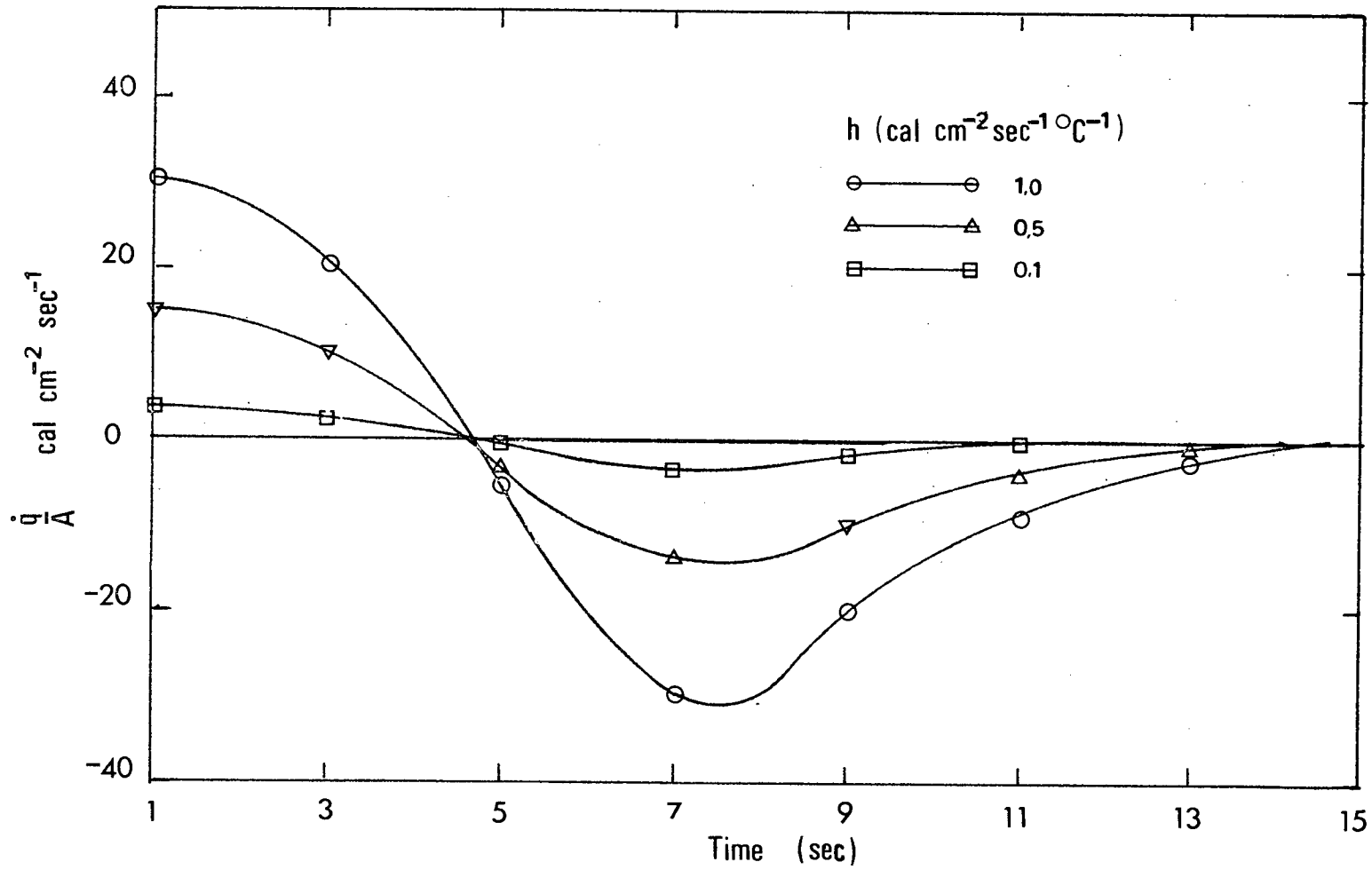

Figure 52. Plot of $\dot{q}/A$ vs time for different values of h_I.

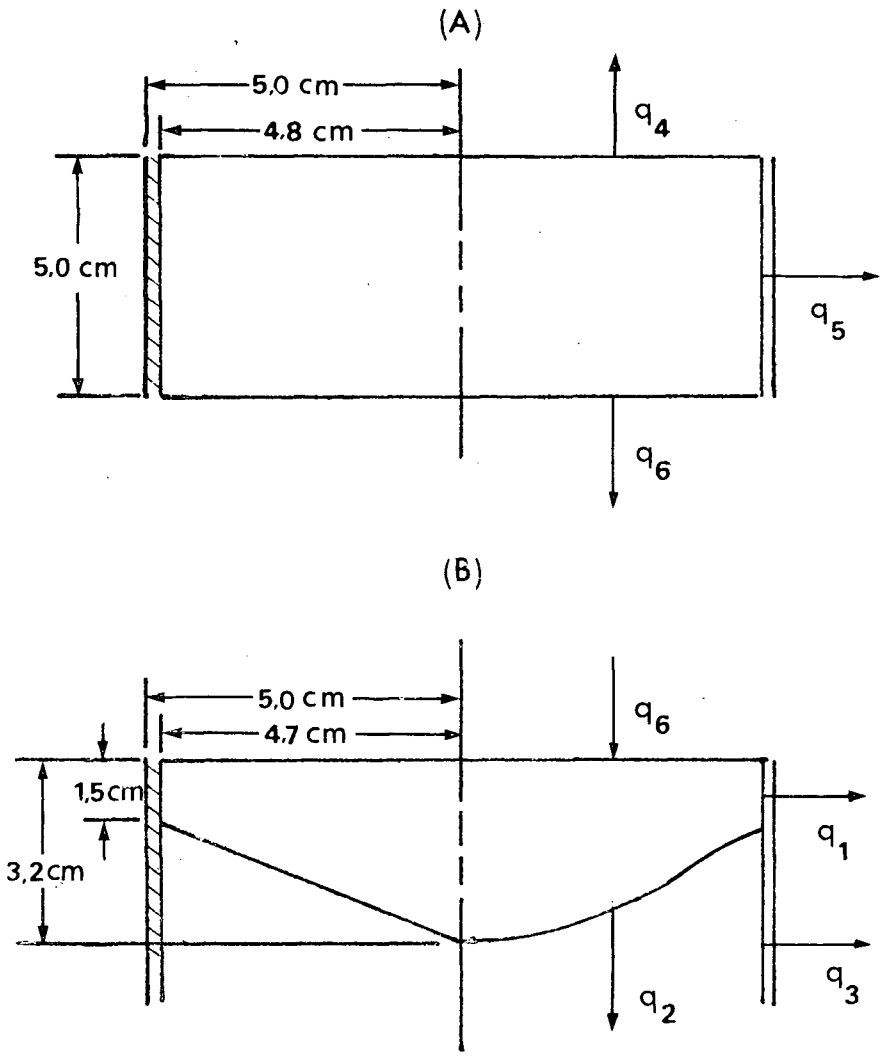

Figure 53. Assumed pool configurations in a 10 cm dia. ingot for (A) slag, (B) metal.

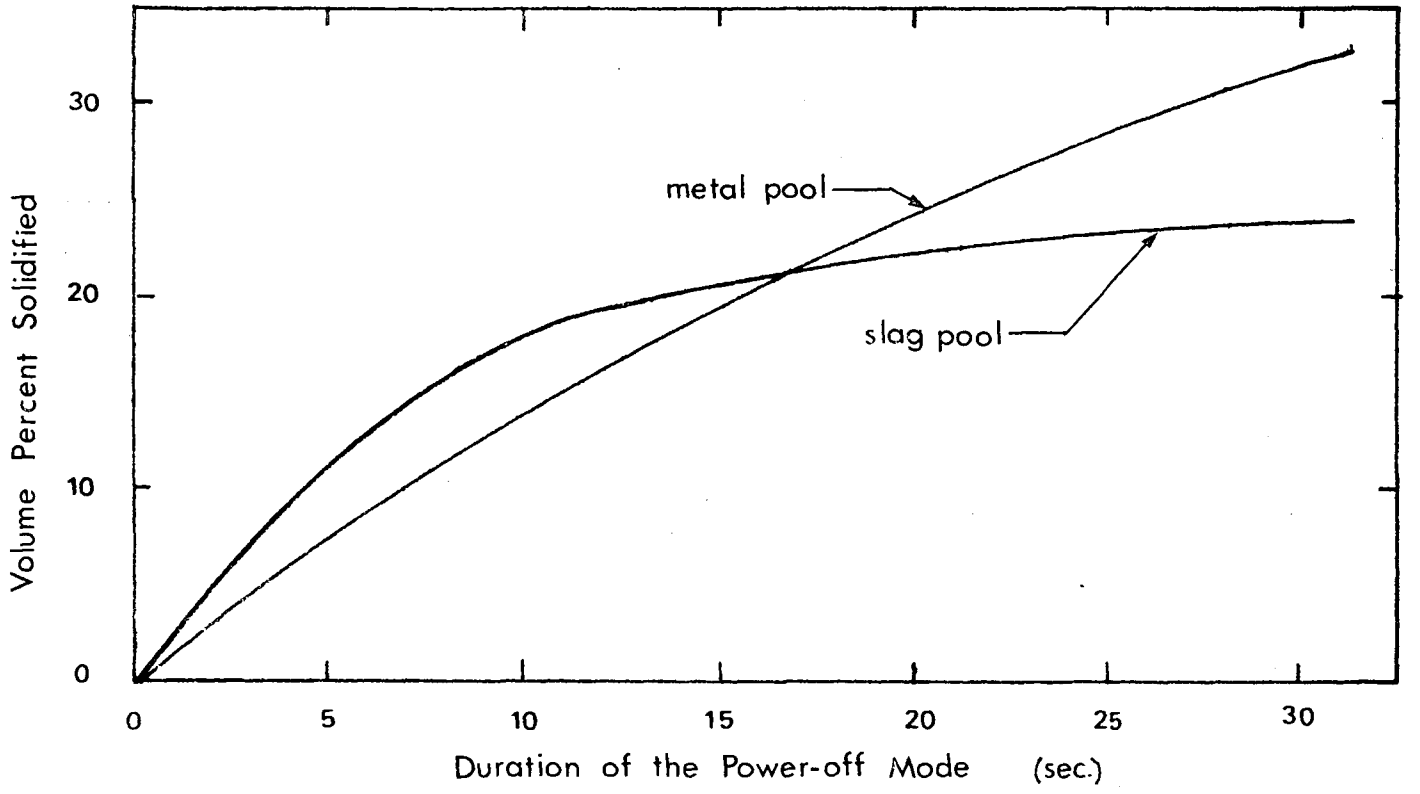

Figure 54. Plot of volume percent solidified vs duration of the "power-off" mode.

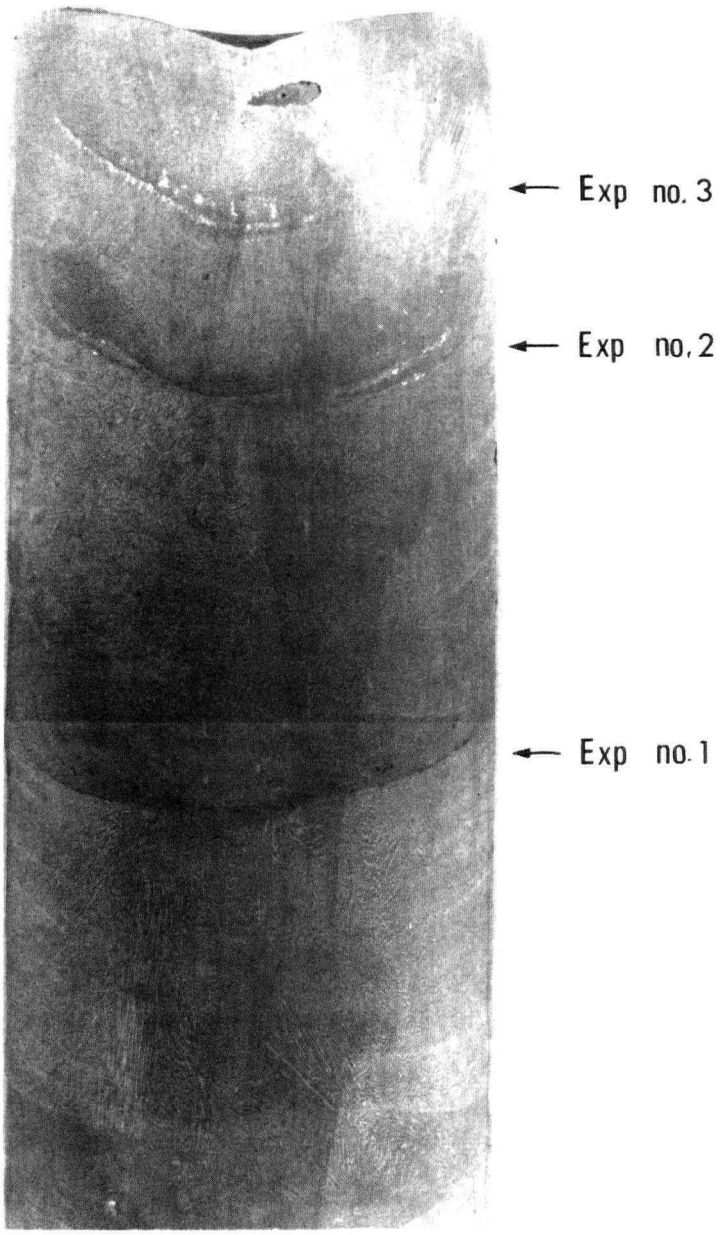

Figure 55. Macrograph of ingot no. 13 containing three w powder addition experiments.

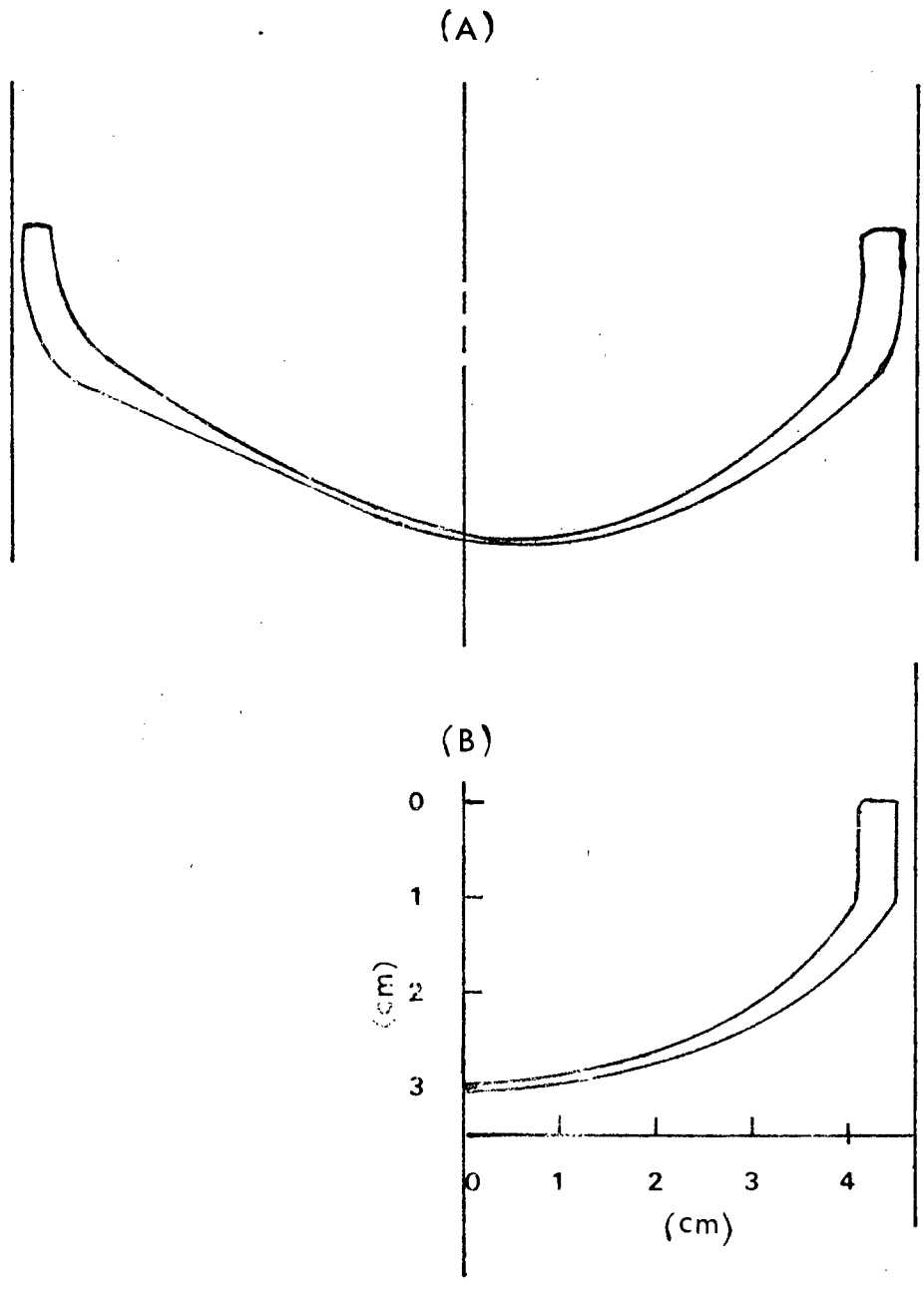

Figure 56. Actual and approximated pool profiles for a w-power addition experiment.

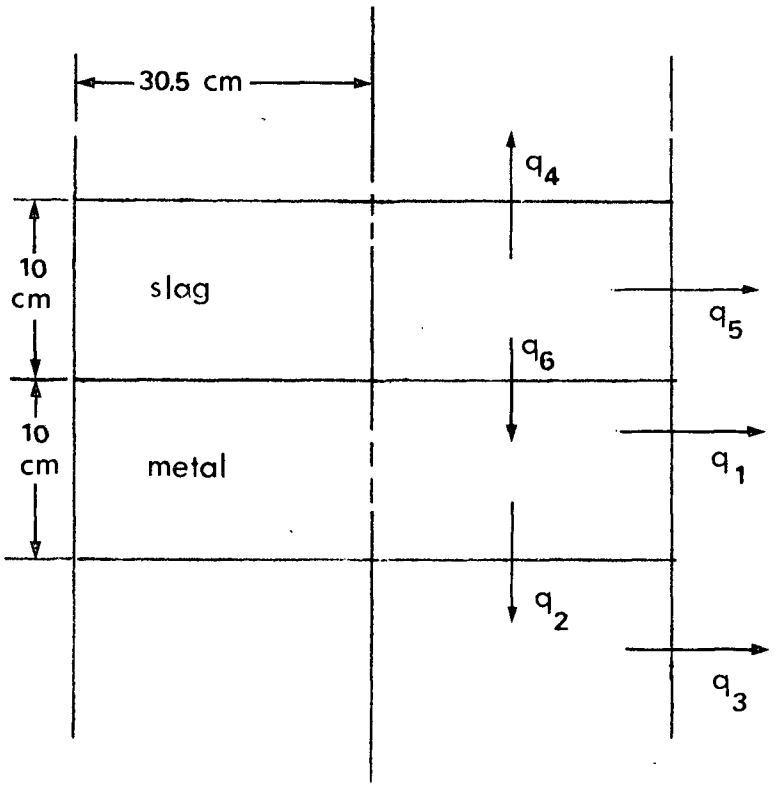

Figure 57. Schematic representation of a 61 cm dia. ESR ingot.

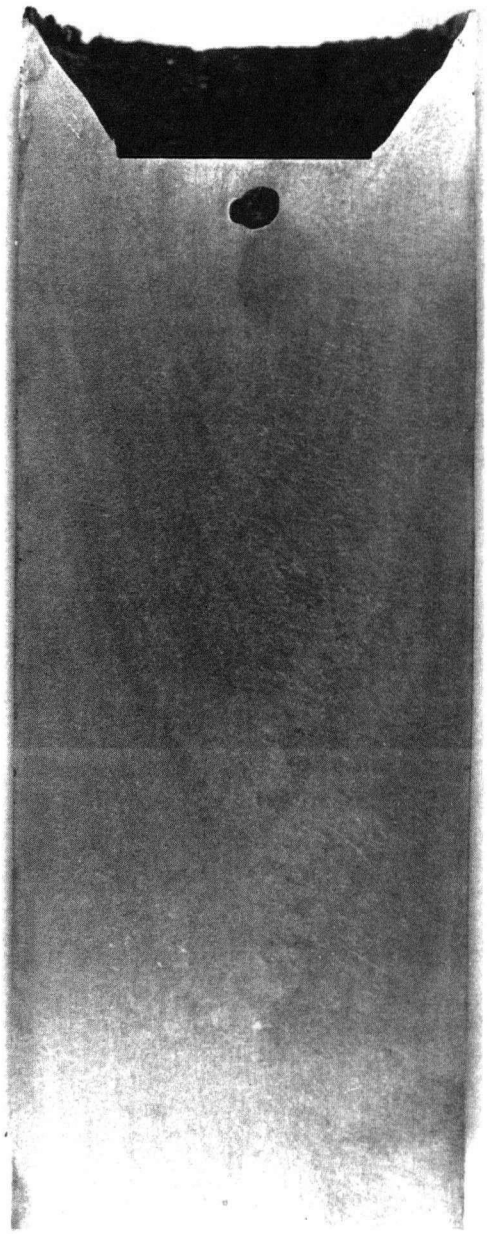

Figure 58. Macrograph of ingot no. V-3 containing several power interruptions.

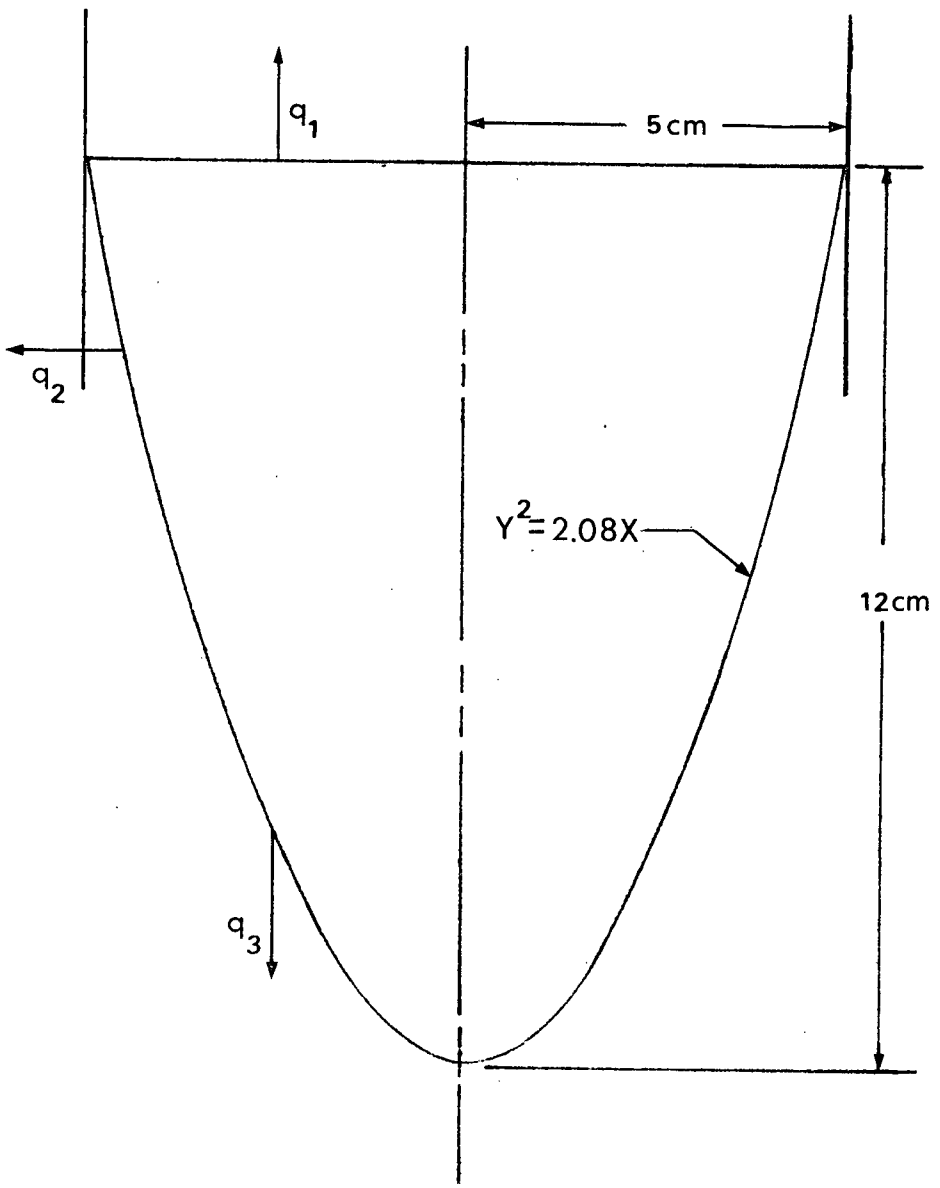

Figure 59. Approximation of the metal pool profile in ingot V-3.

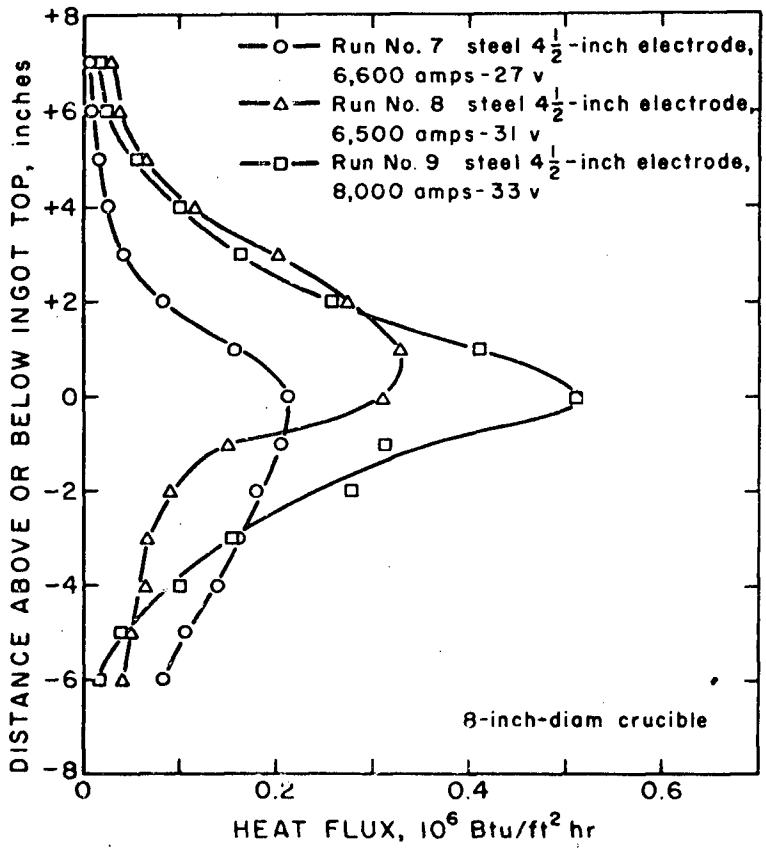

Figure 60. Effect of arc current and arc potential on the heat flux to the crucible wall during the VAR melting of steel electrodes.

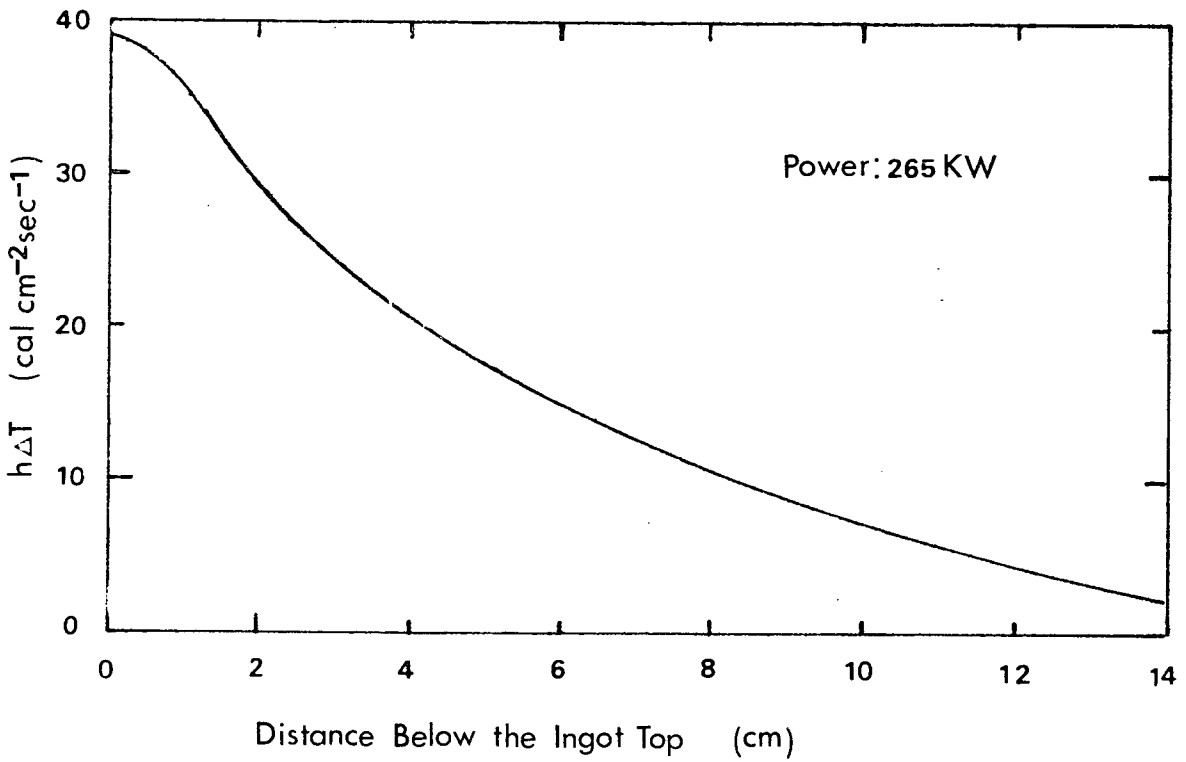

Figure 61. Heat flux profile for run no. 9, Figure 60.

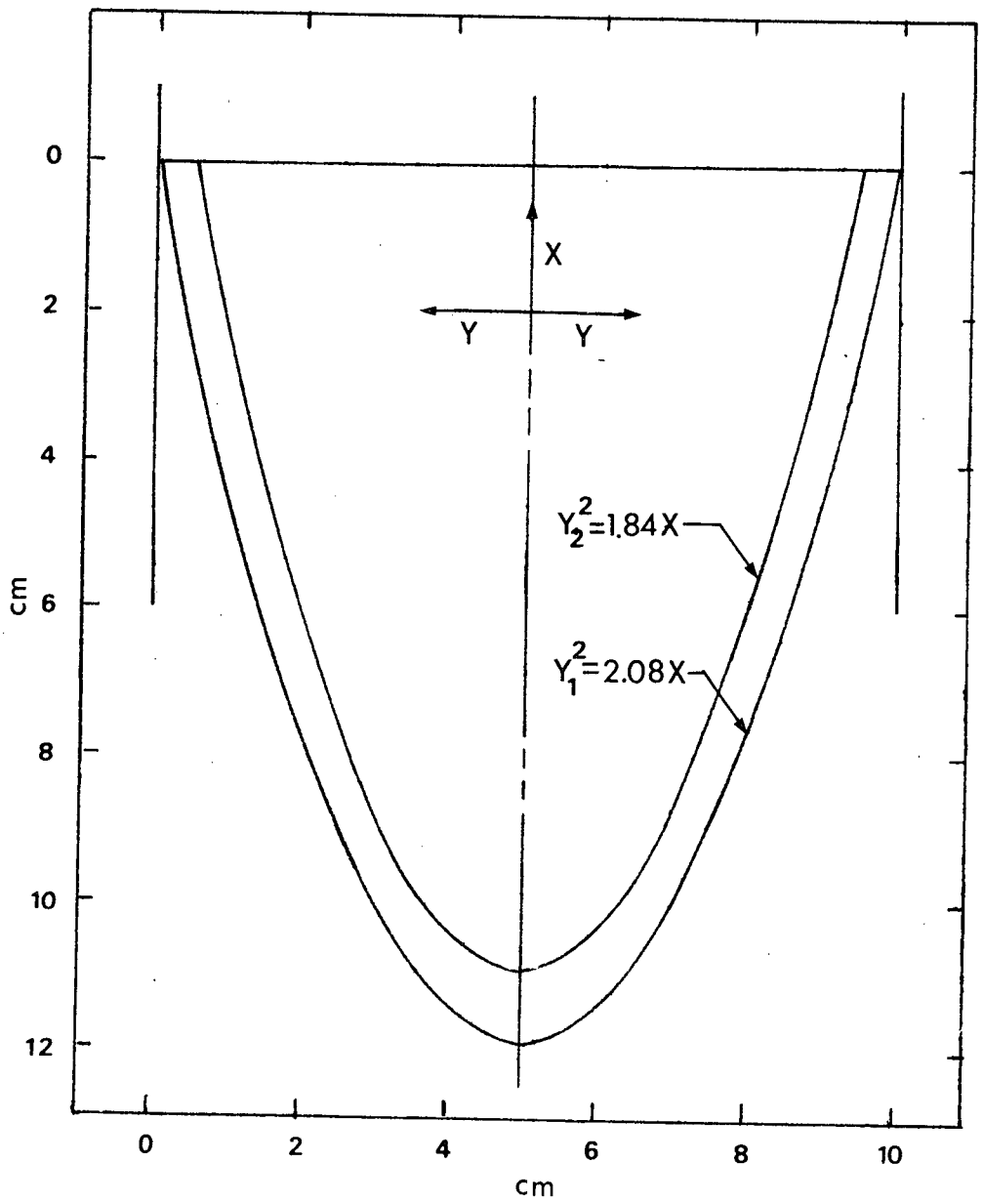

Figure 62. Approximation of the volume solified during a 12.5 second power interruption in a 10 cm dia. VAR ingot.

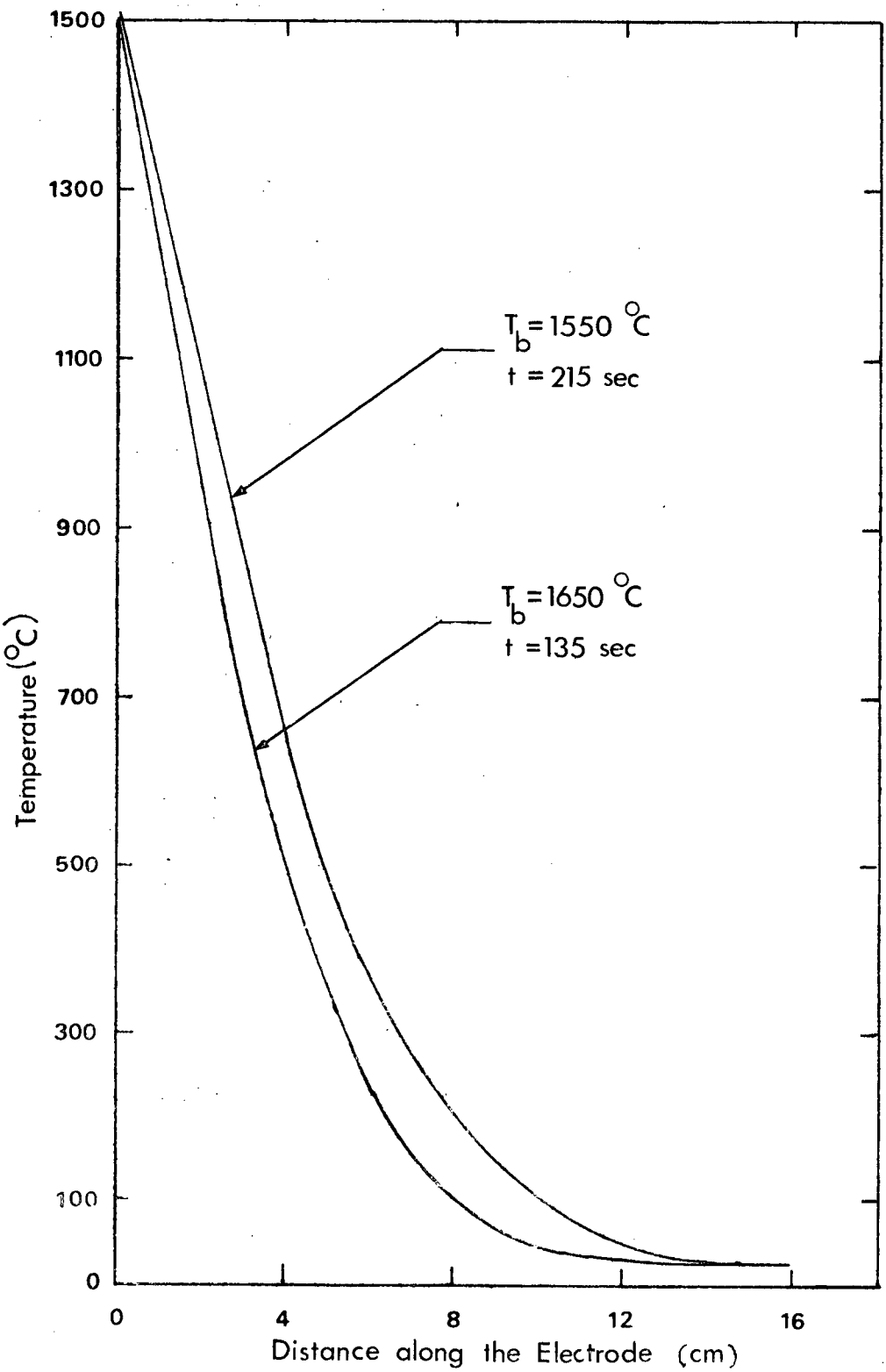

Figure 63. Plot of temperature vs distance along the electrode for (a) T_b = 1550°C, and (b) T_b = 1650°C.

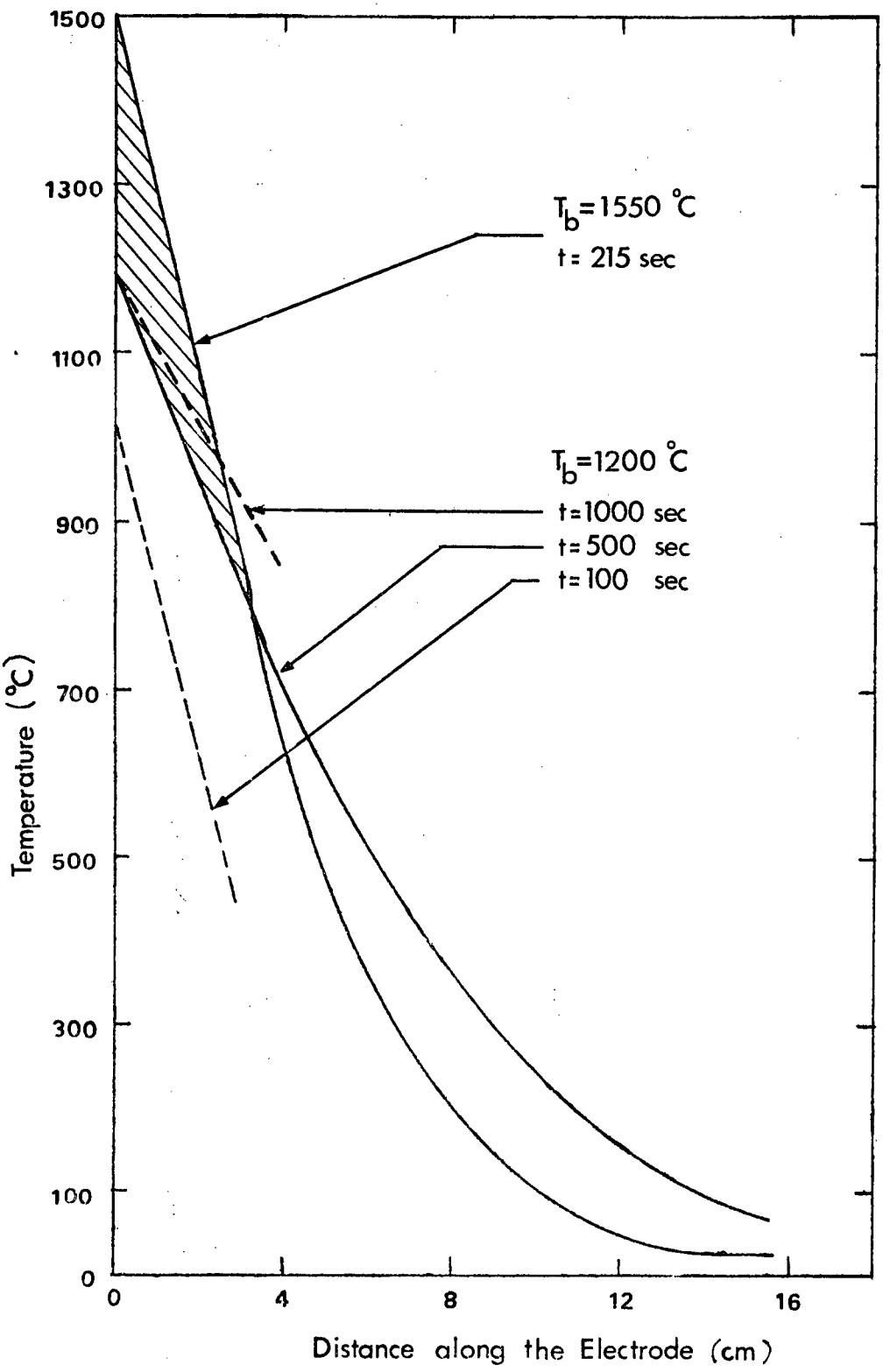

Figure 64. Plot of temperature vs distance along the electrode for (a) T_b = 1550°C, (b) T_b = 1200°C, t = 100, 500 and 1000 seconds.